Investigation of the electronic properties of two-dimensional metal halide perovskites via magneto-optical spectroscopy

Shuli Wang

Université Fédérale
Toulouse Midi-Pyrénées

THÈSE

En vue de l'obtention du
DOCTORAT DE L'UNIVERSITÉ DE TOULOUSE

Délivré par l'Institut National des Sciences Appliquées de Toulouse

Présentée et soutenue par

Shuli WANG

Le 15 mai 2023

Étude des propriétés électroniques des perovskites bidimensionnelles à halogénure métallique par spectroscopie magnéto-optique

Ecole doctorale : **SDM - SCIENCES DE LA MATIERE - Toulouse**

Spécialité : **Nanophysique**

Unité de recherche :
LNCMI - Laboratoire National des Champs Magnétiques Intenses

Thèse dirigée par
Duncan MAUDE et Paulina PLOCHOCKA

Jury

M. Grzegorz SEK, Rapporteur
Mme Maria CHAMARRO, Rapporteure
M. Vincent PAILLARD, Examinateur (Presedent)
M. Adam BABINSKI, Examinateur
M. Duncan MAUDE, Directeur de thèse
Mme Paulina PLOCHOCKA, Co-directrice de thèse

THÈSE

En vue de l'obtention du

DOCTORAT DE L'UNIVERSITÉ DE TOULOUSE

délivré par Institut national des sciences appliquées de Toulouse
Spécialité : Nano physique

Présentée et soutenue par
Shuli WANG

Investigation of the electronic properties of two-dimensional metal halide perovskites via magneto-optical spectroscopy

---

Ecole doctorale : Science de la Matière
Unité de recherche : Laboratoire National des Champs Magnétiques Intenses
Directeurs de Thèse : Paulina PLOCHOCKA et Duncan MAUDE

Investigation of the electronic properties of two-dimensional metal halide perovskites via magneto-optical spectroscopy

Abstract: In recent years, two-dimensional (2D) metal halide perovskite materials have attracted considerable attention due to their unique and excellent electronic and optical properties, which make them an extremely promising semiconductor for light-emitting and display applications. Furthermore, the nonmagnetic perovskite can be semi magnetic semiconductor by incorporating magnetic impurities into lattices of the host perovskite to introduce magnetic properties. The coexistence of both excellent optoelectronic and magnetic properties, makes semi magnetic 2D perovskite to be a considerably promising material for opto-spintronic semiconductor devices for information processing and communications.

In this thesis, we explore the electronic and optical properties of 2D perovskites via magneto-optical spectroscopy. We start from performing magneto-photoluminescence (PL) and magneto-transmission measurements on $CsPbBr_3$-based nanoplatelets with a different thickness of the lead-halide slab, ranging from 2 to 4 layers of lead-halide octahedral plane. By applying in-plane magnetic fields up to 65 T, the optically inactive dark excitonic state is brightened. This approach allows us to directly observe an improvement of the PL emission on the low-energy side of the PL spectrum, which indicates that the optically inactive dark excitonic state is the lowest-lying state in these nanoplatelets. Additionally, combining our magneto-PL and magneto-transmission results with theoretical predictions of the exciton fine structure splitting, we accurately determine the energy splitting between the dark and bright excitons. We demonstrate that indeed the dark-bright exciton splitting increases with decreasing layers of lead-halide octahedral plane. We also demonstrate that the efficient emission from these nanoplateltes is due to a phonon bottleneck, which significantly reduces the relaxation of the photo excited excitons to the optically inactive dark state.

Finally, we investigate the electronic properties of Mn-doped 2D $(PEA)_2PbI_4$ perovskite via magneto-transmission spectroscopy for various Mn molar fractions. We find that the exciton Landé g-factor can be controlled by the incorporated Mn concentration. With increasing Mn concentration x from 0 to 2%, the g-factor increases, which we attribute to the sp-d exchange interaction between band-edge excitons and spins hosted in Mn ions. If the Mn concentration is increased further, up to 5%, the exciton g-factor decreases. This anomalous counter-trend is attributed to the Mn-Mn interactions, which result in an effective anti-ferromagnetic coupling.
Keywords: Two-dimensional metal halide perovskites, nanoplatelets, Mn-doped perovskites, magneto-optical spectroscopy, dark-bright exciton splitting, exciton g-factor

Investigation des propriétés électroniques des pérovskites bidimensionnelles à halogénure métallique par spectroscopie magnéto-optique

Abstract: Les matériaux pérovskites bidimensionnels (2D) ont attiré une attention considérable en raison de leurs propriétés électroniques excellentes, qui en font un semi-conducteur extrêmement prometteur pour les applications d'émission de lumière. En outre, la pérovskite non magnétique peut devenir un semi-conducteur magnétique en incorporant des impuretés magnétiques dans les réseaux de la pérovskite hôte pour introduire des propriétés magnétiques. La coexistence d'excellentes propriétés optoélectroniques et magnétiques fait de la pérovskite 2D semi-magnétique un matériau très prometteur pour les dispositifs semi-conducteurs opto-spintronique pour le traitement de l'information et les communications.

Dans cette thèse, nous explorons les propriétés électroniques des pérovskites 2D via la spectroscopie magnéto-optique. Nous commençons par effectuer des mesures de magnéto-photoluminescence (PL) et de magnéto-transmission sur des nanoplaquettes à base de $CsPbBr_3$ avec une épaisseur différente de la dalle de plomb-halogénure, allant de 2 à 4 couches de plan octaédrique de plomb-halogénure. En appliquant des champs magnétiques dans le plan jusqu'à 65 T, l'état excitonique sombre optiquement inactif est éclairci. Cette approche nous permet d'observer directement une amélioration de l'émission PL du côté basse énergie du spectre PL, ce qui indique que l'état excitonique sombre optiquement inactif est l'état le plus bas dans ces nanoplaquettes. De plus, en combinant nos résultats de magnéto-PL et de magnéto-transmission avec les prédictions théoriques de la division de la structure fine de l'exciton, nous déterminons avec précision la fractionnement d'énergie entre les excitons sombres et lumineux. Nous démontrons qu'en effet, la division des excitons sombres et lumineux augmente avec la diminution des couches du plan octaédrique du plomb-halogénure. Nous démontrons également que l'émission efficace de ces nanoplatelles est due à un goulot d'étranglement phononique, qui réduit considérablement la relaxation des excitons photoexcités vers l'état sombre optiquement inactif.

Enfin, nous étudions la perovskite 2D $(PEA)_2PbI_4$ dopée au Mn par spectroscopie de magnéto-transmission pour différentes fractions molaires de Mn. Nous constatons que le g-facteur de Landé des excitons peut être contrôlé par la concentration de Mn incorporé. Avec l'augmentation de la concentration x de Mn de 0 à 2%, le g-facteur augmente, ce que nous attribuons à l'interaction d'échange sp-d entre les excitons de bord de bande et les spins hébergés dans les ions Mn. Si la concentration en Mn est encore augmentée, jusqu'à 5%, le g-facteur des excitons diminue. Cette contre-tendance anormale est attribuée aux interactions Mn-Mn, qui résultent en un couplage anti-ferromagnétique efficace.

Mots-clés: Pérovskites d'halogénure métallique bidimensionnelles, nanoplaquettes, pérovskites dopées au Mn, spectroscopie magnéto-optique, fractionnement d'exciton sombre-lumineux , g-facteur d'exciton.

Acknowledgements

First of all, I would like to deliver my sincerest gratitude to my supervisors, Dr. Paulina Plochocka and Dr. Duncan Maude. I appreciate them for accepting me as their PhD student even through I had a weak physical background before join their group. During my graduate study, they were very patient to guide my project and to correct my manuscripts. They gave me lots of inspiration and encouragement and provided me an excellent experimental platform which supported my PhD study. During my PhD study, I was deeply inspired by their dedication and enthusiasm in the research.

I would also like to thank the members of the jury for their valuable comments on this research.

I would also like to thank my colleagues in the Laboratoire National des Champs Magnétiques Intenses (LNCMI-Toulouse), who were always very kind and helpful. As older scientific brothers, Alessandro Surrente, Mateusz Dyksik, Michal Baranowski and Krzysztof Galkowski help me a lot with solving the problems in experiments, data analysis and paper writing. Thank to Nan Zhang, Miriam Karpinska, Paulina Peksa, Andrzej Nowok, Swaroop Palai and Nikodem Sokolowski for all the help during my stay in Toulouse. Thank to Tristan Thebault for helping me deal with French administrative work. A special thank to Nicolas Bruyant, Sylvie George, Marc Nardone, Abdelaziz Zitouni, Jérôme Béard, Jean-Pierre Nicolin and Tristan Moraine for their kind help with the probe, synchronization system, cryostat and generator during my measurements. Thank to Catherine Knodlseder, Cécile Laroche and Séverine Bories for helping me deal with my trips.

My acknowledgements are extended to my parents, who tried their best to create a comfortable circumstance for my study, and always encourage me to chase my dream. I would also like to thank my sister, who always supports me to go ahead.

A great thank to China Scholarship Council for awarding a 42 months scholarship, which allows me to pursue my study in France as a PhD student.

Finally, thank God.

Shuli Wang
Toulouse, February 2023

Contents

Chapter 1

Introduction

Contents

1.1 Perovskite structure

The origin of perovskite materials can be traced back to the discovery of the calcium titanate ($CaTiO_3$) mineral in the Ural Mountains of Russia in 1839. Perovskites are named after their discoverer, the Russian mineralogist Lev Perovski [Katz 2020]. Today, all materials with the same crystal structure as the $CaTiO_3$ mineral are referred to as perovskites. The generic chemical formula for perovskites– ionic crystals- is ABX_3, where A and B are two cations of considerably different sizes, and X is an anion.

In Fig.1.1 (a), we schematically show a perovskite unit cell in the cubic phase. The larger A cation is located at the corner position, the smaller B cation sits at the body center, and six X anions are located at the center of the cubic face. In a perovskite structure, the smaller B cation and six X anions form a BX_6 octahedral, where the B cation is located at the center of the octahedral, and X anions are located at the corners around the B cation. The BX_6 octahedral forms a three-dimensional network by connecting all the corners, while A cations fill the voids among the octahedral, as shown in Fig.1.1 (b).

In an ideal cubic structure, the B-X distance is equal to half of the cubic unit cell length $a/2$, and the A-X distance is $a/\sqrt{2}$. So that the relationship between ionic radii can be expressed as,

$$r_A + r_X = \sqrt{2}(r_B + r_X) \tag{1.1}$$

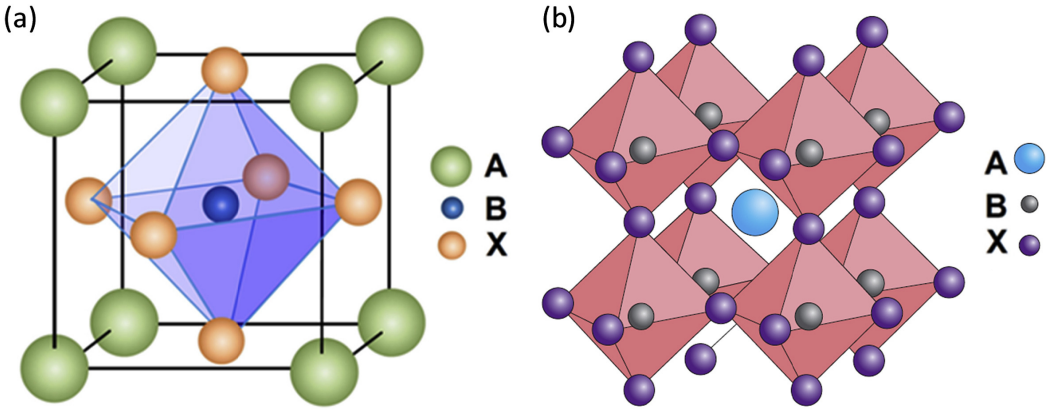

Figure 1.1: (a) Perovskite unit cell with the chemical formula ABX_3. Green, dark blue and orange spheres are A, B cations and the X anion. (b) The extended network structure of perovskites linked by the BX_6 octahedral. Light blue, grey and purple spheres represent A, B cations and X anion. Figure reprinted after reference [Moniruddin 2018].

It is worth to note that, even though equation 1.1 is not totally fulfilled, the cubic structure of perovskite may still be retained in ABX_3 compounds. To describe the difference from the ideal structure, Goldschmidt et al. introduced a concept of tolerance factor t [Goldschmidt 1926, Jia 2010, Pena 2001]:

$$t = \frac{r_A + r_X}{\sqrt{2}(r_B + r_X)} \tag{1.2}$$

which is applicable at room temperature to the empirical ionic radii. The ideal perovskite cubic structure appears in a few cases (such as $SrTiO_3$) with a t factor very close to 1 [Johnsson 2005]. However, the cubic structure may still be stable in the range of $0.89 < t \leq 1$ [Johnsson 2005, Buttner 1992]. In other cases, different ranges of the t factor define different distortions of the perovskite structure; (i) a tetragonal structure in the range $0.81 < t < 0.87$, (ii) orthorhombic structure with $t < 0.81$ [Li 2016] and (iii) hexagonal structure with $t > 1$ (*e.g.* $BaNiO_3$) [Johnsson 2005]. The classification of the perovskite structure described by tolerance factor t is only a rough approximation as this parameter mainly takes into account the ionic bonds.

Due to the great flexibility of chemical substitution of A, B and X atoms, perovskites form a relatively large family of materials. Owing to their different physical properties, perovskites have a wide range of commercial and industrial applications. Here, we introduce some representative perovskite materials and their potential applications. Perovskite oxides (ABO_3) as an important member of the perovskite family, exhibit excellent physical properties. $SrRuO_3$ exhibits both ferromagnetic and conducting properties, which is promising for spintronics applications [Boschker 2019]. $BaTiO_3$ perovskites are ferroelectric materials with wide applications in actuators, transducers, memories and capacitors [Megaw 1952, Zhang 2006]. $YBa_2Cu_3O_7$ perovskite possesses a rather unique superconductivity transition at

the temperature between 80 K and 93 K [Wu 1987]. $LaCoO_3$ exhibits thermally induced insulator-to-metallic transitions, which can be used for thermistor applications [Tokura 1998]. Metal halide perovskites, investigated in this thesis, with potential applications as light harvesters and emitters, will be introduced in detail in the following sections.

1.2 Metal halide perovskites

In the case of metal halide perovskites, B is usually a heavy divalent metal, typically either lead (Pb^{2+}) or tin (Sn^{2+}), X are halide ions, most commonly chloride (Cl^-), bromide (Br^-) or iodide (I^-), or an alloyed combination of these. The large cations can be either organic species such as methylammonium (MA: $CH_3NH_3^+$) or formamidinium (FA: $CH(NH_2)_2^+$), or fully inorganic species, such as cesium (Cs^+).

The first halide perovskite structures to be synthesized were the cesium lead halides ($CsPbX_3$), obtained by Moller in 1958 [Møller 1958]. Moller demonstrated the coloured $CsPbX_3$ crystals are photo-conductive, with different halide components X leading to a different spectral response. In 1978, the first organic metal halide perovskite-methylammonium based perovskite ($CH_3NH_3PbX_3$) was investigated by Weber [Weber 1978]. Due to the excellent optical and electronic properties, organic-inorganic metal halide perovskites were studied for field effect transistor (FET) and thin-film light-emitting diodes (LEDs) applications in the following years.

The first significant breakthrough in methylammonium based perovskites occurred with their use as light-absorbing materials in photovoltaic cells by Miyasaka et al., with an initial energy conversion efficiency of 3.8% [Kojima 2009]. Since then, rapid progress in perovskites based photovoltaic devices has been attained over only a few years, with the energy conversion efficiency increasing from 3.8% to 25.6% (single junction) [Jeong 2021], which is comparable to the mature technologies of solar cells based on silicon or copper indium gallium diselenide (CIGS) [Berry 2017].

1.2.1 Unique combination of the properties of metal halide perovskites

Metal halide perovskites are promising materials for all opto-electronic applications due to their unique combination of properties. Despite numerous defects due to their spin-coated fabrication, surprisingly, perovskites have long carrier life times of the order of hundreds nanoseconds [Stranks 2014], with correspondingly large carrier diffusion length. The value can be more than 1 μm, which is an order of magnitude more than the thickness of the active layer of perovskite solar cells, which is typically of 200-300 nm [Dong 2015]. Additionally, metal halide perovskites are also exceptional due to their high absorption coefficient. In Fig.1.2, it is seen that the optical absorption coefficient of $MAPbI_3$ is up to an order of magnitude greater than that of the traditional GaAs direct band gap semiconductor, over the visible light range. As this range accounts for the major usable portion of the full solar spectrum, high visible light absorption is essential to achieve high efficiency solar

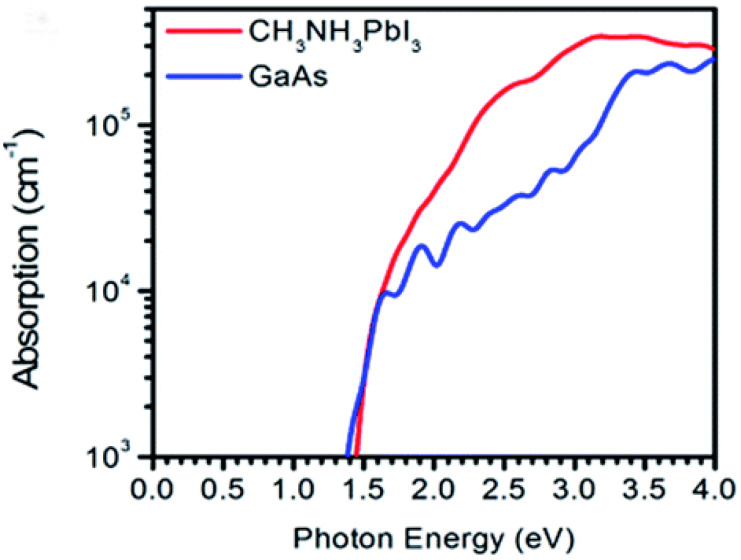

Figure 1.2: Absorption coefficients of $MAPbI_3$ and GaAs. Figure reprinted after reference [Elumalai 2016].

cells [Yin 2014, Elumalai 2016]. Furthermore, for $MAPbI_3$ perovskites, the fabrication process is much easier, and the cost is also much lower than for traditional GaAs.

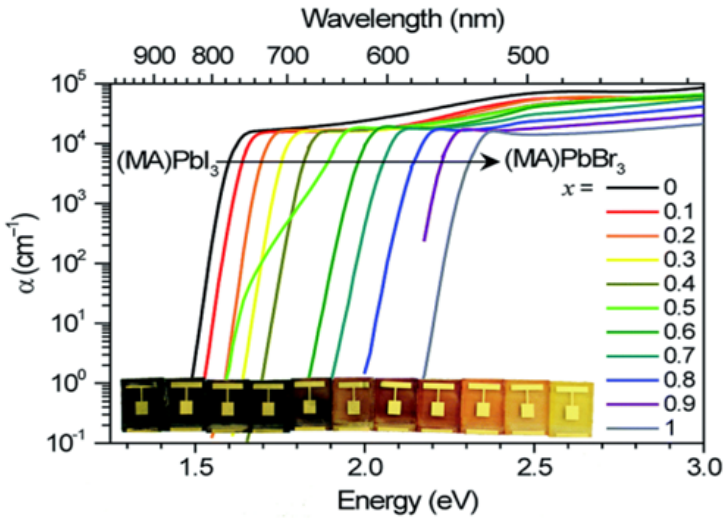

Figure 1.3: Absorption coefficient of $MAPb(Br_xI_{1-x})_3$ series. Inset: photograph of $MAPb(Br_xI_{1-x})_3$ photovoltaic devices from x = 0 to 1 (left to right). Figure reprinted after reference [Hoke 2015].

The band gap of halide perovskites can be easily modified by chemical substitution. Since the valence and conduction band are mainly dominated by the

hybridization of the p and s orbitals of the B cation and X anions, the inorganic octahedral slabs play a primordial role in tuning the band gap. For example, Hoke et al. studied the absorption of methylammonium based photovoltaic devices with different halide components [Hoke 2015], as shown in Fig.1.3. From left to right, the onset of the band-edge absorption changes from 1.6 eV (pure $MAPbI_3$ band gap) to 2.2 eV (pure $MAPbBr_3$ band gap), as the incorporated Bromide ions concentration x varies from 0 to 1. Moreover, the band gap of methylammonium based perovskite materials can further be tuned to the UV spectral region of 3.1 eV (pure $MAPbCl_3$ band gap) by introducing lighter chlorine ions [Leguy 2016].

1.2.2 Structural phase transition of metal halide perovskites

Metal halide perovskite materials show distinct temperature dependence of the lattice structure. At high temperatures (close to room temperature), perovskites have cubic crystal structure, as shown in Fig.1.4 (a) and (e) for, as an example, $MAPbI_3$. In this phase, the MA cations are fully disordered and can freely rotate between the PbI_6 octahedral. With decreasing temperature, the cubic structure can be transformed to a tetragonal phase, due to the octahedral tilting and distorting. In this case, MA cations are partially ordered and partially free to rotate [Whitfield 2016], as shown in Fig.1.4 (b) and (f). As the temperature is further reduced, the tetragonal crystal structure can be transformed to an orthorhombic structure, as shown in Fig.1.4 (c) and (g).

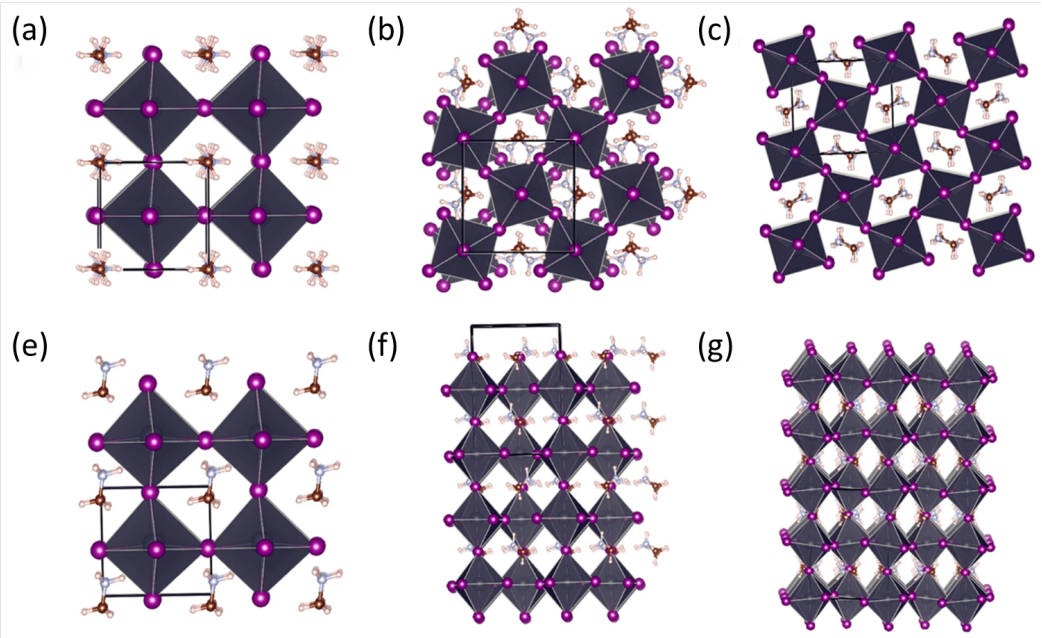

Figure 1.4: The crystal structure of (a,e) cubic, (b,f) tetragonal and (c,g) orthorhombic phase of $MAPbI_3$. Panels (a-c) are oriented though <001>, and panels (e-g) are oriented though <100>. Figure reprinted after reference [Tao 2017].

In this structure, the PbI_6 octahedral are strongly deformed, which restricts the rotational degrees of freedom of MA, resulting in the fully ordered MA cations [Whitfield 2016]. The critical temperature for each phase transition is different for different components of metal halide perovskites. According to results of Oku et al. [Oku 2015], the temperature regions corresponding to the relevant phase transitions of the $MAPbX_3$ (X = I, Br, Cl) perovskites are summarized in table 1.1.

Table 1.1: Temperature dependence of the crystal structure of $MAPbX_3$ (X = I, Br, Cl) perovskites. Data taken after reference [Oku 2015]

Material	Cubic	Tetragonal	Orthorhombic
$MAPbI_3$	$T > 330$ K	161 K $< T < 330$ K	$T < 161$ K
$MAPbBr_3$	$T > 236$ K	150 K $< T < 237$ K	$T < 150$ K
$MAPbCl_3$	$T > 177$ K	172 K $< T < 177$ K	$T < 172$ K

When the structural phase transition occurs, the electronic properties of metal halide perovskites are significantly modified. Since the band structure originates from BX_6 octahedral, the induced octahedral tilting with decreasing temperature, leads to an increase of the band gap. For example, in the case of $MAPbI_3$, the band gap in the orthorhombic structure can be around 100 meV larger than the band gap in the tetragonal structure at room temperature [Davies 2018]. Additionally, when the orthorhombic structure transforms to the tetragonal structure, the dielectric screening increases due to the increased rotational degrees of freedom of the organic cations. As a result, the exciton binding energy is smaller in the tetragonal phase than in the orthorhombic phase [Galkowski 2016]. The values of the exciton binding energy of $MAPbI_3$ perovskites obtained from magneto-optical measurements in the orthorhombic structure and in the tetragonal structure are 16 meV and 12 meV, respectively [Miyata 2015, Galkowski 2016].

1.2.3 Band structure of metal halide perovskites

By far, most of the calculation of the band structure of metal halide perovsites is based on the use of density functional theory (DFT) [Even 2015, Tao 2017, Ghaithan 2021]. In order to clarify the electronic band structure of metal halide perovskites, here, we summarize the DFT calculations, performed by Even *et al.* on the representative $MAPbI_3$ perovskite [Even 2015, Even 2014b]. The cubic crystal structure of $MAPbI_3$ exists a $Pm3m$ space group symmetry, and the tetragonal phase of $MAPbI_3$ has a $I4/mcm$ space group symmetry, which is a subgroup of $Pm3m$ [Even 2014a].

A real-space 3D view of the $pm3m$ cubic crystal structure of metal halide perovskite is presented in Fig.1.5 (a), the corresponding reciprocal space 3D view which shows the first Brillouin zone of the $pm3m$ space group is presented in Fig.1.5 (b). Γ-point is located at the center of the Brillouin, X-point is at the face center of the Brillouin zone boundary and M-point and R-point are located at the center of cube

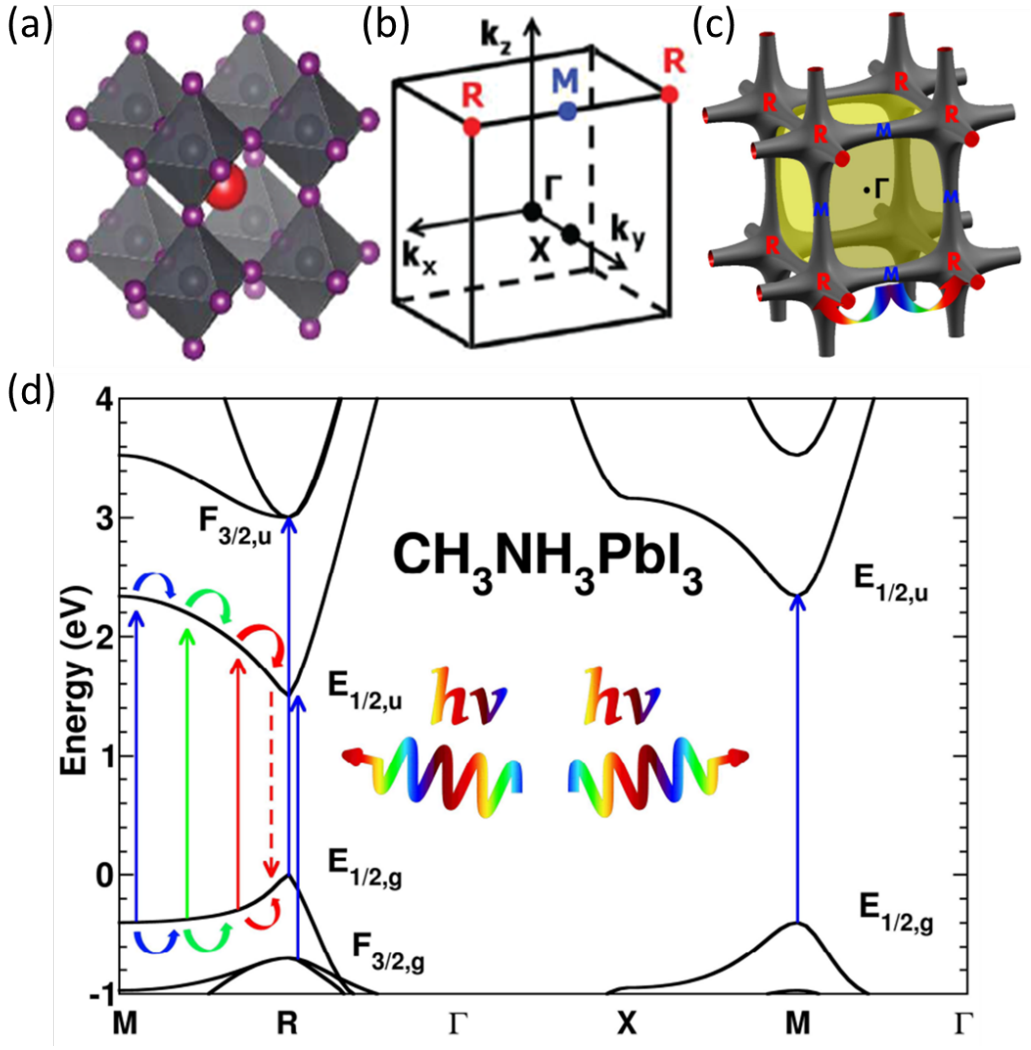

Figure 1.5: (a) Real-space 3D view of the $Pm3m$ cubic crystal structure of the metal halide perovskites. (b) Reciprocal-space 3D view showing the first Brillouin zone of the $Pm3m$ space group. (c) Fermi surface (E = -0.5 eV) in the first Brillouin zone. Points R and M are connected along the edges, highlighting the saddle nature of the point M. (d) Electronic band structure for the cubic $Pm3m$ of $CH_3NH_3PbI_3$ (with spin-orbital coupling). Vertical arrows show various possible optical transitions close to the band gap energy. Optical transitions along the line between the M and R points generate carriers that easily relax toward the R point. Figure reprinted after reference [Even 2015, Even 2014b].

edges and vertices of the cube, respectively. A schematics of the Fermi surface in the Brillouin zone is shown in Fig.1.5 (c). This iso-energy surface with energy -0.5 eV below the valence band maximum, connects the valleys of the Brillouin zone, centered at the R points with the saddle points M. This suggests that, in recipro-

cal space, the photo-generated hole carriers at the edges of Brillouin zone can flow toward R-point [Even 2014b].

In Fig.1.5 (d), the band structure of the cubic structure of $MAPbI_3$ perovskite calculated at different points of the Brillouin zone is presented. The DFT results indicated the optical transitions are related to two high symmetric points of R and M, where the direct band gap at the R-point is the primary band gap and at the M-point is the secondary band gap. Near the R-point, possible dipole allowed optical transitions are marked by vertical solid arrows. At M-point, the optical transitions between $E_{1/2,g}$ valence band and $E_{1/2,u}$ conduction band are also optical allowed, as the blue arrow shows. Since the M-point has a saddle-like nature, the carriers generated by photons at the M-point can relax to the R-point along M $\rightarrow$ R path, as schematically shown by the colored bent arrows in Fig.1.5 (d). The optical transition of the ground state is at the R-point between $E_{1/2,g}$ valence band and $E_{1/2,u}$ conduction band. Furthermore, additional transitions (secondary) at the R-point such as $E_{1/2,g} \rightarrow F_{3/2,u}$ and $F_{3/2,g} \rightarrow E_{1/2,u}$ are also optically allowed. The trapped photo-generated carriers in $F_{3/2,u}$ and $F_{3/2,g}$ states at R-point will relax through the paths $F_{3/2,u} \rightarrow E_{1/2,u}$ and $F_{3/2,g} \rightarrow E_{1/2,g}$ due to the optical phonon assisted relaxation process [Even 2014b].

The character of the valence band is dominated by iodine p-like orbitals with some component of lead s-like orbitals, while the conduction band is mainly formed by lead p-like orbitals with some hybridization with the iodine s-like orbital [Kirstein 2022, Umebayashi 2003]. The strong spin orbit coupling (SOC) splits the electronic states. The band splitting is more noticeable in the conduction band due to the domination of the heavy lead atom, which can be at ≈ 1.3 eV at the R-point (energy space between $E_{1/2,u}$ and $F_{3/2,u}$ states in Fig.1.5 (d)). However, the splitting of the valence band at the R-point is only ≈ 0.6 eV (energy space between $E_{1/2,g}$ and $F_{3/2,g}$ states in Fig.1.5 (d)) compared to the large splitting in conduction band. Consequently, the SOC effect significantly reduces the band gap by splitting the lowest degenerate states in the conduction band.

In section 1.2.2, we mentioned that with increasing temperature, the crystal structure of $MAPbI_3$ transforms from the orthorhombic phase to the tetragonal phase, and finally to a cubic phase around room temperature. Here, temporarily neglecting the SOC effect, we show the electronic band structures of $MAPbI_3$ in these three different phases in Fig.1.6 (a-c). The band gap in the orthorhombic structure or tetragonal structure is distinctly large than the band gap in the cubic structure due to the PbI_6 octahedral tilting and symmetry reduction. Additionally, the ground state transitions in the orthorhombic and tetragonal structures are of a direct type at Γ-point rather than R-point and M-point. The electronic states from R and M points in the Brillouin zone of cubic structure are folded back to Γ point in the Brillouin zone of orthorhombic and tetragonal structures.

For a $MAPbI_3$ material with the cubic structure and without the SOC effect, the p-like conduction band and s-like valence band of a PbI_6 octahedral have Γ_4^- and Γ_1^+ symmetries in the point group of the PbI_6 octahedral (O_h), respectively, as schematically shown in Fig.1.7 (a). Now we take the SOC effect into consideration

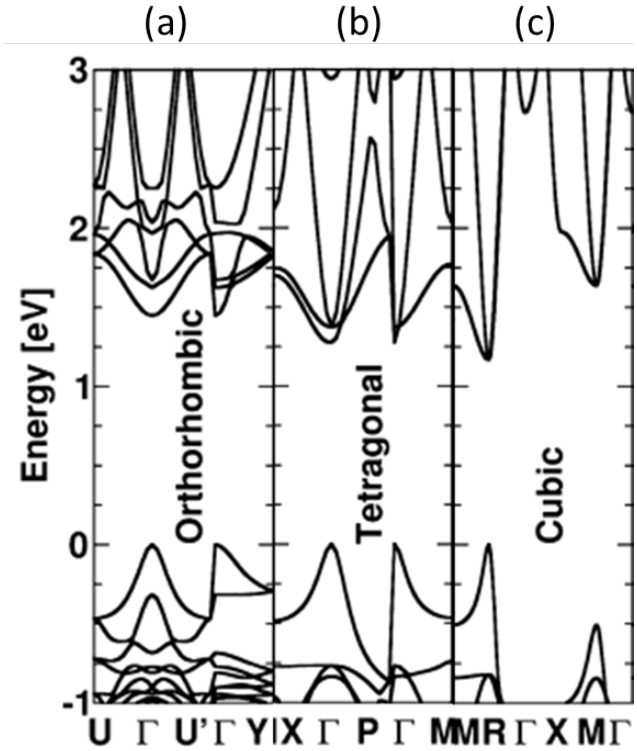

Figure 1.6: Electronic band structures of (a) orthorhombic, (b) tetragonal and (c) cubic phase of $MAPbI_3$. Figure reprinted after reference [Even 2015].

to discuss the electronic band structures under different symmetric conditions. The strong SOC effect significantly splits the electronic states; the sixfold conduction band transforms as a fourfold Γ_8^- state ($J = 3/2$, J represents the total angular momentum) and a twofold Γ_6^- state ($J = 1/2$), while the valence band transforms as a Γ_6^+ state ($J = 1/2$), as shown in Fig.1.7 (b). After introducing the tetragonal crystal field, the valence band keeps the Γ_6^+ symmetry, while the conduction band splits into three bands, labeled as A, B and C, respectively, as shown in Fig.1.7 (c), where both A and C have Γ_6^- symmetry ($J_z = \pm 1/2$, J_z represents the total angular momentum J along the z projection), and B has Γ_7^- symmetry ($J_z = \pm 3/2$) [Tanaka 2005, Tanaka 2003]. The symmetry reduction further lifts the band splitting between A, B and C. In Fig.1.7 (d), we show the DFT-calculated band structure of $MAPbI_3$ in the orthorhombic crystal field [Even 2013]. The ground state at Γ-point of Brillouin zone mainly involves eight active Bloch levels; two levels for the valence band maximum and six levels for the conduction band minimum.

1.2.4 Two-dimensional metal halide perovskites: more stable materials

Halide perovskites based photovoltaic devices mainly comprise thin films of bulk perovskite materials, and the perovskite films are deposited by different methods

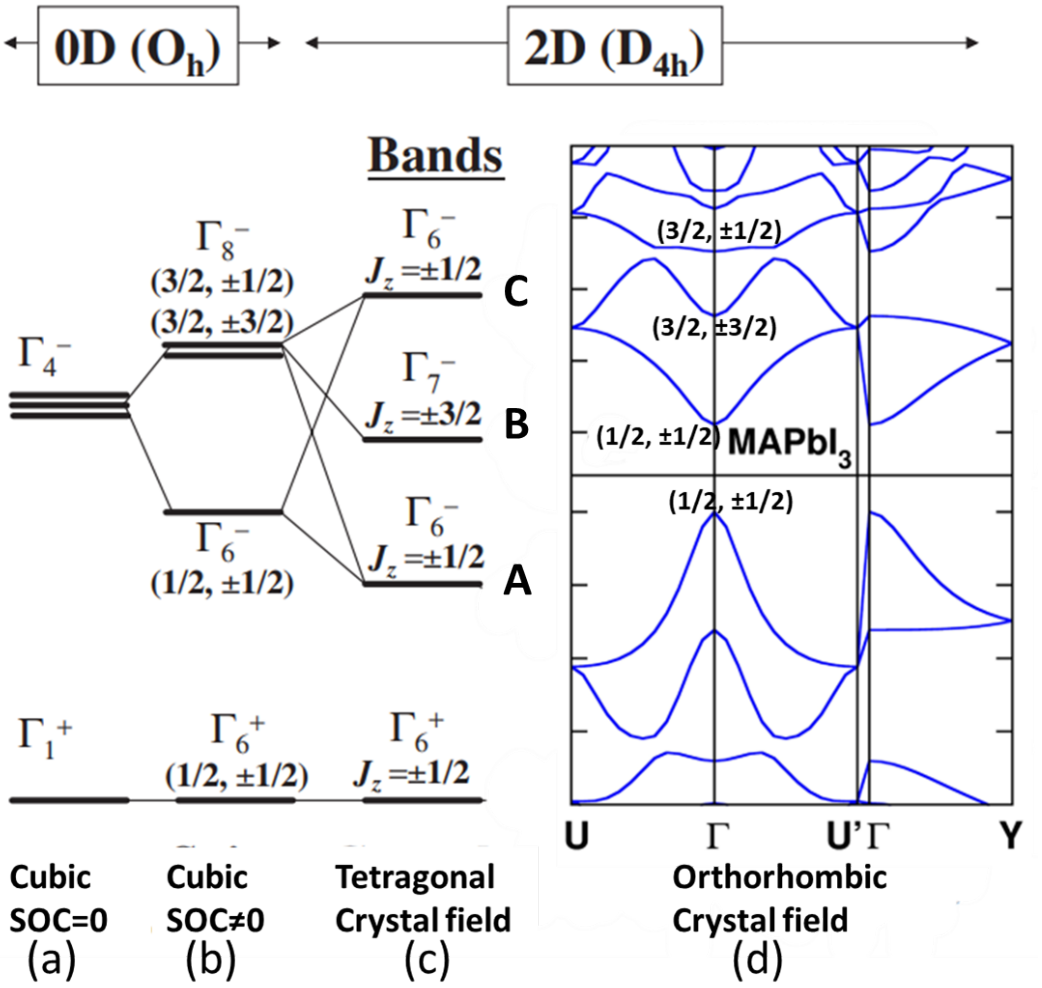

Figure 1.7: Schematic energy diagram of cubic crystal structure of $MAPbI_3$ at R point of Brillouin (a) without SOC effective and (b) with SOC effective. (c) Schematic energy diagram of tetragonal crystal structure of $MAPbI_3$ at Γ point of Brillouin zone. (d) Electronic band structure of $MAPbI_3$ in the orthorhombic phase with SOC effect. The origin of the energy scale is taken at the top of the valence band. Figure reprinted after reference [Tanaka 2005, Even 2013].

such as spin coating of perovskite solution [Tai 2019] and chemical vapor deposition (CVD) [Qiu 2021], *etc.* Despite the impressive photovoltaic performances of these devices, poor stability in ambient air limits their further development. First of all, the fabrication process and characterization of the devices have to be operated under the closed and controlled atmosphere in order to avoid the degradation. Additionally, the unavoidable formation of the defect states and grain boundaries in these photovoltaic devices during fabrication inevitably slow down the device performance [Varma 2018, Azpiroz 2015, Kim 2014]. Therefore, it is crucial to improve the purity of the materials and the stability of the thin films.

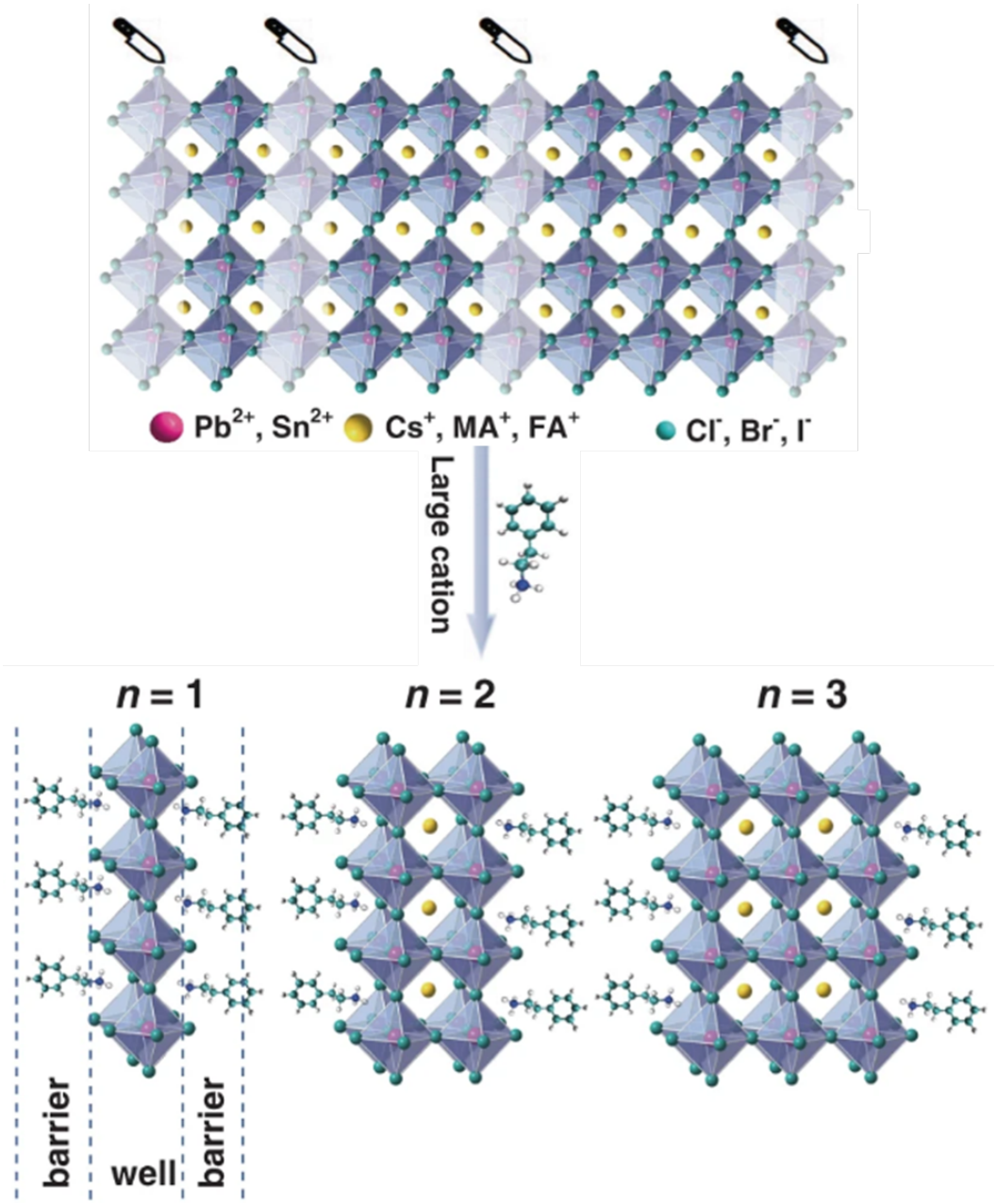

Figure 1.8: Schematic crystal structures of bulk (top) and 2D perovskite with different thickness of octahedral layers (bottom). 2D perovskites are obtained by tailoring the bulk perovskite along $< 100 >$ crystallographic direction. Figure reprinted after reference [Zhang 2021].

Compared to bulk perovskite materials, enhanced environmental stability has been observed in two-dimensional (2D) hybrid perovskites. This is because in a 2D perovskite structure, large incorporated organic ligands effectively protect the BX_6 octahedral cages [Lin 2018, Smith 2014]. 2D perovskites as layered materials

can be structurally derived from the bulk materials by tailoring along $< 100 >$ crystallographic direction [Mitzi 1995, Liang 2020]. In Fig.1.8, we can see that the interlayer separation and thickness of the BX_6 octahedral layers can be tuned through the choice of large organic cations during crystal growth. The large organic cations do not fit into the octahedral structure. In fact they play as a "barrier" and "cap" the bulk perovskites, which lead to the formation of the layered structure. Generally, the chemical formula for these layered perovskites is $A'_2A_{n-1}B_nX_{3n+1}$ ($1 \leq n \leq \infty$), where A′ represents a large organic cation such as monoammonium (R-NH_3^+) and diammonium (^+H_3N-R-NH_3^+, R refers to an alkyl chain or aromatic ligand) cations [Zhang 2021]; A refers to a small monovalent cation such as methylammonium, formamidinium or cesium; B is a divalent heavy metal cation such as lead or tin; X represents a halide; and n stands for the number of BX_6 octahedral layers.

2D perovskites can be considered as a novel class of materials with confined structure, which possess excellent physical properties. In 1986, Maruyama et al. firstly reported this new layered material; lead based organic -inorganic hybrid halide perovskites with $n = 1$ [Dolzhenko 1986]. In 1988, Ishihara et al. studied the excitonic state in 2D $(C_{10}H_{21}NH_3)_2PbI_4$ perovskite. They found that the exciton has a large binding energy of 370 meV and is very stable even at room temperature [Ishihara 1989]. Large exciton binding energy reduces the photovoltaic performance of layered perovskites due to the confined quantum well structure. However, it makes 2D perovskites promising candidates for light emitting diodes (LED) application because of the high-efficient radiative recombination resulting from their ideal quantum well structure [Zhang 2021, Bohn 2018, Vescio 2022, Yuan 2020]. The first LED device based on layered perovskite was reported in 1994 by Era et al., who fabricated a $C_6H_5C_2H_4NH_3PbI_4$ perovskite emitter with an excellent electroluminescence at liquid nitrogen temperature [Era 1994]. In 2014, Tan et al. reported the first room temperature LED device based on the layered $CH_3NH_3PbI_{3-x}Cl_3$ perovskite with highest external quantum efficiency (EQE) and internal quantum efficiency of 0.76% and 3.4%, respectively [Tan 2014]. Since then, significant progress has been achieved in 2D perovskite-based LEDs devices, where the EQE has exceeded 23% [Bao 2023].

1.3 Excitonic properties of two-dimensional perovskites

The extraordinary structural and opto-electronic properties in 2D perovskite semiconductors, make them promising candidates for the applications of solid state lighting, ultrahigh-definition displays and low-threshold lasers [Liu 2023, Qin 2020, Zhang 2021]. To further propel and realize their industrial applications, a deep understanding on the fundamental physical properties is vital. In this section, we summarize the excitonic properties in 2D perovskite materials, mainly including excitons in 2D quantum well system and exciton fine structure splitting.

1.3.1 Excitons in bulk semiconductors

When semiconductor materials absorb a photon with an energy equal to or higher than the band gap, the electron in the valence band will be excited to the conduction band. The hole in the valence band and the excited electron in the conduction band are bound by the attractive Coulomb potential, [Pelant 2012]

$$U(r) = -\frac{e^2}{4\pi\epsilon_0\epsilon r}, \tag{1.3}$$

where r is the electron-hole separation, ϵ is the dielectric constant of the material, ϵ_0 represents the vacuum permittivity and e is the elementary charge. The electron-hole pair generally referred to as an exciton. Depending on the strength of Coulomb

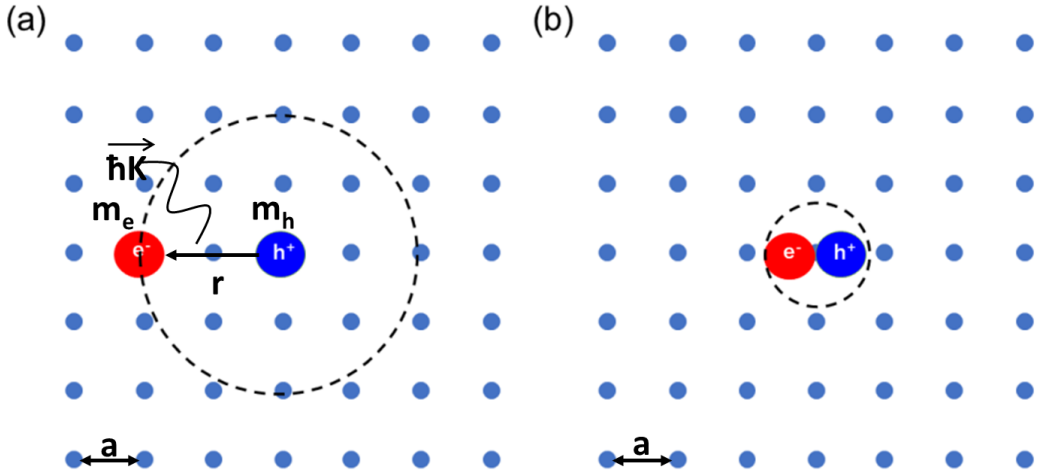

Figure 1.9: Schematic of a (a) Wannier exciton and a (b) Frenkel exciton. a represents the lattice constant, r is the exciton radius, m_e and m_h are the effective masses of electron (e) and hole (h), respectively, and $\hbar K$ is the quasi-momentum belonging to the translational movement of the exciton centre of mass. Figure reprinted after reference [Yuan 2019].

interaction, excitons can be divided into two limiting cases. Excitons with a weak electron-hole interaction which are weakly bound due to the large dielectric constant are usually called Wannier excitons, as shown in Fig.1.9 (a). A Wannier exciton extends over many unit cells, and usually its radius r is much larger than the lattice constant a, but its binding energy is small, typically on the order of 10 meV. In the other case, in materials with small dielectric constant, such as ionic crystals and organic molecule semiconductors, excitons with a strong electron-hole interaction which are tightly bound to a unit cell are usually named Frenkel excitons. The size of a Frenkel exciton is usually the same order as the size of the unit cell, as shown in Fig.1.9 (b). However, the binding energy of a Frenkel exciton is much larger, which can be up to a few hundred meV [Yuan 2019].

An exciton can be treated as a quasi-particle. In the case of Wannier excitons, the excitonic energy states in 3D semiconductors can be described by a hydrogen-like Bohr model,

$$E_n^{3D} = \frac{m_r/m_0}{\epsilon^2}\frac{1}{n^2}R_y = \frac{R_y^*}{n^2} \tag{1.4}$$

where $n = 1, 2, 3...$ is the orbital quantum number, m_0 is the free electron mass, ϵ is the dielectric constant, $R_y = -13.6\,\text{eV}$ represents the Rydberg constant, and m_r is the exciton reduced mass corresponding to the electron and hole masses,

$$\frac{1}{m_r} = \frac{1}{m_e} + \frac{1}{m_h}. \tag{1.5}$$

When the Rydberg constant R_y is substituted by an effective Rydberg constant

$$R_y^* = \frac{R_y m_r}{m_0 \epsilon^2}, \tag{1.6}$$

excitonic states are expressed in the same formation as for the hydrogen atom. Here R_y^* accounts for the fact that the dielectric environment of excitons is different from the vacuum environment, and the masses of the carriers are renormalized compared to the free electron mass. Due to the large dielectric constant, the Coulomb interaction is effectively screened by the dielectric environment, and this, together with the smaller effective masses of the electrons and holes, leads to a much smaller effective Rydberg constant for excitons in semiconductors, with typical values of a few to a few tens of meV. The exciton binding energy (E_b) is the separation of ground excitonic state ($n = 1$) from the continuum ($n = \infty$), which is equal to R_y^*. Typical exciton binding energy in bulk perovskites are for example 16 meV in bulk $MAPbI_3$ [Miyata 2015], 10 meV in bulk $FAPbI_3$ [Galkowski 2016] and 26 meV in bulk $CsPbBr_3$ [Bohn 2018] at room temperature.

Perovskite materials as direct-band gap semiconductors, the onset of the absorption edge can be described (in the so called dipole approximation and without considering the exciton effects) by the square-root law

$$\alpha(h\nu) \approx (h\nu - E_g)^{1/2}, h\nu \geq E_g. \tag{1.7}$$

The absorption of Wannier excitons, as shown in Fig.1.10, arise from transitions from the $|0\rangle$ state to the ground state ($n = 1$) or the higher excited excitonic states ($n = 2, 3...$). In absorption, we usually observe a hydrogen-like series of the excitonic lines at energies [Pelant 2012]

$$h\nu = E_g - \frac{E_b}{n^2}, n = 1, 2, 3, ...\infty; \tag{1.8}$$

Due to the relatively small exciton binding energy in bulk perovskites (compared to the thermal energy $K_B T \simeq 26\,\text{meV}$ at $T = 300\,\text{K}$), the observation of an exciton is usually possible only at low temperatures.

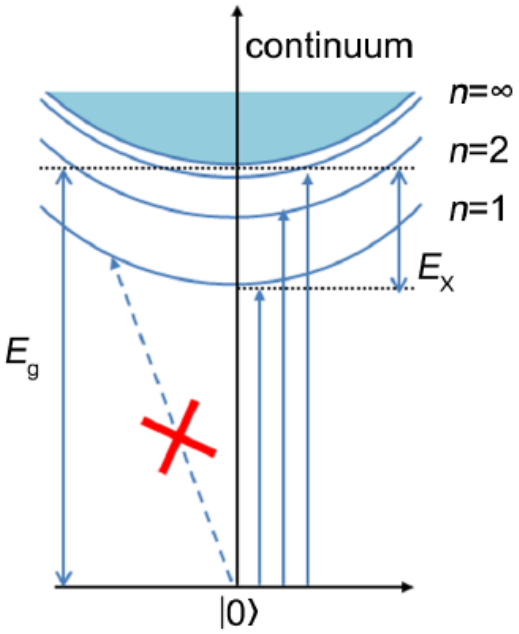

Figure 1.10: Schematic of the exciton dispersion relations $E = E(K)$ for the ground state ($n = 1$) and excited excitonic states ($n = 2, 3...$). Figure reprinted after reference [Pelant 2012].

1.3.2 Excitons in 2D perovskites

With the dimensionality of materials decreasing, the exciton binding energy increases due to the in-plane spatial confinement which leads to a stronger spatial overlap of the hole and electron wave functions. The dimensionality-dependent exciton binding energy of the 1s exciton ($n = 1$) can be described as [He 1991]

$$E_b = (\frac{2}{\alpha - 1})^2 E_{b,3D} \tag{1.9}$$

where α is the dimensionality of the system. In a perfect 2D system, $\alpha = 2$, the corresponding exciton binding energy is 4 times larger than in the 3D system. For 2D layered perovskites, with the thickness d of the octahedral slabs increasing, α increases from 2 and begins to approach 3, giving rise to the decreasing of exciton binding energy.

A further enhancement of the exciton binding energy results from a reduction of the dielectric screening. From a 3D bulk to a 2D system, the dielectric screening is significantly decreased because the electric field between the electrons and holes extends outside of the sample (where the dielectric constant is much lower), as shown in Fig.1.11. The reduced dielectric screening dramatically enhances Coulomb interactions, leading to a further enhancement of the exciton binding energy [Chernikov 2014, Weidman 2017]. Typical exciton binding energies observed in 2D perovskites are a few hundred meV [Blancon 2018, Dyksik 2020, Bohn 2018],

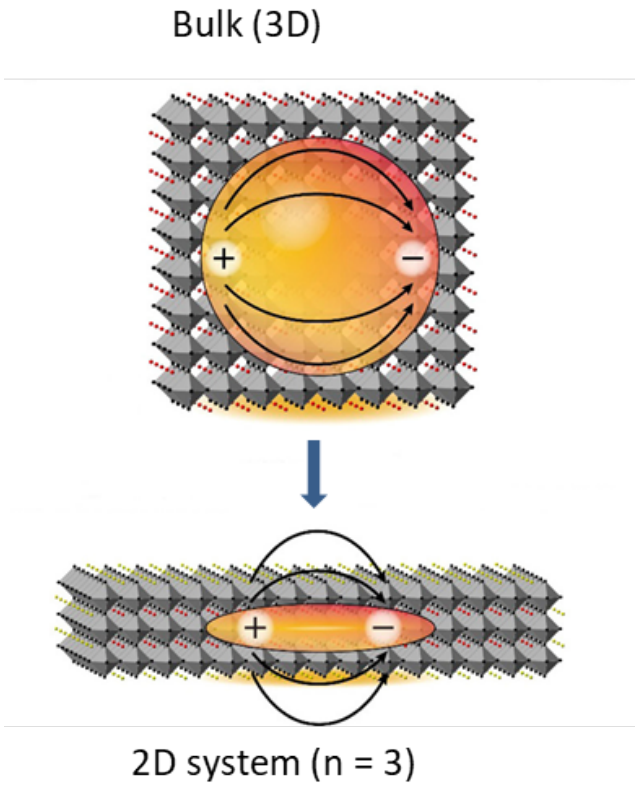

Figure 1.11: Real-space representation of electrons and holes bound into excitons for a 3D bulk and a 2D system ($n = 3$). Figure reprinted after reference [Weidman 2017].

which make excitonic effects in 2D perovskites dominate even at room temperature (considering the thermal energy $K_B T \simeq 26$ meV at $T = 300\,\mathrm{K}$).

Now we consider an inhomogeneous dielectric environment in a system of the 2D perovskite quantum well. In Fig.1.12, we show a schematics of 2D perovskite ($n = 1$) with the projection along the layer direction in panel (a) and its relevant energy diagram in panel (b). In this system, dielectric confinement is an electrostatic phenomenon, which results from a thin layer of the inorganic octahedral with a larger dielectric constant ϵ_1 sandwiched between the organic ligands with a smaller dielectric constant ϵ_2, as labeled in Fig.1.12 (b). According to Keldysh theory generalized to a semiconducting dielectric quantum well, the electrostatic force between charges in the higher dielectric constant ($\epsilon_1 \simeq 4$ or higher) octahedral rises due to the charge-generated electric field extending into the lower dielectric constant ($\epsilon_2 \simeq 2.2$) medium where it is screened less effectively [Keldysh 1979, Blancon 2018, Straus 2018]. So dielectric confinement effect is also called image charge effect. The significant difference in Coulomb forces in the higher dielectric constant octahedral renormalizes the energy levels, leading to the increase of the exciton binding energy. Assuming that charge carriers are confined to the

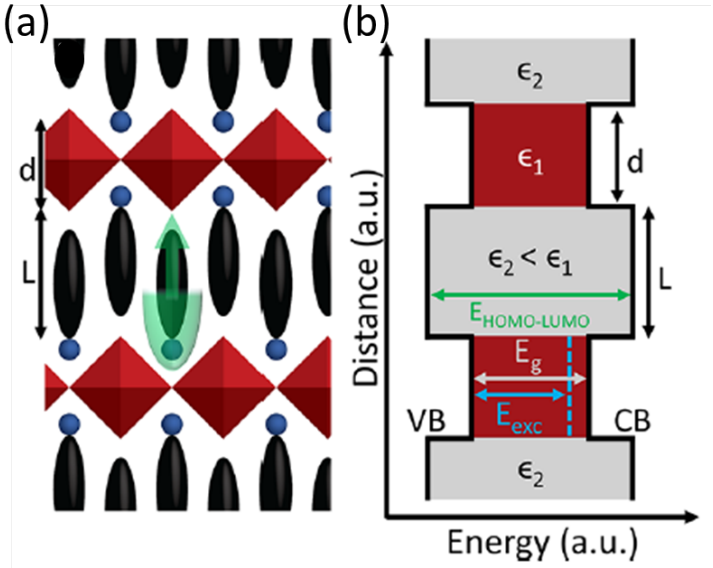

Figure 1.12: (a) Schematic of a projection along the layers of 2D perovskite, showing the alternation of organic (blue and black) and inorganic octahedral (red) layers for $n = 1$ with octahedral layer thickness d and organic layer thickness L. Highlighting (green) indicates the restriction solely on the cross-section area, but not the length of the organic cation. (b) Energy diagram corresponding to the 2D structure in panel (a). Relevant labels are: Conduction band CB, valence band VB, electronic band gap E_g (gray), optical band gap E_{exc} (blue) of the inorganic framework and the larger $HOMO - LOMO$ gap of the organic cations (green). The inorganic framework (red areas) has a dielectric constant ϵ_1, which is larger than the dielectric constant ϵ_2 of the organic framework (gray areas). Figure reprinted after reference [Straus 2018].

inorganic quantum well by an infinite barrier together with assuming a two-band model with separable wave functions by using first-order perturbation theory and an approximate model, the change in exciton binding energy [Straus 2018]

$$\triangle E_b \approx 2 \left(\frac{\epsilon_1 - \epsilon_2}{\epsilon_1 + \epsilon_2} \right) \left(\frac{q^2}{\epsilon_1 \epsilon_0 d} \right) I, \tag{1.10}$$

where ϵ_0 is the vacuum permittivity, q is the fundamental charge, and I is a factor of approximately unity [Mathieu 1992, Andreani 1990]. Equation 1.10 provides a simple model to describe the confinement effects in 2D perovskites. However, it is not possible to define parent 3D organic and inorganic components from which to extrapolate their properties [Straus 2018].

Quantum and dielectric confinement effects in 2D perovskites also increase the band gap. Quantum confinement shifts the valence and conduction bands by $\hbar^2\pi^2/2m_{e,h}d^2$, where d is the quantum well thickness, as shown in Fig.1.12 (b), m_e and m_h are the electron and hole masses. Therefore, with the inorganic oc-

tahedral layers decreasing, the band gap increases. Moreover, the band gap can also be modified by a change of the dielectric environment. The change in Coulomb forces in the high dielectric constant material renormalizes the energy levels, further increasing the band gap [Straus 2018, Raja 2017].

1.3.3 Exciton fine structure splitting

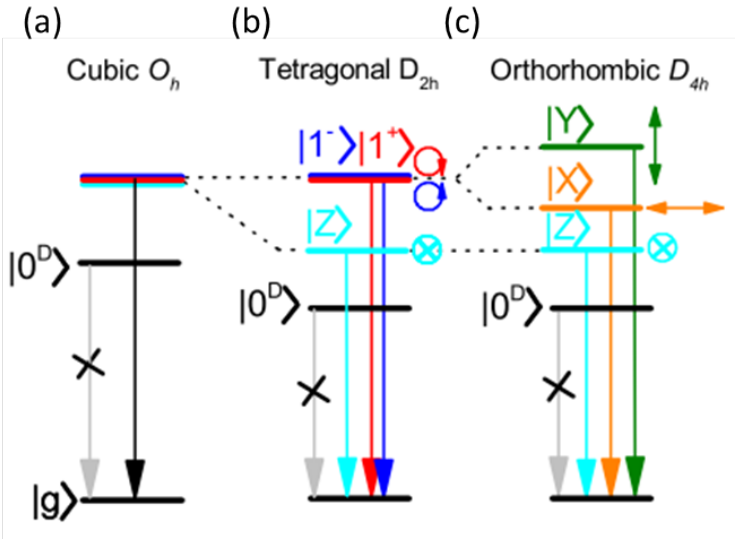

Figure 1.13: Schematic showing the exciton fine structure for the cubic (O_h symmetry), tetragonal (D_{2h}) and orthorhombic (D_{4h}) crystal structures of perovskite and expected circular or linear polarization of the optical transitions. Figure reprinted after reference [Baranowski 2019].

The Coulomb interaction between an electron from the spin-orbit split-off p-like conduction band ($J^e = 1/2, J^e_z = \pm 1/2$, see Fig.1.7 (c) band A) and a hole from the s-like valence band ($J^h = 1/2, J^h_z = \pm 1/2$) leads to the stabilization of a new excitation (band-edge exciton) which energy is lowered compared to the corresponding band-to-band transition. Here J^e and J^h are total angular momentum of electron and hole, respectively, and J_z is the angular momentum along z projection. Due to the strong electron-hole exchange interaction, band-edge exciton state is split into several energy sublevels at zero magnetic field, known as exciton fine structure. Generally, the electron-hole exchange energy is proportional to the integral [Bayer 2002]

$$E_{exchange} \propto \int\int d^3r_1 d^3r_2 \Psi^*_X(\mathbf{r}_e = \mathbf{r}_1, \mathbf{r}_h = \mathbf{r}_2) \times \frac{1}{|\mathbf{r}_1 - \mathbf{r}_2|} \Psi_X(\mathbf{r}_e = \mathbf{r}_2, \mathbf{r}_h = \mathbf{r}_1), \tag{1.11}$$

where Ψ_X is the exciton function and $\mathbf{r}_e$ and $\mathbf{r}_h$ are the electron and hole coordinates, respectively. In the case of the cubic structure of perovskites, the exciton state splits into four excitonic states: an optically inactive dark state $|0^D\rangle$ with total

angular momentum $J = 0$ and an optically active bright triplet with total angular momentum $J = 1$. The relevant energy diagram schematically shown in Fig.1.13 (a). With the symmetry reduction, the degeneracy of the bright triplet is lifted. In the tetragonal symmetry, bright exciton states split into two degenerate state $|1^{\pm}\rangle$ ($J_z = \pm 1$) with in-plane dipole orientation which couple to left-and right-handed circularly polarized light, and an excitonic state $|Z\rangle$ ($J_z = 0$) with out-of-plane dipole moment orientation, as shown in Fig.1.13 (b). The further symmetry reduction in the orthorhombic crystal field lifts the degeneracy of the in-plane bright $|1^{\pm}\rangle$ state, giving rise to symmetric and antisymmetric states $|X\rangle = (|1^{+}\rangle + |1^{-}\rangle)/\sqrt{2}$, $|Y\rangle = (|1^{+}\rangle - |1^{-}\rangle)/\sqrt{2}$ which couple to the two linearly perpendicular polarizations of light, respectively, as shown in Fig.1.13 (c) [Baranowski 2019].

Chapter 2

Experimental Methods

Contents

All of the experiments were performed in the Laboratoire National des Champs Magnétiques Intenses-Toulouse (LNCMI-T), which is one of a few pulsed magnetic field labs in the world, generating magnetic fields up to 98.8 T (nondestructive record in Europe) and 150 T (semi-destructive). This chapter briefly describes the experimental methods used in this thesis, including the preparation of nanoplatelets thin films, the pulsed magnetic field installation and magneto-optical spectroscopy.

2.1 Preparation of nanoplatelets thin films

The perovskite nanoplatelets investigated here are planar and ultra-thin perovskite sheets embedded between long organic ligands, which stabilize the colloids. Fig.2.1 schematically shows layered hybrid perovskite nanoplatelets with a varying number n of lead-halide octahedral sheets in each layer [Walters 2018]. Here the long organic ligands are hexylammonium, and A is a cation, which typically will be an inorganic cation such as Cs. The $CsPbBr_3$-based nanoplatelets were produced in the group of Alexander Urban at the Ludwig-Maximilians-Universität München (LMU). These colloidal nanoplatelets were synthesized by a reprecipitation method at room temperature, and the thickness, varying from 2-4 lead-halide octahedra planes (2-4ML), can be precisely controlled by altering the molar ratio of the precursors. First of all, 0.1 mmol Cs_2CO_3 (cesium carbonate, 99 %) powder was dissolved in 10 mL oleic acid at 100 °C under continuous stirring to obtain the Cs-oleate precursor. Similarly, the Pb-Br_2 precursor was prepared by dissolving 0.1 mmol Pb-Br_2 (lead(II)

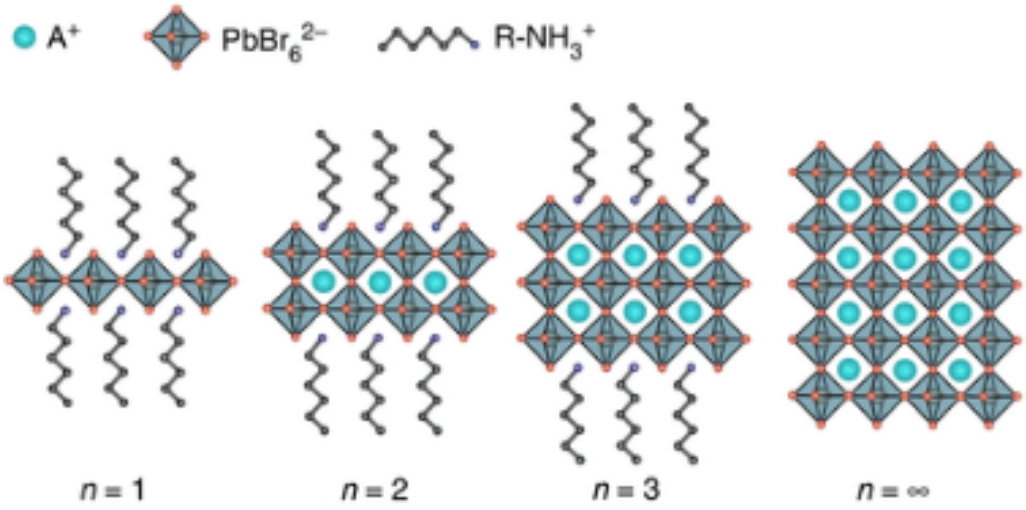

Figure 2.1: Schematic showing layered hybrid perovskite nanoplatelets, with a varying number n of lead-halide octahedral sheets in each layer. Figure reprinted after reference [Walters 2018].

bromide, $\geq$ 98 %) powder in 10 mL toluene at 100 °C, as well as 100 μL each of oleylamine and oleic acid was added to solubilize Pb-Br_2 better in toluene.

In order to obtain 2 ML nanoplatelets, 150 μL Cs-oleate precursor solution was dropped into 3 mL $PbBr_2$ precursor solution under vigorous stirring at room temperature. After 5 s, acetone was added into the mixed solution to initiate the formation of 2ML nanoplatelets. After 1 minute of stirring, the solution was centrifuged at 4000 rpm for 3 minutes, after which the precipitate was redispersed in 2 mL of hexane. It is worth noting that the thickness of the nanoplatelets can be precisely determined by the ratio of the precursors. For 3 ML, the volume of the Pb-Br_2 precusors solution is 1.5 mL and for 4 ML is 1.2 mL, synchronously keeping other steps and conditions the same as for the synthesis of 2 ML thick nanoplatelets. Further details on the samples synthesis can be found in the literature [Gramlich 2021, Gramlich 2022a]. Fig.2.2 presents the $CsPbBr_3$-based nanoplatelets solutions with thicknesses from 2 ML to 4 ML. These highly dispersed nanoplatelets solutions show a characteristic difference in color even under natural light. The 4 ML nanoplatelets show a bright yellow color, which becomes progressively lighter for 3 ML and 2 ML solutions.

In order to have fresh samples, we made the thin films at LNCMI-T using the colloidal solutions synthesized in Germany. To drop cast, the nanoplatelets solution was drawn into a syringe and then dripped, drop by drop, onto a 1.8×5 mm glass substrate, which we had previously ultrasonically cleaned in ethanol and dried with dust free air. The thin films were deemed to ready when the glass substrates acquired a yellowish colour. Representative thin films of 3 ML and 4 ML thick nanoplatelets are shown in the inset of Fig.2.2. The yellow colour of the thin film

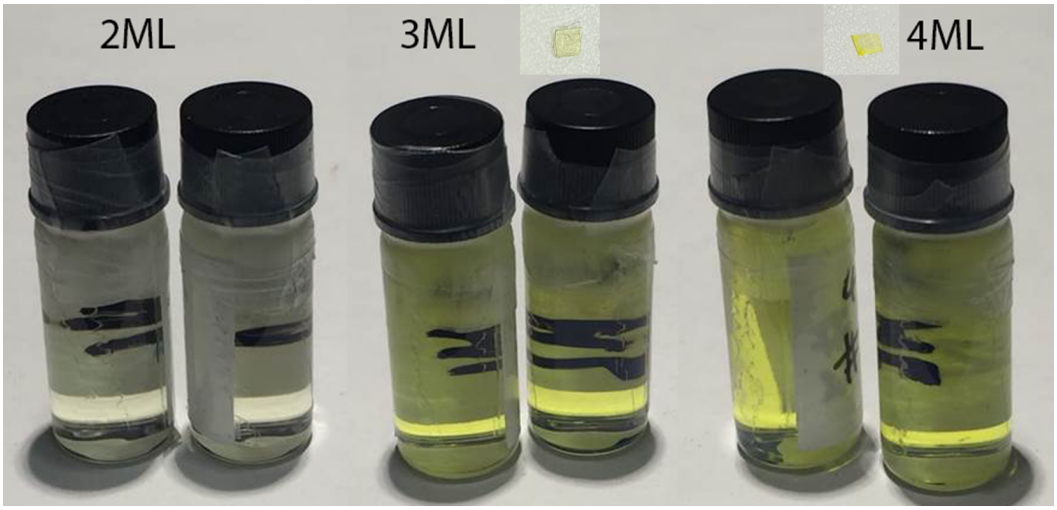

Figure 2.2: $CsPbBr_3$-based nanoplatelets solutions with the thickness from 2-4 lead-halide octahedra planes (2-4 ML). The inset shows representative drop cast thin films for 3 ML and 4 ML nanoplatelets.

provides a reliable indication that there are enough nanoplatelets on the surface of the glass substrate. This is particularly crucial for transmission measurements, in which white light passing through the thin film is absorbed by the nanoplatelets. If there is not enough nanoplatelets on the glass surface, the transmission spectrum will be identical to the original white light spectrum which is treated as a reference, and the absorption of the nanoplatelets will be too weak to detect. For instance, since the 2 ML nanoplatelets solution is almost transparent, in order to have an exploitable transmission spectrum, with a sharp peak and a narrow line width, we have to drop cast this solution repeatedly, until the glass substrate acquires a yellowish colour. Only then, were the freshly drop cast thin films, installed in the cryostat for transmission measurements in pulsed magnetic field.

2.2 Pulsed magnetic field setup

In order to explore the magneto-optical properties of the samples at low temperature, a custom optical setup has been built at LNCMI-T which functions with the pulsed high magnetic field installation. The pulsed magnetic field is generated by discharging electrical energy from capacitor banks into a resistive coil. The resistive coil is installed inside a liquid nitrogen (LN_2) cryostat, which maintains the coil temperature around 77 K. A specially designed helium (He) cryostat is inserted into the magnet bore in order to provide lower temperatures for the sample, down to $\simeq 2\,\mathrm{K}$ when the helium bath is pumped. A light transmitting probe, with investigated samples, is installed into the He cryostat. Near the sample there is a calibrated thermometer, and a calibrated pick-up coil, which are used to monitor the experimental conditions of the temperature and the magnetic field, respectively.

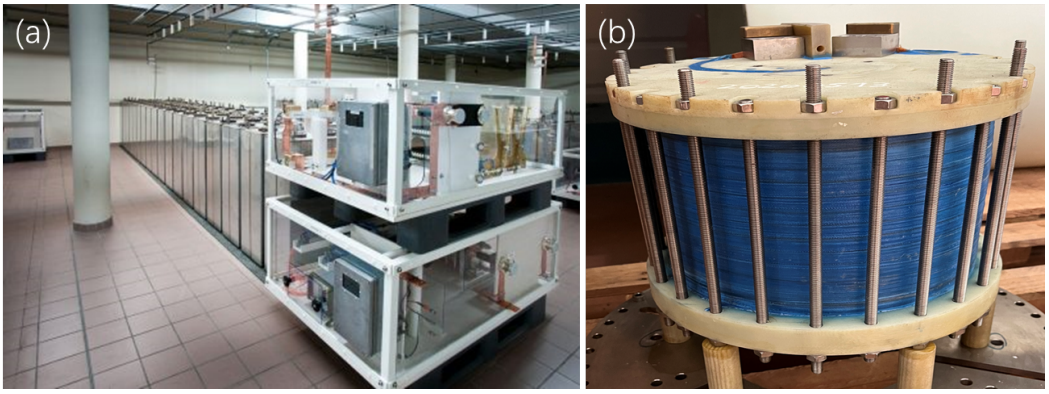

Figure 2.3: (a) The 14 MJ capacitor bank at LNCMI-T; (b) a resistive coil capable of generating magnetic fields up to 70 T with a usable magnet bore of 13 mm at LN_2 temperatures.

2.2.1 Generator

The generator group in LNCMI-T has designed and constructed three different capacitor banks (14 MJ, 6 MJ and 1.15 MJ) in order to energize the resistive coils. All capacitor banks can be charged to voltages up to 24 kV. Fig.2.3 (a) shows the 14 MJ capacitor bank, which consists of 14 capacitor units, with each unit storing a maximum of 1 MJ energy, with total capacitance of 48 mF.

2.2.2 Resistive coil

To fulfill the demands of different intensities of magnetic fields, different kinds of resistive coils have been designed and fabricated in the technical workshops of LNCMI-T. The biggest challenge for the coil is how to withstand the high pressure exerted by the magnetic field during the pulse, which results from the Lorentz force due to the charge carriers moving in the coil wire. The mechanical strain including tangential expansion and axial compression is proportional to B^2, which means that the higher the magnetic field, the larger is the force on the coil, with a maximum pressure at the peak value of the pulsed field. To withstand the induced mechanical strain, the coil is made up of specially designed copper stainless steel-(CuSS) wires reinforced with Zylon fibers, further protected by additional winding wires outside. Fig.2.3 (b) presents a 70 T single coil with a 13 mm diameter bore at LN_2 temperatures.

The duration of the single coil pulse varies from a few tens to a few hundred of milliseconds, depending on which generator is used, as well as the coil size. Fig.2.4 shows the temporal profile of the pulsed magnetic fields as a function of time for different coils which are labelled from A to F, respectively, accompanied with the maximum magnetic fields and the required energy to reach the maximum field value. Both A and B are 60 T single coils, which are designed to have different sizes. A has a 13 mm inner bore and connects to a 1 MJ capacitor bank, generating a 100 ms

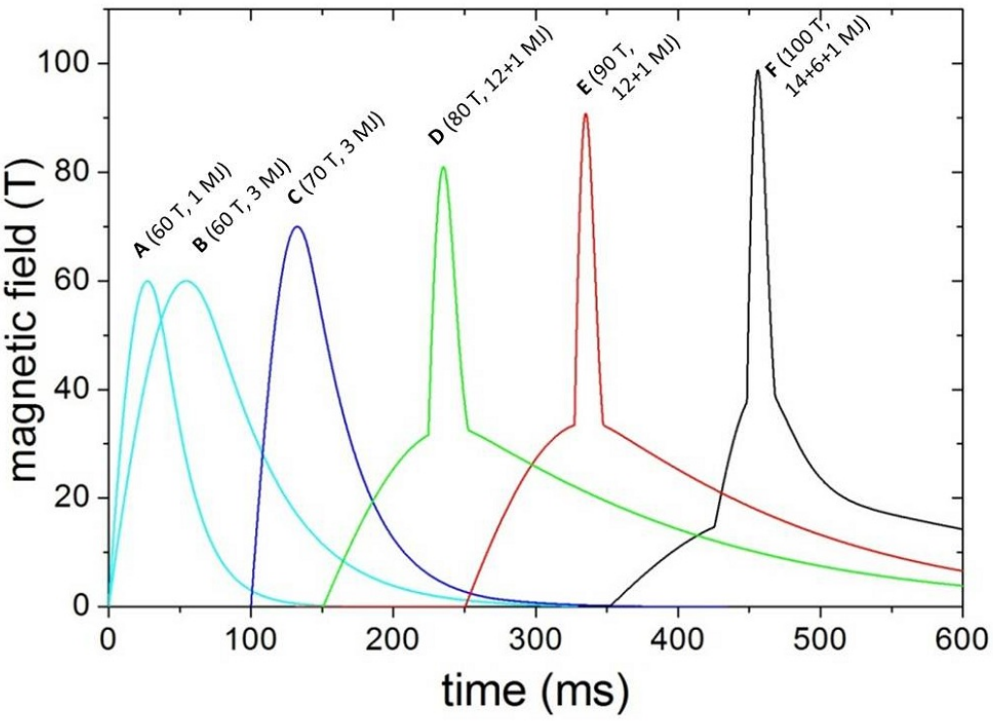

Figure 2.4: Temporal profiles of the pulsed magnetic fields as a function of time for different magnets. Maximum magnetic field pulse and energy required for each magnet are indicated for each curve. Results are shown for single coils (A-C), double-coils (D-E) and a triple-coil (F), which are energized by 1, 2 or 3 capacitor banks, respectively.

duration pulse. B has a 28 mm inner bore and connects to a 3 MJ capacitor bank, giving rise to a 200 ms duration pulse. C is a 70 T single coil. The typical duration of this coil is 150 ms if the 3 MJ generator bank is used for charging the coil.

Currently, a single coil can only supply magnetic field pulses up to 70 T. To obtain higher magnetic fields, multi-coil systems have been designed. D and E in Fig.2.4 are 80 T and 90 T double-coils. Both of these have an outer coil which is energized by a 12 MJ generator, and an inner coil which is energized by a 1.15 MJ generator. By synchronizing the maximum fields that the outer and the inner coils produce, a total pulsed field which can be up to 80 T or 90 T is created, with both having a rise time of $\simeq$ 75 ms. Similarly, in order to obtain a $\simeq$ 100 T magnetic pulse, a triple-coil including an outer coil, a middle coil and an inner coil which are respectively energized by a 14 MJ, a 6 MJ and a 1 MJ generator, to generate a 98.8 T pulse, which is the European record today [Béard 2018]. The temporal profile of this triple-coil (F) is shown in Fig.2.4. The magnet used in our magneto-optical setup is a 70 T single coil with 13 mm bore diameter, energized by the 14 MJ

capacitor bank.

2.2.3 Cryogenic system

The cryogenic system includes a liquid nitrogen (LN_2) cryostat and a helium cryostat. Fig.2.5 (a) shows a LN_2 cryostat installed with a 70 T magnet, a He cryostat and a transmission probe. The LN_2 cryostat is for cooling the magnet, while the He cryostat is for measurements. Special electrode connects the magnet to the generator. The LN_2 cryostat is filled with the liquid nitrogen to maintain the coil, and the outside of the tail of the He cryostat, at 77 K. This is important to minimize the temperature rise of the coil during a pulse due to the energy dissipation originating from resistive losses in the coil wires. Liquid nitrogen not only protects the safety of the coil during the pulse, but also cools the temperature of the coil to the normal after the pulse. Usually, it takes about one hour to cool down after a high field shot. However, the cooling time can be shortened to some extent by pumping on the cryostat in order to decrease the temperature of the LN_2 bath.

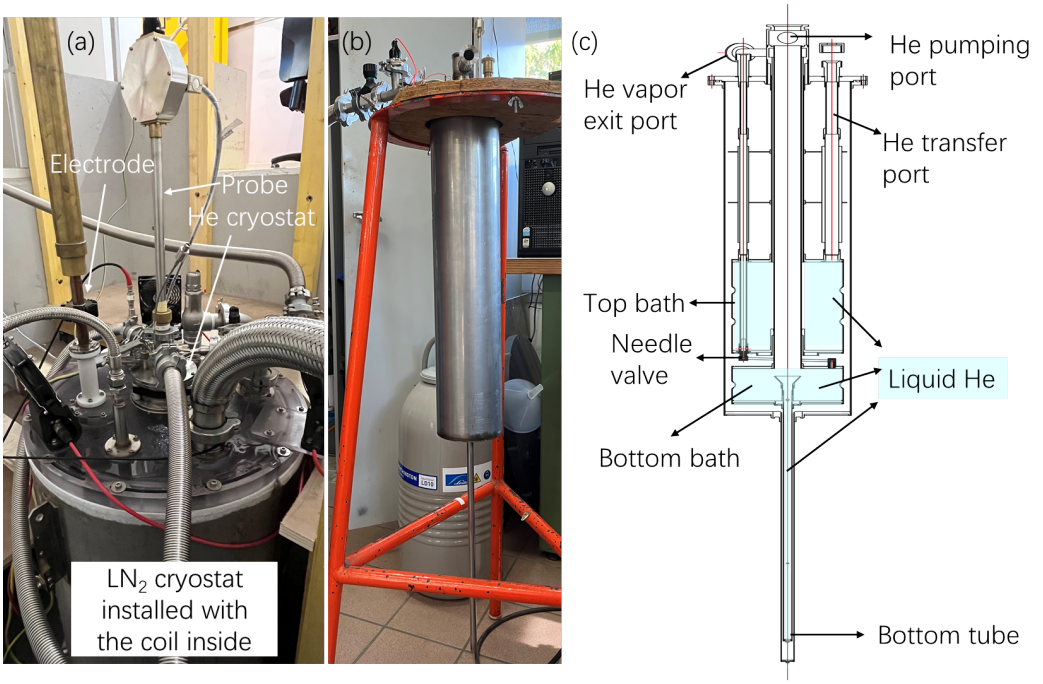

Figure 2.5: (a) A liquid nitrogen cryostat equipped with a transmission probe, a 70 T helium cryostat and a 70 T coil (not visible). (b-c) a picture and a schematic view of the 70 T liquid helium cryostat.

In order to have a low sample temperature, a helium cryostat has been designed to fit the LN_2 bore of the coil. A photograph of a 70 T liquid helium cryostat prior to installation in the LN_2 cryostat is shown in Fig.2.5 (b). To maximise use of the available magnet bore diameter (13 mm), and to reduce the cryogenic heat load, the tail of the He cryostat is made from thin walled stainless steel tube with

outer diameter 12 mm. The inner tube has an internal diameter of 7.5 mm, which accepts the 7 mm diameter of transmission probe. Fig.2.5 (c) schematically shows the inside system of the He cryostat. Liquid He is transferred from a He dewar into the top He bath through the He transfer port. The top bath used to store liquid helium, and the bottom bath (tail of cryostat) are separated by a needle valve. By pumping on the liquid He in the bottom bath through the He pumping port, the sample temperature can be lowered to $\simeq 2$ K. The evaporated He gas is sent to a special He recovery system for re-liquefaction.

2.3 Magneto-optical spectroscopy

In order to explore the optical properties of the samples in high magnetic field, a special setup, which allows us to measure both of the transmission and photoluminescence (PL) of the thin film sample in the magnetic field, has been built in LNCMI-T. Fig.2.6 schematically shows the drawing of this setup.

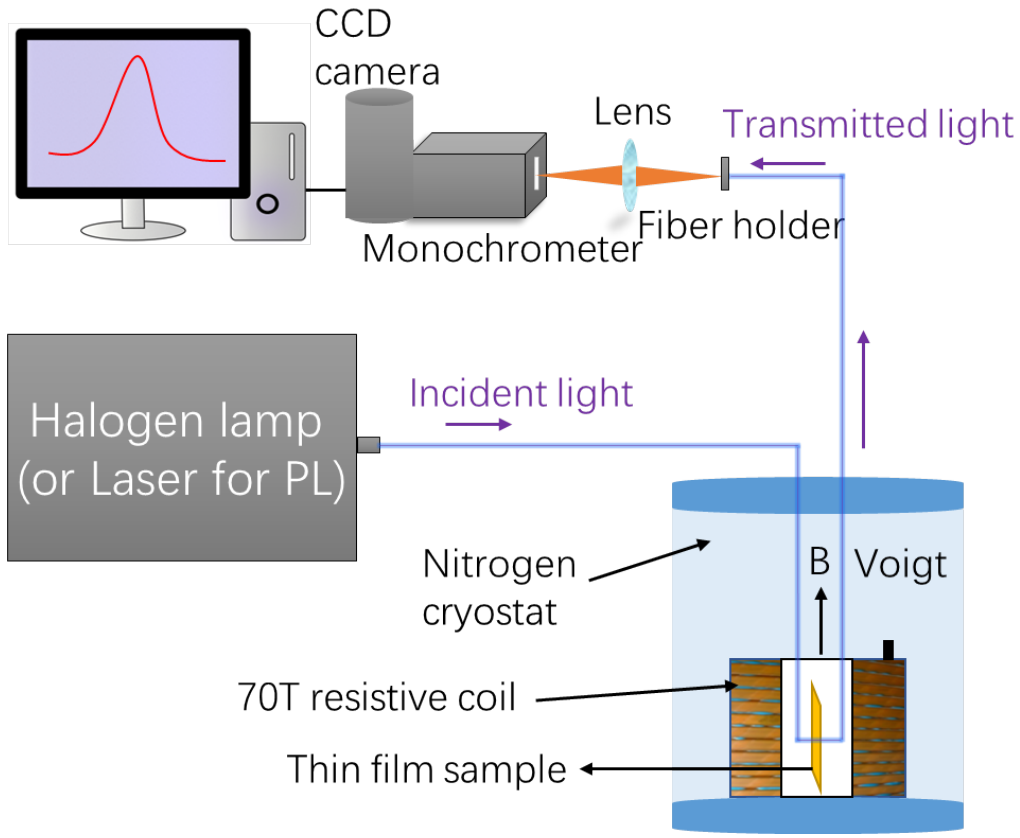

Figure 2.6: Schematic drawing (not to scale) of the transmission measurement in pulse magnetic field (shown here in the Voigt geometry). Same setup is also used for photoluminescence (PL) measurement in pulse magnetic field.

Generally, a thin film sample is placed in the center of the magnet. For magneto-

transmission measurement, A broadband Halogen lamp is used to provide the incident light using an optical fiber. The transmitted light collected by a second optical fiber, is dispersed by a monochromator equipped with a diffraction grating, and detected using a liquid nitrogen-cooled CCD camera, which is synchronized with the magnetic field pulse. Similarly, for magneto-PL measurement, we use a continuous wave laser as excitation, and we collect the emitted light from the sample which is sent to the monochrometer. In front of the slit of the monochrometer, we place a corresponding long pass filter to block the transmitted laser so that only the signal of the sample is detected.

2.3.1 Transmission probe

To install the sample into the magnet with both the Voigt geometry ($\mathbf{k} \perp \mathbf{B}$, $\mathbf{k}$ is the light wave vector and $\mathbf{B}$ is the magnetic field) and the Faraday geometry ($\mathbf{k} \parallel \mathbf{B}$), a special transmission probe has been designed, as shown in the Fig.2.7 (a). Multi-mode optical fibers, shown in Fig.2.7(a-b), are used to guide the incident light and transmitted light.

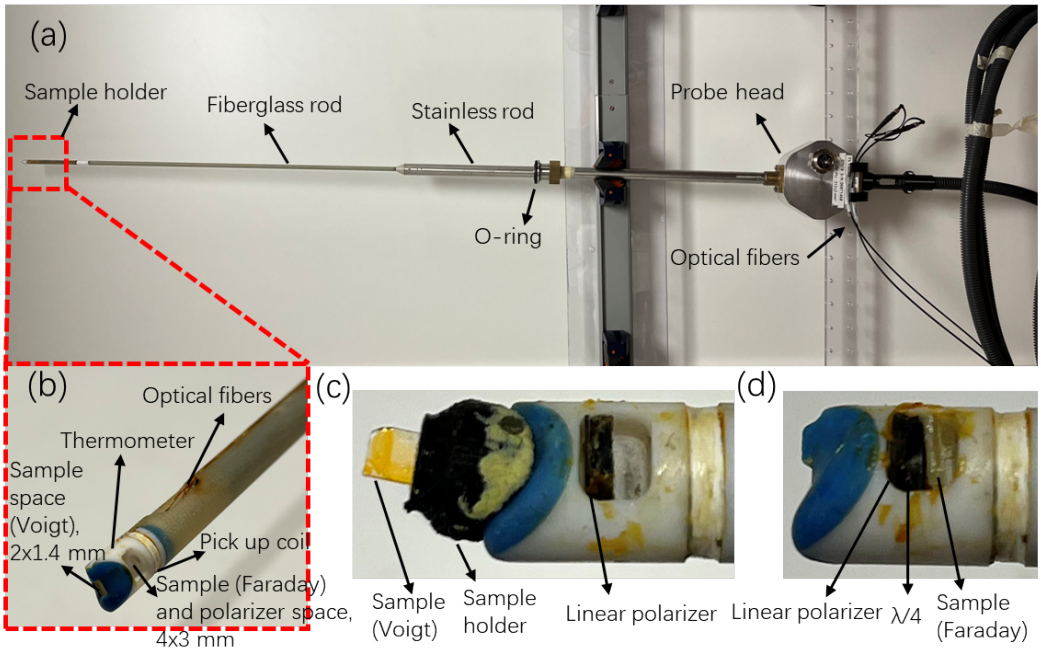

Figure 2.7: (a) A complete picture of the transmission probe; (b) The zoomed image of the sample holder; (c) Sample and polarizer attached in the probe for Voigt geometry and (d) Faraday geometry.

For transmission measurement, the incident light, usually from a broadband halogen lamp, is guided by the input fiber with a diameter of 200 μm, while the transmitted light is collected by an output fiber with a diameter of 400 μm. For photoluminescence measurement, the excited light from a continuous wave laser is

guided by the input fiber to the sample, and the emitting light from the sample is collected by the output fiber and sent to the monochrometer. In the middle of the probe is an O-ring, which is used to seal the entry of the probe to the He cryostat. By adjusting the position of the O-ring on the stainless rod, the probe can be moved vertically in the cryostat to exactly adjust the position of the sample to be in the center of the magnetic field. The sample holder is located at the tip of the probe. A zoomed image is shown in Fig.2.7(b). The sample holder includes a pick-up coil, a thermometer, a 2×1.4 mm sample space designed for Voigt configuration and a 4×3 mm space for samples in Faraday configuration, and polarizers. For the sample in Voigt configuration, we need an extra holder to keep the sample horizontal in the sample space. The positions of the sample, as well as a relevant linear polarizer in Voigt configuration, are shown in Fig.2.7(c). Similarly, we also show the typical positions of the sample and polarizer in the Faraday configuration in Fig.2.7(d). From left to right inside the sample space, there are a linear polarizer sheet, a quarter-wave plate and the sample.

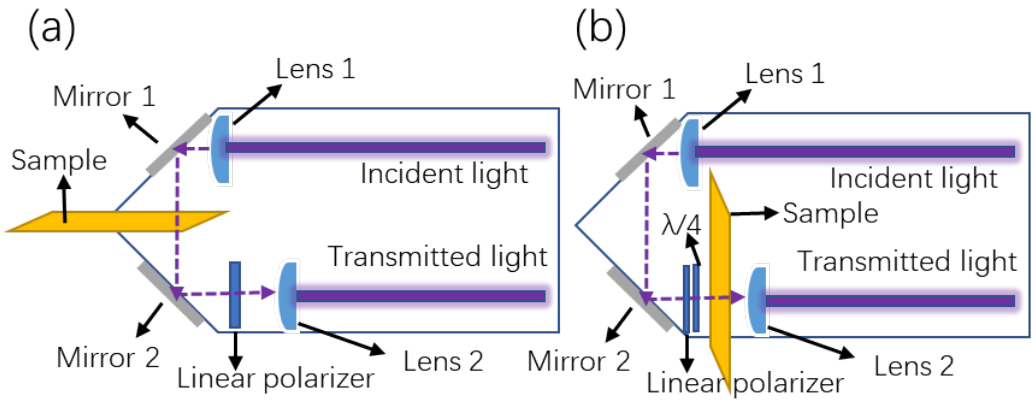

Figure 2.8: Schematics of the optical path for (a) Voigt and (b) Faraday configuration.

In order to better describe the sample holder, we schematically show the intrinsic optical path of the sample holder in both Voigt and Faraday geometries in Fig.2.8 (a-b). For the Voigt geometry the magnetic field is perpendicular to the propagation vector of light. The incident light is guided by a 200 μm input optical fiber to the first lens then focused onto the first mirror, which is angled at 45 degrees, so that the reflected light passes perpendicularly through the surface of the thin film sample. The transmitted light is reflected by the other 45 degree mirror, so that it passes perpendicularly through the linear polarizer sheet, is focused by the second mirror, and finally collected by a 400 μm output optical fiber and sent to the monochromator. Since this probe is vertically inserted into the magnet, the direction of the magnetic field is aligned along the probe, so that the magnetic field is perpendicular to the light wave vector on the sample.

For the Faraday geometry, the direction of magnetic field is along to the light

wave vector. To realize this geometry, a 4×3 mm space for the sample and also for additional polarizers has been designed, shown in Fig.2.7 (b). The incident light is guided by an input optical fiber to the first lens, the first mirror and the second mirror in sequence. After the light reflected by the second mirror, the propagation vector of light **k** is already along the magnetic field. The transmitted light is focused by the second lens and then collected by an output optical fiber, and delivered to the monochromator. For the perovskite samples in this thesis, the two in-plane bright states usually couple to the circularly polarized light. Hence, a linear polarizer sheet and a quarter-wave plate are used in front of the sample to adjust the excitation to be a circularly polarized excitation. The direction of the circular polarization is changed by reversing the direction of the magnetic field (polarity of the capacitor bank). Positive or negative magnetic field corresponds to the left-handed (σ^+) or right-handed (σ^-) circular polarization.

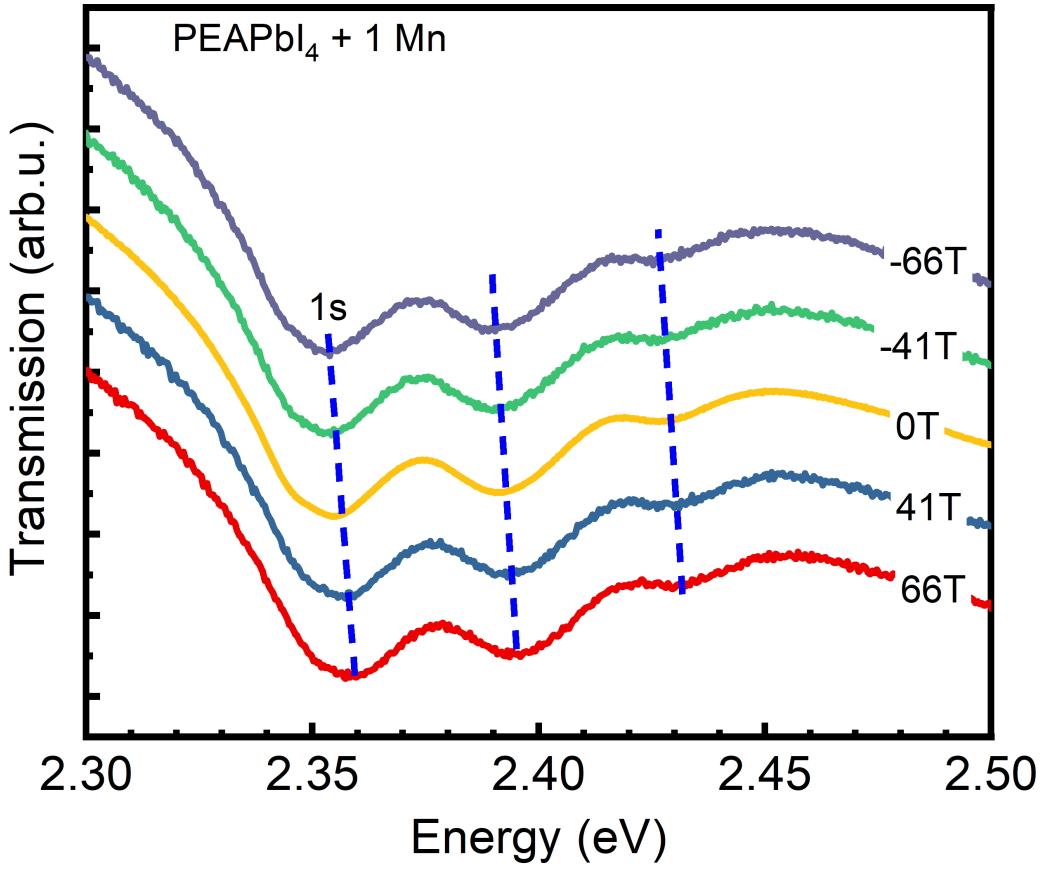

Figure 2.9: Circular polarization resolved transmission spectra of the $PEAPbI_4$ perovskite sample doped with 1% manganese for selected magnetic fields at $T = 2.2$ K. Reversing the magnet field direction allows us to detect in $\sigma\pm$ polarization. The dashed lines highlight the shift of the 1s state and the phonon replicas in magnetic field.

In Fig.2.9 we show preliminary circular polarization resolved transmission spectra in Faraday configuration for the sample of $PEAPbI_4$ perovskite doped with 1% manganese at selected positive and negative magnetic fields. The dashed lines highlight the shift of the 1s transition (and phonon replicas) in magnetic field. The transitions shift to higher or lower energy depending upon the direction of the magnetic field.

2.3.2 Pick-up coil

A pick-up coil is used for a number of important purposes. Primarily it is used to precisely monitor in real time the value of the magnetic field on the sample during the high field pulse. Generally, a pick-up coil is made of 100 turns of insulated copper wire with a diameter of 50 μm, mounted as close as possible to the sample.

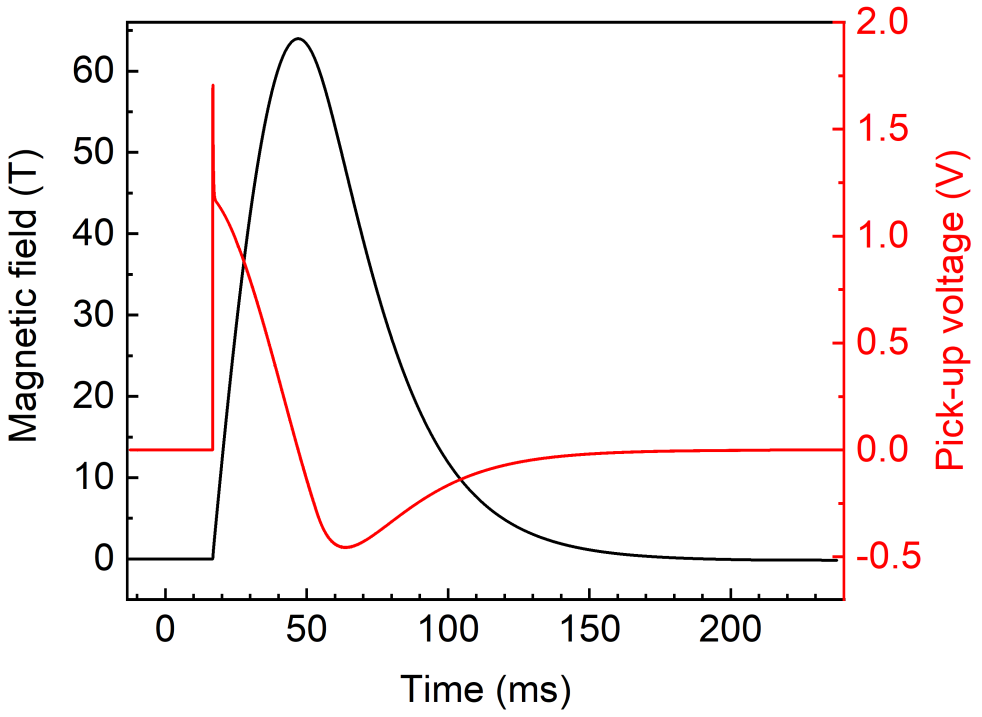

Figure 2.10: Pick-up voltage (red curve) and magnetic field (black curve) calculated using equation 2.1) as a function of time during a 66 T pulse.

During the magnetic pulse, the induced voltage (V) on the pick-up coil is the first derivative of the magnetic flux (ϕ),

$$V = -\frac{d\phi}{dt} = -N \times S\frac{dB}{dt}, \tag{2.1}$$

where N is the number of turns, S is the surface of one spire and $N \times S$ is the effective area of the whole pick-up coil. Therefore, the value of magnetic field (B) can be obtained from the integrated pick-up voltage divided by the effective area. It is therefore crucial to know the exact value of the effective area.

To determine the effective area, the pick-up coil is installed in the center of 1 m long calibration coil, with a known $B(I)$ dependence. Using the oscillator output of a lock-in amplifier, a sinusoidal magnetic field is induced in the calibration coil, and the voltage of the pick-up coil is also recorded simultaneously. As the voltage and the magnetic field are known, the effective area of the pick-up coil can be precisely obtained according to the equation 2.1. In Fig.2.10 we show the measured voltage (red curve) on the pick-up coil during a 66 T magnetic field pulse. The magnetic field (black curve) is calculated using equation 2.1.

The pick-up coil is also used to precisely center the sample in the magnetic field. For this, the oscillator output of a lock-in amplifier is used to inject a small alternating current into the pulsed field coil. The alternating magnetic field induces a voltage on the pick-up coil which is proportional to the magnetic field. Monitoring the pick-up voltage, while moving the sample holder vertically, allows us to find the position at which the voltage, and therefore the magnetic field, are a maximum. At this position, the pick-up coil, and therefore the sample, are perfectly centered in the resistive pulsed field coil.

Last but not least, monitoring the pick-up coil for voltages spikes and other anomalies during the magnetic field pulse, can be used to detect potential problems with the resistive coil. Resistive coils with anomalies, which often develop slowly over time, are retired for disassembly in order to diagnose the origin of the problem. This prevents catastrophic explosions, with loss of samples and equipment, and also provides information to improve the design of the next generation of pulsed coils.

2.3.3 Thermometer

A DT-670 silicon diode is used as our thermometer to accurately record the temperature from 2 K (pumped helium conditions) to 295 K (room temperature). The position of this thermometer (placed as close as possible to the sample) is shown in Fig.2.7 (b). A diode thermometer is based on the temperature dependence of the forward voltage drop in a p-n junction biased at a constant current, typically 10 μA supplied by a Lake Shore temperature controller [LakeShoreCryotronics-company 2022]. A standard response curve of voltage verses temperature with a 10 μA excitation is presented in Fig.2.11. During the measurement, the temperature is monitored according to this voltage/temperature relationship and the value of temperature is shown by the Lake Shore temperature controller, which is connected to the thermometer via the probe head.

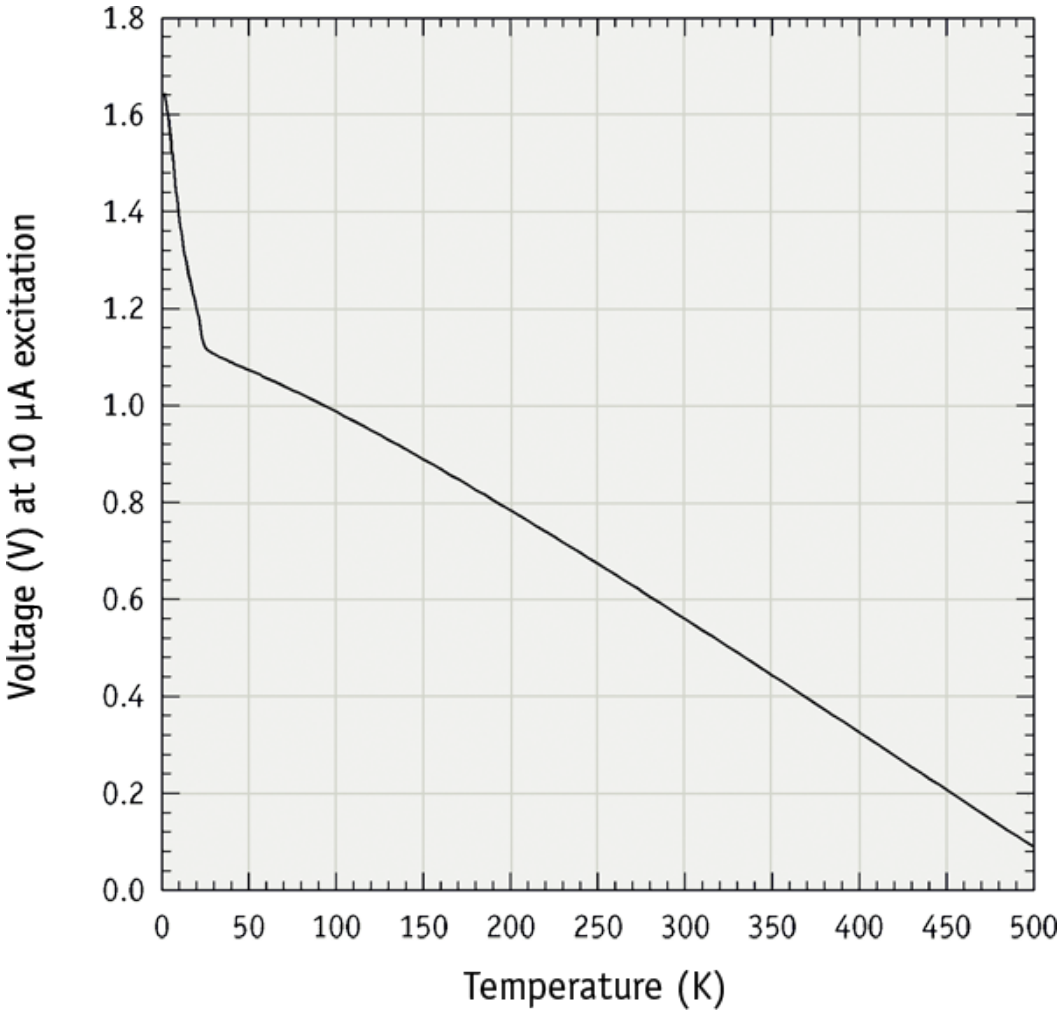

Figure 2.11: Standard voltage/temperature relationship at a constant 10 μA current of diode thermometer on the transmission probe [LakeShoreCryotronics-company 2022].

2.3.4 Synchronization

Fig.2.12 schematically describes the setups in both the optical room and the magnetic field room (bunker), as well as the 14 MJ generator. Considering the duration of the 70 T magnetic field pulse is only 150 ms, the available time to acquire a spectrum at a constant value of magnetic field is typically only 2-4 ms. To synchronize the magnetic field pulse with the spectral acquisition, which is crucial for the magneto-optical experiment, a system has been built for the temporal synchronization with a precision of 0.1 ms. The detailed process is as follows:

First of all, in order to pre-trigger the CCD camera, the 14 MJ generator sends an optical continuous signal to the trigger box by an optical fiber, and the trigger box converts this optical signal into an electrical pulse with 500 ms duration and

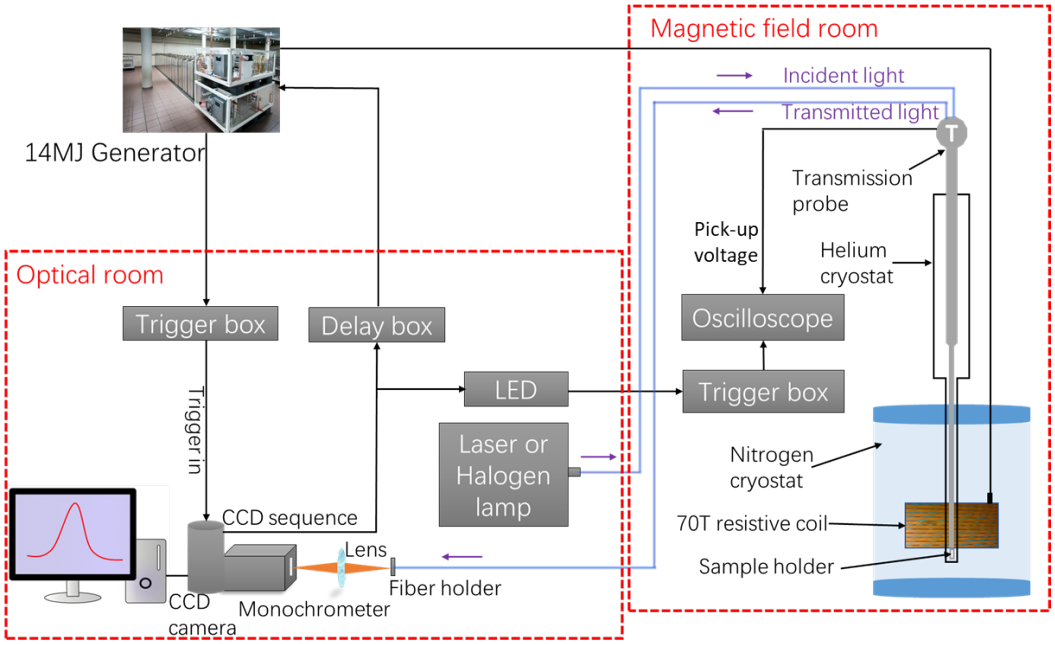

Figure 2.12: Schematic graph of synchronization sequence for magneto-optical spectroscopy.

then delivers it to the CCD.

Next, a sequence of square waves produced by the CCD camera is sent in two paths: one path is to the numerical oscilloscope in the magnetic field room and the other is back to generator. For the former path, a LED is used in the optical room to transformed the electrical signal into an optical signal. Then the optical signal is guided by an optical fiber to the trigger box in the magnetic field room. The trigger box converts again the optical signal into electrical signal then sends it to oscilloscope. For the latter path, the CCD sequence is received by a delay box, which is used here to adjust the delay time so that the maximum of the magnetic field is in the center of one of the CCD square wave frames, as the Fig.2.13 shows. The delay box converts the electrical CCD sequence into 500 ms single optical signal and then sends it to the generator. Afterwards, the generator discharges the electrical energy into the coil for the pulse.

Finally, the voltage of the pick-up coil is recorded by the oscilloscope during the pulse. According to the equation 2.1, the magnetic field as a function of time can be calculated by integrating the voltage. Combining the data of CCD square wave simultaneously recorded by the oscilloscope after the pulse, the magnetic field and CCD square wave as a function of time can be plotted, as the Fig.2.13 shows. The red rectangles represent the CCD square wave, and each acquisition lasts 2 ms.The black curve comes from a 67 T pulse. By setting the delay time to 16.5 ms, the sixth acquisition corresponds exactly to the maximum value of the magnetic field.

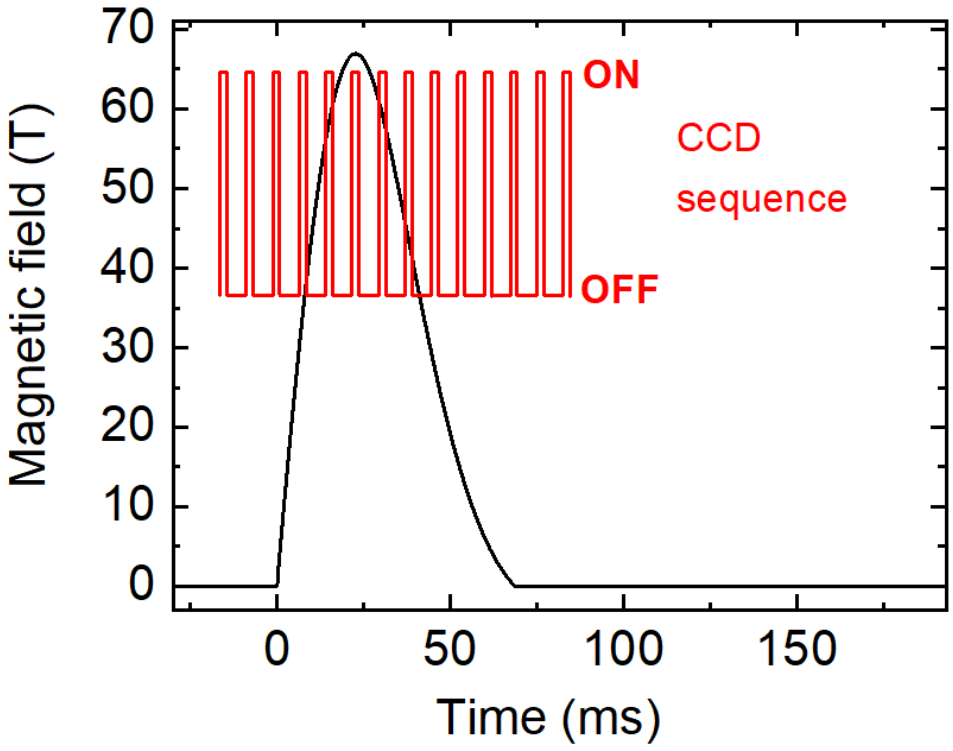

Figure 2.13: Magnetic field (black curve), obtained from the integrated pick-up coil voltage using equation 2.1) and the CCD sequence (red curve) as a function of time during a 67 T pulse. The CCD acquires a spectrum during each maximum of the square wave.

Chapter 3

Magneto-optical spectroscopy on $CsPbBr_3$-based nanoplatelets

Contents

*In this chapter, the results of thickness-dependent dark-bright exciton splitting in $CsPbBr_3$-based nanoplatelets, revealed via magneto-optical spectroscopy are presented. By applying large in-plane magnetic fields up to 65 T, the optically inactive dark states of $CsPbBr_3$-based nanoplatelets were brightened for the first time. We demonstrate that the optically inactive dark state is the lowest-lying state in these nanoplatelets with different thicknesses. With decreasing thickness of the inorganic octahedral, the dark-bright exciton splitting increases due to the enhanced exciton confinement. Moreover, the magneto-photoluminescence (PL) spectrum suggests that the dark and the bright state populations are non-thermalized, which supports the presence of a phonon bottleneck in the exciton relaxation process. Finally, the experimental results for the out-of-plane state are discussed. They indicates that the out-of-plane bright states in 3 ML and 4 ML nanoplatelets might be the highest-lying states. The results presented in this chapter have been published in Nano Letters, **22**, 7011-7019 (2022)*

3.1 Introduction

Perovskite nanoplatelets are atomically planar, two-dimensional ultra-thin sheets of semiconductors, which exhibit significantly larger exciton binding energy compared

to their bulk counterparts, due to the strongly enhanced quantum and dielectric confinement. In this chapter, we investigate the excitonic properties of $CsPbBr_3$-based nanoplatelets with different lead-halide octahedral layers, which were synthesized by the group of Alexander S. Urban from Ludwig-Maximilians-Universität München in Germany. The details of the sample synthesis and description are described in Chapter 2.1.

We start from a theoretical description of the excitonic states at zero magnetic field and in applied in-plane magnetic field. We then present the results of magneto-optical spectroscopy measurements on $CsPbBr_3$ nanoplatelets with different thicknesses of the lead-halide slabs, ranging from 2 ML to 4 ML. The optically inactive dark exciton state at zero magnetic field is brightened using large in-plane magnetic fields up to 64 T, which allows us to accurately determine the dark-bright exciton splitting of these nanoplatelets. The results of thickness-dependent dark-bright exciton splitting in $CsPbBr_3$ nanoplatelets indicate that with decreasing octahedral thickness of nanoplatelets, the dark-bright exciton splitting increases due to the strongly enhanced exciton confinement. Additionally, by calculating the ratio of the PL intensity between the dark states and bright states in magnetic field, we demonstrate that the exciton population is not thermalized (non Boltzmann distribution) at the moment of the recombination which can be attributed to the presence of a phonon bottleneck.

3.1.1 Exciton structure of $CsPbBr_3$ nanoplatelets at magnetic field

Band-edge exciton states in $CsPbBr_3$ nanoplatelets originate from the Coulomb interaction of an electron residing in the split-off P-like conduction band ($J^e = 1/2, J^e_z = \pm 1/2$) and a hole residing in the S-like valence band ($J^h = 1/2, J^h_z = \pm 1/2$), where J^e and J^h are the total angular momentum of the electron and hole, respectively, and J_z is the angular momentum projected along z. Due to the strong electron-hole exchange interaction, the band-edge exciton has four degenerate states; an optically inactive dark singlet state ϕ_D with total angular momentum $J = 0$ and an optically active bright triplet with total angular momentum $J = 1$. The bright triplet includes two excitonic states $\phi_\pm$ ($J_z = \pm 1$) with in-plane dipole orientation which couple to left-and right-handed circularly polarized light in the case of cubic or tetragonal crystal structure, as well as the excitonic state ϕ_z ($J_z = 0$) with out-of-plane dipole moment orientation. For lower symmetries of the crystal structures, the degeneracy of the in-plane bright states is lifted, giving rise to states that couple to two perpendicular linear polarization components. However, the splitting between the two in-plane bright states is expected to be quite small, compared to the bright-dark splitting. We schematically show these four band-edge excitonic states at zero magnetic field in the center panel of Fig.3.1. The $|0\rangle$ state represents the ground state.

In external magnetic field, the intrinsic symmetry of the crystal is broken, and the excitonic states are no longer eigen-states of the zero magnetic field Hamiltonian. In the Voigt configuration ($\mathbf{B} \perp \mathbf{k}$), the effective Hamiltonian H_V can be written in

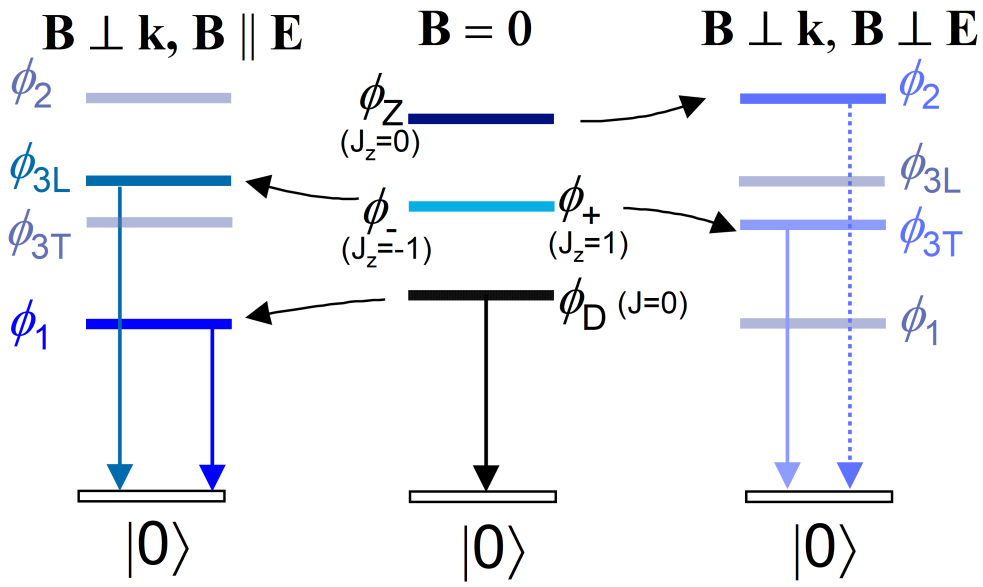

Figure 3.1: Schematics of the exciton structure of $CsPbBr_3$ nanoplatelets at zero magnetic field (center) and with in-plane magnetic field ($\mathbf{B} \perp \mathbf{k}$) with the light electric field vector $\mathbf{E} \parallel \mathbf{B}$ (left) and $\mathbf{E} \perp \mathbf{B}$ (right).

the basis of the zero field states as

$$H_V = \begin{bmatrix} E_1 & 0 & -\xi B & \xi B \\ 0 & E_2 & \eta B & \eta B \\ -\xi B & \eta B & E_3 & 0 \\ \xi B & \eta B & 0 & E_3 \end{bmatrix}, \tag{3.1}$$

where ξ and η are coefficients dependent on the electron and hole g-factors, the spin–orbit coupling and the crystal field. The new eigenstates can nevertheless be obtained by using linear combinations of the zero-field exciton states, with dipole moments oriented longitudinally (labeled L) or transversally (labeled T) to the direction of the magnetic field

$$\phi_{1,3\mathrm{L}} = c_{1,3\mathrm{L}}\phi_{\mathrm{D}} + d_{1,3\mathrm{L}}(\phi_+ - \phi_-), \tag{3.2a}$$
$$\phi_{2,3\mathrm{T}} = c_{2,3\mathrm{T}}\phi_Z + d_{2,3\mathrm{T}}(\phi_+ + \phi_-). \tag{3.2b}$$

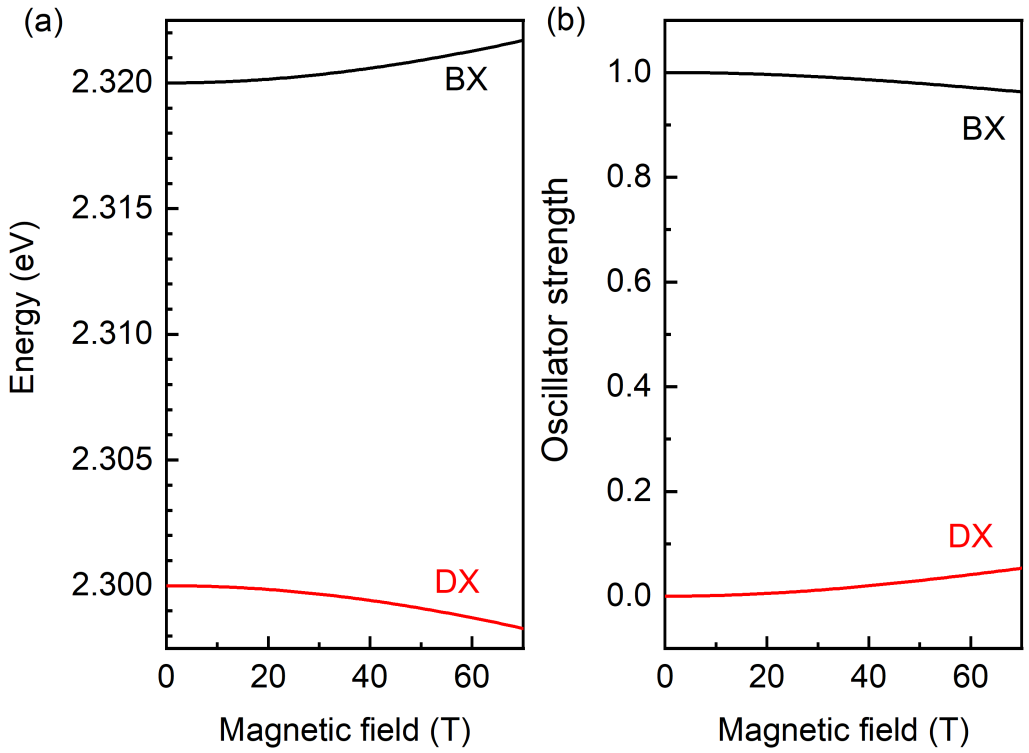

Figure 3.2: Excitonic transition (a) energy and (b) oscillator strength as a function of magnetic field in Voigt configuration ($\mathbf{B} \perp \mathbf{k}$). BX and DX represent bright exciton and dark exciton, respectively. In panel (a), the lines are the calculated transition energy using equation 3.4a. In panel (b), the lines are the calculated oscillator strength from equation 3.3a and equation 3.3b.

The coefficients $c_{1,3\mathrm{L}}$, $d_{1,3\mathrm{L}}$, $c_{2,3\mathrm{T}}$ and $d_{2,3\mathrm{T}}$ are given by

$$c_{1,3\mathrm{L}} = \frac{\frac{1}{\sqrt{2}} g_{\mathrm{L}} \mu_{\mathrm{B}} B}{\sqrt{2[E_{1,3\mathrm{L}}(B) - E_{\mathrm{D}}]^2 + \frac{1}{2}(g_{\mathrm{L}} \mu_{\mathrm{B}} B)^2}}, \tag{3.3a}$$

$$d_{1,3\mathrm{L}} = \frac{E_{\mathrm{D}} - E_{1,3\mathrm{L}}(B)}{\sqrt{2[E_{1,3\mathrm{L}}(B) - E_{\mathrm{D}}]^2 + \frac{1}{2}(g_{\mathrm{L}} \mu_{\mathrm{B}} B)^2}}, \tag{3.3b}$$

$$c_{2,3\mathrm{T}} = \frac{\frac{1}{\sqrt{2}} g_{\mathrm{T}} \mu_{\mathrm{B}} B}{\sqrt{2[E_{2,3\mathrm{T}}(B) - E_Z]^2 + \frac{1}{2}(g_{\mathrm{T}} \mu_{\mathrm{B}} B)^2}}, \tag{3.3c}$$

$$d_{2,3\mathrm{T}} = \frac{E_{2,3\mathrm{T}}(B) - E_Z}{\sqrt{2[E_{2,3\mathrm{T}}(B) - E_Z]^2 + \frac{1}{2}(g_{\mathrm{T}} \mu_{\mathrm{B}} B)^2}}, \tag{3.3d}$$

where $g_{\mathrm{L}} = g_{\mathrm{e}\perp} - g_{\mathrm{h}\perp}$ and $g_{\mathrm{T}} = g_{\mathrm{e}\perp} + g_{\mathrm{h}\perp}$ are the effective Landé g-factors for the longitudinal and transverse modes, $g_{\mathrm{e}\perp}$ and $g_{\mathrm{h}\perp}$ are the electron and hole g-factors perpendicular to the c-axis, respectively [Kataoka 1993, Surrente 2021, Dyksik 2021a].

The energy of the exciton states is described by

$$E_{1,3\mathrm{L}} = \frac{1}{2}\left[E_{\mathrm{D}} + E_{XY} \mp \sqrt{\left(E_{\mathrm{D}} - E_{XY}\right)^2 + \left(g_{\mathrm{L}}\mu_{\mathrm{B}}B\right)^2}\right], \tag{3.4a}$$

$$E_{2,3\mathrm{T}} = \frac{1}{2}\left[E_Z + E_{XY} \pm \sqrt{\left(E_Z - E_{XY}\right)^2 + \left(g_{\mathrm{T}}\mu_{\mathrm{B}}B\right)^2}\right], \tag{3.4b}$$

where E_{D}, E_{XY}, and E_Z represent the zero magnetic field energies of the dark state, the in-plane bright states, and the out-of-plane bright state, respectively.

In the Voigt configuration, the magnetic field mixes the in-plane excitonic states with the dark state and the out-of-plane bright state. In the longitudinal polarization ($\mathbf{B} \parallel \mathbf{E}$), the magnetic field mixes the dark state ϕ_1 with the in-plane bright state ϕ_{3L}, as shown in the left panel of Fig.3.1. The brightened dark state (DX) ϕ_1 couples to longitudinal polarized light and its energy E_1 decreases with increasing magnetic field, whereas, the energy of in-plane bright state (BX) E_{3L} simultaneously increases, as predicted by equation 3.4a, which is plotted in Fig.3.2 (a). According to equation 3.2a, the magnetic field transfers oscillator strength from the in-plane bright state ϕ_{3L} to the dark state ϕ_1, as shown in Fig.3.2 (b). According to equation 3.2b, the magnetic field also mixes the out-of-plane exciton state ϕ_2 with the other in-plane bright state ϕ_{3T}, as shown in the right panel of Fig.3.1. These states couple to transverse polarized light ($\mathbf{B} \perp \mathbf{E}$). With increasing magnetic field, the energy of $\phi_{3\mathrm{T}}$ state is expected to red shift, whereas the energy of ϕ_2 state is expected to blue shift according to equation 3.4b, as shown by the black dashed lines in Fig.3.2 (a).

3.2 Optical measurements on $CsPbBr_3$ nanoplatelets

3.2.1 Optical spectra at zero field

Let us start from the optical spectra of $CsPbBr_3$ nanoplatelets with thickness from 2 ML to 4 ML measured at zero magnetic field and at $T = 5\,\mathrm{K}$. In Fig.3.3, we show PL (red) and transmission (black) spectra for each thickness. For 2 ML to 4 ML nanoplatelets, the 1s excitonic transmission peaks can be observed at 2.90 eV, 2.69 eV and 2.60 eV in Fig.3.3 (a), (b) and (c), respectively. The high energy peak of the PL spectrum of 2 ML nanoplatelets (red curve in Fig.3.3 (a)) is around 2.90 eV, which is attributed to the recombination of the bright exciton. This PL shoulder is very close to the 1s excitonic resonance seen in the transmission spectrum (black curve in Fig.3.3 (a)), with a Stokes shift of $\simeq$6 meV. For 3 ML and 4 ML nanoplatelets, each PL spectrum is clearly dominated by a sharp and narrow peak, indicating the emission of the exciton ground state. The PL central peak position red shifts from $\simeq$2.66 eV to $\simeq$2.56 eV when the octahedral layers increasing from 3 ML to 4 ML. The small peak around 2.66 eV at high energy side of 4 ML PL spectrum (see Fig.3.3 (c)), is an additional emission from 3 ML nanoplatelets, which suggests that a small fraction of 3 ML nanoplatelets are formed in 4 ML nanoplatelets during the chemical synthesis. Compared to 2 ML nanoplatelets, the

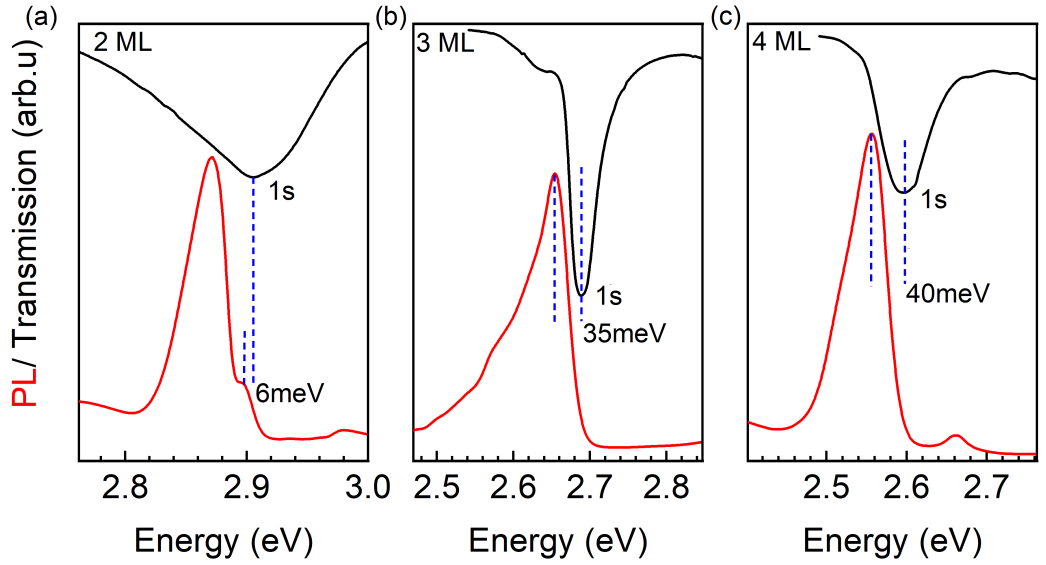

Figure 3.3: PL (red) and transmission (black) spectra of (a) 2 ML, (b) 3 ML and (c) 4 ML thick nanoplatelets at $T = 5\,\mathrm{K}$.

Stokes shifts between the PL and transmission spectra are considerably lager for 3 ML and 4 ML thick nanoplatelets ($\simeq$35 meV and $\simeq$40 meV shifts), as shown in Fig.3.3 (b, c), respectively.

In order to exactly determine the 1s excitonic transition energy and the band gap, in Fig.3.4, we have modeled the absorption spectra of 2 ML, 3 ML and 4 ML thick nanoplatelets with a generalized 2D Elliott formula [Elliott 1957, Shinada 1966, Campi 1995, Chen 2021],

$$\alpha(h\nu) = \frac{A}{\zeta}\frac{\Gamma(E_{ex})}{\left(\frac{\Gamma(E_{ex})^2}{4} + \left[\frac{h\nu - E_{ex}}{\zeta}\right]^2\right)} + B\frac{\frac{1}{2} + \frac{1}{\pi}\arctan\left[\frac{2(h\nu - E_g)}{\Gamma(E_g)}\right]}{1 + \theta(h\nu - E_g)\exp\left[-2\pi\left[\frac{h\nu - E_g}{E_b}\right]^{-1/2}\right]}, \tag{3.5}$$

where h is the Plank constant, ν is the photon frequency, A and B are the relative amplitudes of the exciton and free carrier absorption, ζ is a density-dependent broadening parameter, $\Gamma(E_{ex})$ is an energy-dependent broadening parameter and E_{ex} is an independent variable, which represents the transition energy, such as excitonic transition or band to band transition. $\Gamma(E_{ex})$ is described by the following formula

$$\Gamma(E_{ex}) = \frac{2\Gamma_0}{\exp\left[-3(h\nu - E_{ex})/k_B T\right] + 1}, \tag{3.6}$$

and k_B is the Boltzmann constant. For ground state (n = 1), the excitonic transition energy E_{ex} can be described by,

$$E_{1s} = E_g - E_b, \tag{3.7}$$

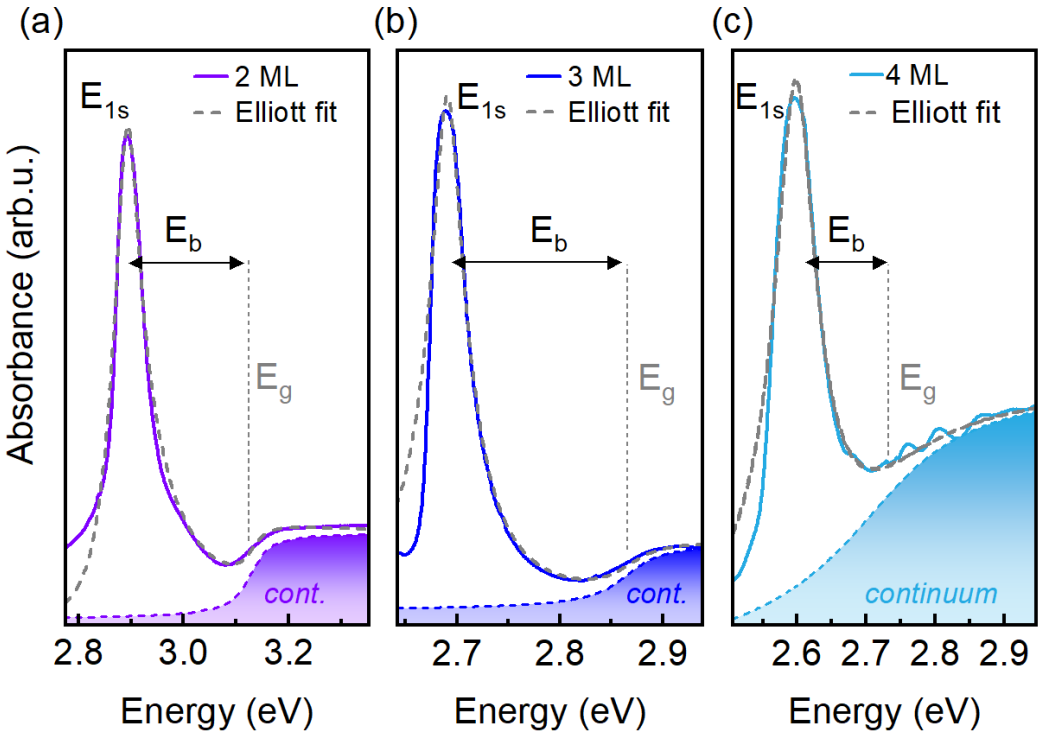

Figure 3.4: (a-c) Absorption spectra of 2-4 ML thick nanoplatelets (continuous lines) fitted using the Elliot formula, *i.e.* equation 3.5 (dashed gray lines). The contribution to the absorption spectrum from the continuum is shown as a shaded curve under each spectra.

and then the exciton binding energy is then,

$$E_b = E_g - E_{1s}. \tag{3.8}$$

We can directly obtain the parameters of the 1s excitonic transition energy E_{1s}, the band gap E_g and the exciton binding energy E_b by using Elliott's formula to fit the absorption spectra. The contribution to the absorption spectrum of the continuum is shown as a shaded curve under each spectrum in Fig.3.4 (a-c).

The extracted energies of the 1s exciton transition (E_{1s}) and band gap (E_g) by fitting the Elliott formula are plotted as a function of the nanoplatelet thickness in Fig.3.5 (a). We observe that both energies increase with decreasing thickness of the octahedral layers. This is because, on one hand, quantum confinement shifts the conduction and valence bands by $\hbar^2\pi^2/2m_{e,h}d^2$, where m_e and m_h are the mass of the electron and hole, respectively, and d is the quantum well thickness, and on the other hand, the change in Coulomb forces in the higher dielectric constant quantum well also renormalizes the energy levels, resulting in an increases of the band gap and the 1s excitonic transition energy with decreasing quantum well thickness d.

The quantum and dielectric confinement effects not only increase the band gap but also increase the exciton binding energy. In Fig.3.5 (b), we present the exciton

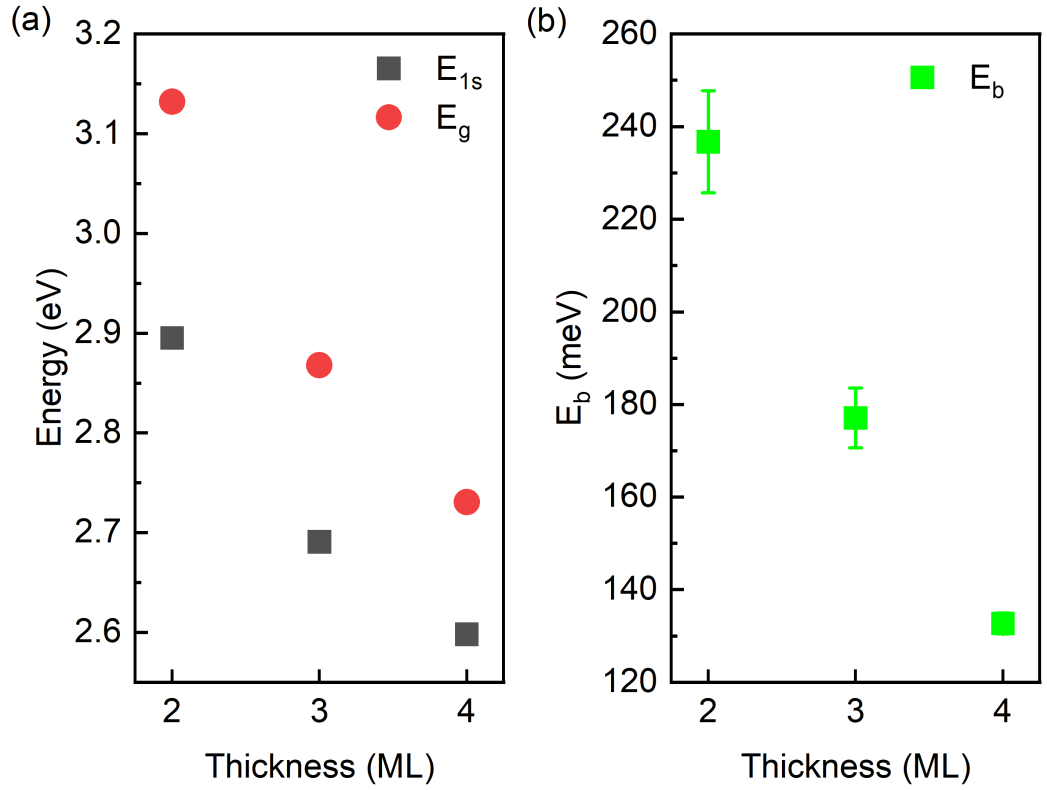

Figure 3.5: (a) Energies of the 1s exciton transition (E_{1s}) and band gap (E_g). (b) Measured exciton binding energy (E_b) as a function of nanoplatelet thickness.

binding energies (E_b) as a function of the nanoplatelet thickness. The exciton binding energy of 4 ML nanoplatelets is 133 meV. With decreasing thickness of the octahedral layers, the exciton binding energy increases up to 177 meV (3 ML) and to 237 meV (2 ML), due to the strongly enhanced quantum and dielectric confinement effects. This trend corresponds well to the reported result for 2D Ruddlesden-Popper halide perovskites $(BA)_2(MA)_{n-1}Pb_nI_{3n+1}$ (BA and MA stand for $CH_3(CH_2)_3NH_3$ and CH_3NH_3, respectively) with the number of layers n varying from 5 to 1, leading to the exciton binding energy increasing from 125 meV to 470 meV [Blancon 2018], and our previous result of 2D perovskites $(PEA)_2(MA)_{n-1}Pb_nI_{3n+1}$ (PEA represent $C_6H_5C_2H_4NH_3$) with n varying from 3 to 1 giving rise to the E_b increasing from 78 meV to 265 meV [Dyksik 2021b]. The E_b value of 237 meV of the thinnest nanoplatelets (2 ML), corresponds to the experimental results from Alexander Urban's group, who obtained a value 280 meV at room temperature [Bohn 2018], and from Jing Li's group who determined this value to be 127 meV [Li 2017]. Additionally, our result of $E_b = 237$ meV of 2 ML nanoplatelets also corresponds to the theoretical results from Maria Chamarro's group, who used a $k{\cdot}p$ approach including dielectric effects under the image charge formalism and a variational excitonic wave function and determined a value of 130 meV when the dielectric constant of

the organic barrier medium $\epsilon_2 = 2$ (close to the dielectric constant of glass, ligand or liquid) and a value of 190 meV when $\epsilon_2 = 1$ (vacuum or air) [Ghribi 2021].

3.2.2 Magneto-transmission spectra

Now, we turn to the optical spectra of $CsPbBr_3$ nanoplatelets measured at high magnetic fields up to 65 T in the Voigt configuration ($\mathbf{k} \perp \mathbf{B}$) and at $T = 2.2$ K. Here, we first show magneto-transmission spectra resolved in the longitudinal polarization ($\mathbf{E} \parallel \mathbf{B}$) of 2 ML, 3 ML and 4 ML thick nanoplatelets in Fig.3.6. For each sample, the line shape of the magneto-transmission spectra does not change with increasing magnetic field even up to 65 T, which suggests that the transmission feature is mainly related to the absorption of bright exciton (BX) states.

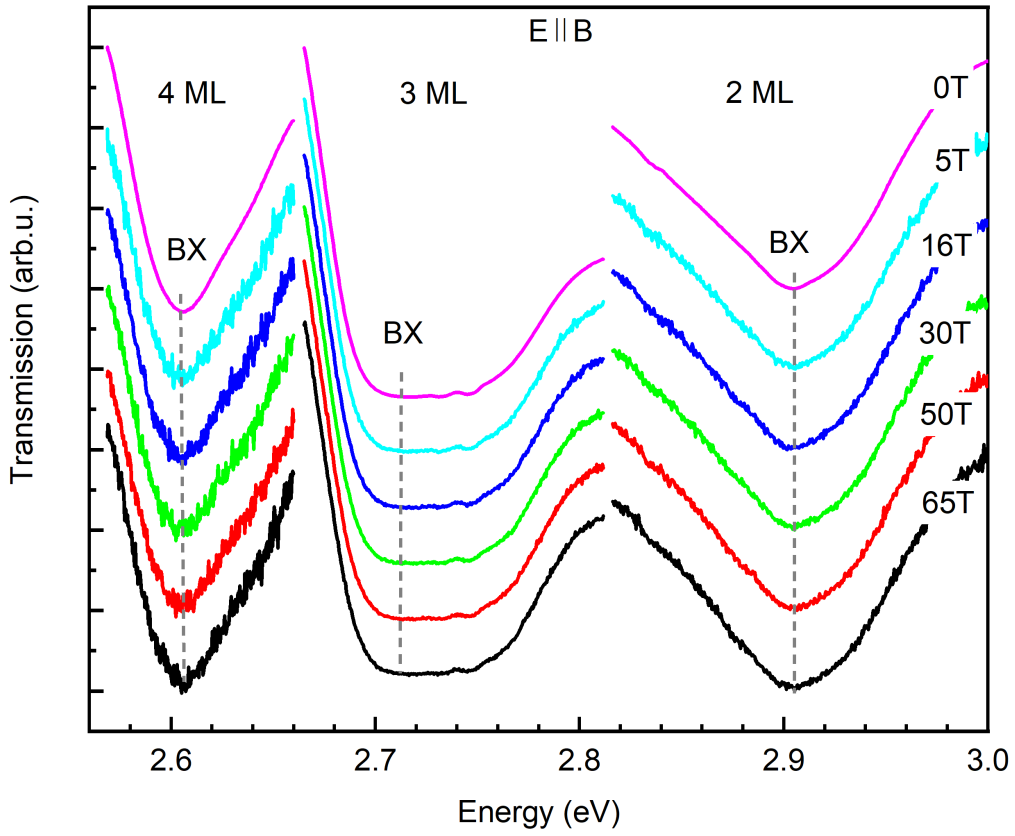

Figure 3.6: Transmission spectra of 2 ML, 3 ML and 4 ML thick nanoplatelets measured at the indicated values of magnetic field for $\mathbf{E} \parallel \mathbf{B}$. BX represents the bright exciton and the gray dashed lines are drawn a guide to the eye.

Due to the small shifts and large spectral broadening of 2 ML and 3 ML transmission spectra, to reliably extract the magnetic field dependence of the BX energy, we calculate the ratio spectra, *i.e.* transmission spectra measured at different magnetic fields divided by the zero magnetic field spectrum. Here we show the ratio

spectra of 2 ML and 3 ML samples in Fig.3.7 (a) and (b), respectively, to illustrate our fitting method. The ratio spectra have a characteristic sharp feature with a well defined amplitude, line width and position, despite the fact that the magnetic field induced shift of the transition energy with respect to the to zero field spectrum is very small. Due to the same line shape of the transmission spectra at high field and zero field, as Fig.3.6 shown, the ratio spectra can be expressed using the following formula,

$$\frac{T_B(E)}{T_0(E)} = \frac{AT_0(E+\Delta E)+C}{T_0(E)}, \tag{3.9}$$

where $T_B(E)$ and $T_0(E)$ are the transmission spectra at a given magnetic field and zero field. A and C are constants which take into account any possible change of the transmission amplitude or background during the field sweep. ΔE is the energy shift of the transmission resonance at a selected magnetic field. To extract the value of ΔE, we use the least-squares method to fit the experimental curves. In Fig.3.7 (a) and (b), blue curves are the calculated fits, which correspond very well to the experimental ratio spectra $T(B)/T(0)$. This method allows us to precisely extract the shift of excitonic transition even at a very low magnetic field, where the shift is small compared to the broadening of the absorption line.

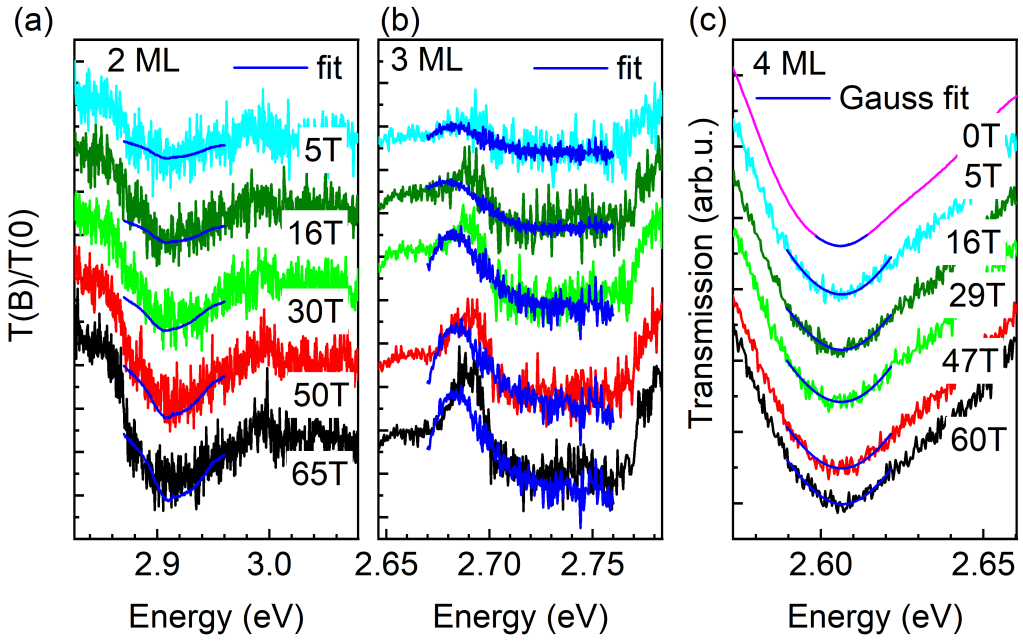

Figure 3.7: The ratio spectra of (a) 2 ML and (b) 3ML samples obtained by dividing the high field by the zero field transmission spectra using equation 3.9, together with the calculated fits (blue curves). (c) Transmission spectra of 4 ML nanoplatelets at selected magnetic fields together with the Gaussian fits (blue curves).

In the case of 4 ML thick nanoplatelets, the magnetic field induced shift can be accurately determined by a Gaussian fitting of the transmission spectrum, as

shown in Fig.3.7 (c). Blue curves represent Gaussian fits, which agree well with the transmission spectra in the selected range.

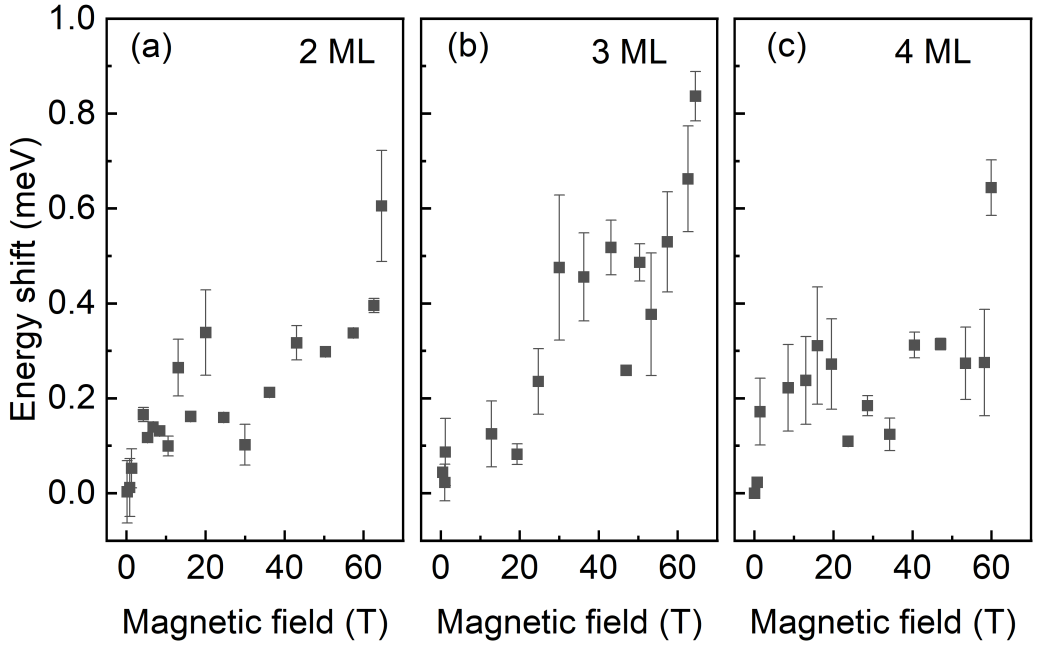

Figure 3.8: Extracted energy shift of bright exciton state as a function of the magnetic field. The data of (a) 2 ML and (b) 3 ML nanoplatelets are obtained by fitting the ratio spectra in Fig.3.7 (a) and (b) respectively using equation 3.9, and the data of (c) 4ML are obtained from Gaussian fits.

Finally, by fitting the ratio transmission spectra $T(B)/T(0)$ of 2 ML and 3 ML samples using equation 3.9, as well as applying Gaussian fits to the transmission spectra of 4 ML sample, we are able to extract the magnetic field dependent energy shifts of bright excitons, as shown in Fig.3.8 (a-c), with sample thickness from 2 ML to 4 ML, respectively. Overall, each of the samples shows blue-shift of the transition energy with increasing magnetic field.

3.2.3 Magneto-photoluminescence spectra

To further explore the exciton fine structure, we perform magneto-PL measurements on $CsPbBr_3$ based nanoplatelets with octahedra thickness varying from 2 ML to 4 ML. We start from the light polarization longitudinal to magnetic field ($\mathbf{E} \parallel \mathbf{B}$). In Fig.3.9, we show the global evolution of the PL spectrum as a function of the applied in-plane magnetic field. For 2 ML magneto-PL spectra in Fig.3.9 (a), the bright exciton emission (BX), with a distinct spectral shoulder around 2.9 eV at zero-field. The BX emission weakens with increasing magnetic field before disappearing at intermediate magnetic field around 30 T, as the inset shown in Fig.3.9 (a). Simultaneously, the peak at lower energy energies significantly increases in amplitude, and completely dominates the PL emission at high magnetic fields

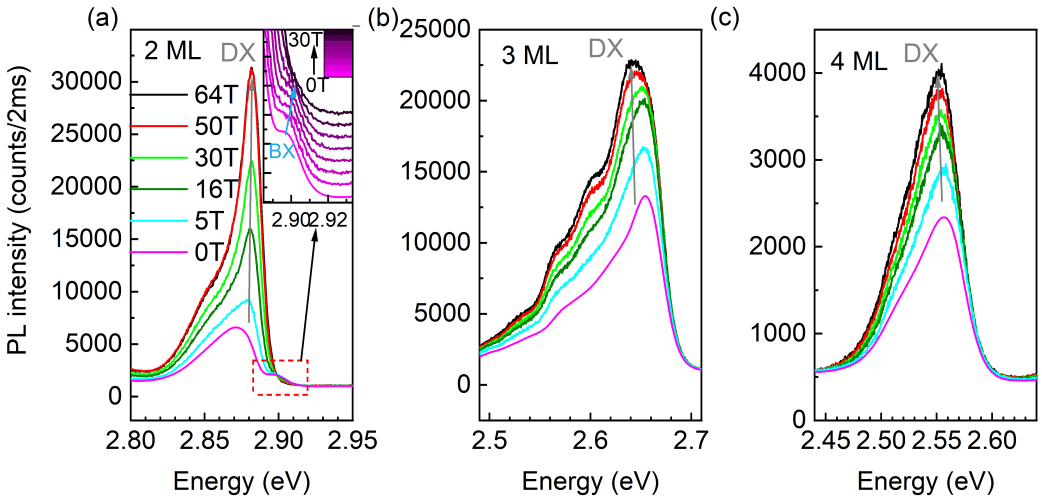

Figure 3.9: Magneto-PL spectra in the Voigt configuration of (a) 2 ML, (b) 3 ML and (c) 4 ML nanoplatelets, measured in longitudinal polarization ($\mathbf{B} \parallel \mathbf{E}$) up to 64 T at $T = 2$ K. The peaks attributed to the bright exciton and dark exciton are marked by BX and DX, respectively. The arrows are drawn as a guide to the eye. Inset of panel (a) is the bright exciton emission at selected magnetic fields up to 30 T.

up to 64 T. According to equation 3.2a, the magnetic field transfers the oscillator strength from the in-plane bright states to the dark state. Therefore, the peak with energy around 2.88 eV at 64 T is attributed to the dark exciton emission (DX). For 3 ML nanoplatelets, overall, the PL intensity of the main peak with energy around 2.66 eV sharply increases with increasing magnetic field, as shown in Fig.3.9 (b). Additionally, an extra shoulder at $\simeq 2.64\,eV$ is observed on the PL spectrum at 64 T, which might also be attributed to the brightened dark exciton emission. Fig.3.9 (c) shows the magneto-PL spectra of 4 ML sample. We can clearly see that the energy of the main peak slightly red shifts (as expected for dark exciton emission) and the PL intensity dramatically increases with increasing magnetic field.

To precisely determine the energy and intensity values of different peaks, we apply multiple Gaussian fits to these PL spectra. To simplify, we normalize the amplitude of all of PL spectra to the zero PL spectrum (PL spectra divided by the intensity of the main peak in the zero-field spectrum). In Fig.3.10, we show selected PL spectra of (a) 2 ML, (b) 3 ML and (c) 4 ML nanoplatelets, resolved in the longitudinal linear polarization ($\mathbf{E} \parallel \mathbf{B}$), at three selected values of magnetic field, together with the different peaks used to fit the data and extract the energies and intensities. We begin the analysis of the magneto-PL spectrum by the PL spectra measured at high magnetic field, where the contribution of the dark exciton is very pronounced. To fit the data in Fig.3.10 (a) top panel, at 60 T, in addition to the dominant peak of the dark exciton emission (shaded curve), we have to add additional transitions with maxima at $\simeq$2.86 eV and $\simeq$2.875 eV (red and orange

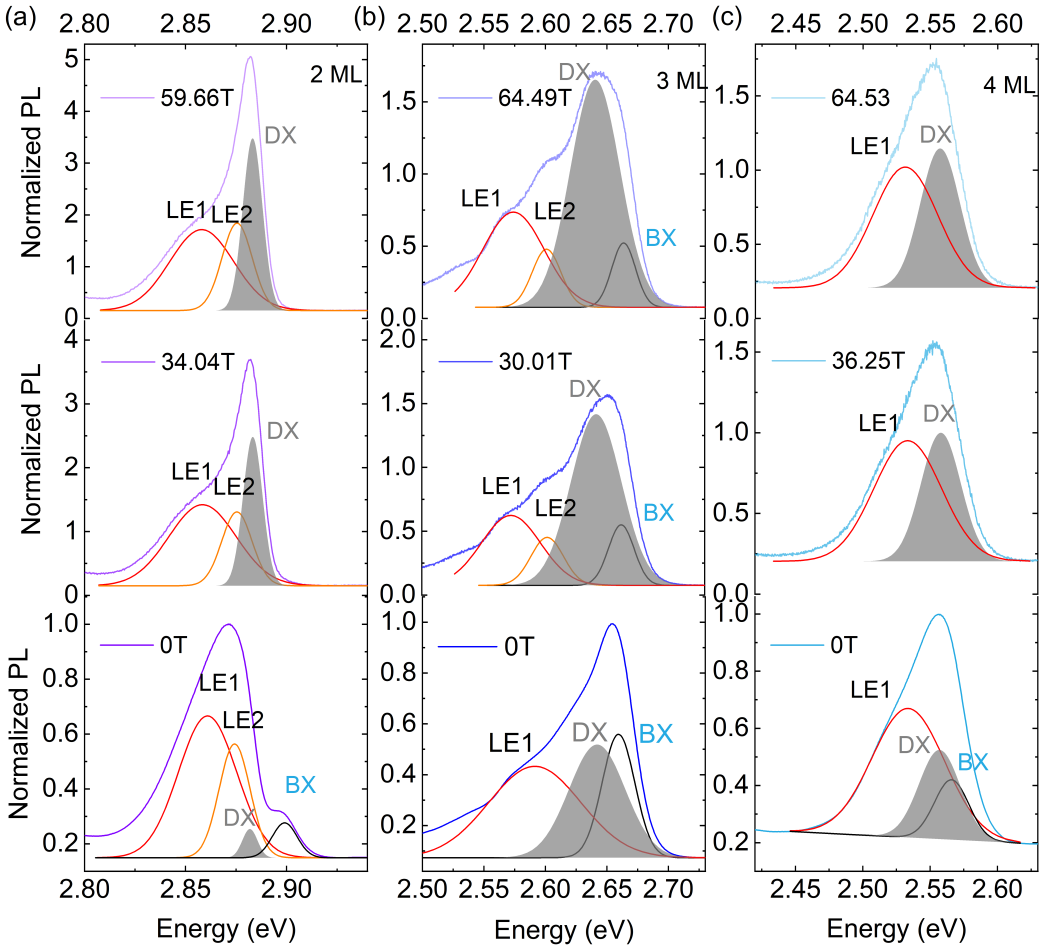

Figure 3.10: PL spectra ($\mathbf{E} \parallel \mathbf{B}$) at $\simeq 60$ T, $\simeq 30$ T and 0 T of (a) 2 ML, (b) 3 ML and (c) 4 ML thick nanoplatelets. Multiple Gaussian fits are also shown. The bright state is shown with a black curve marked as BX, the expected dark state is represented by a dark, shaded curve, marked as DX. Additional peaks at low energy side are shown in red and orange, marked as LE1 and LE2, respectively.

curves, marked as LE1 and LE2, respectively) to fully describe this spectrum. We fit the magneto-PL spectra by triple Gaussian fits until intermediate magnetic field at $\simeq$30 T, where the energy of the DX peak can still be determined with sufficiently high accuracy (see Fig.3.10 (a) middle panel).

However, for magnetic fields below $\simeq$30 T the fitting procedure becomes more difficult, and increasingly artificial due to the weaker and weaker emission from the dark exciton and more distinct bright exciton emission on the higher energy side. In this case, we are not able to precisely extract the energy and intensity values of the DX peak from the triple Gaussian fits. To obtain the PL intensity values of both bright and dark states emission at low magnetic field, we fix the energy value of DX peak, which is extrapolated to zero-field by simultaneously fitting the bright branch from magneto-transmission results, and dark branch from magneto-PL results at

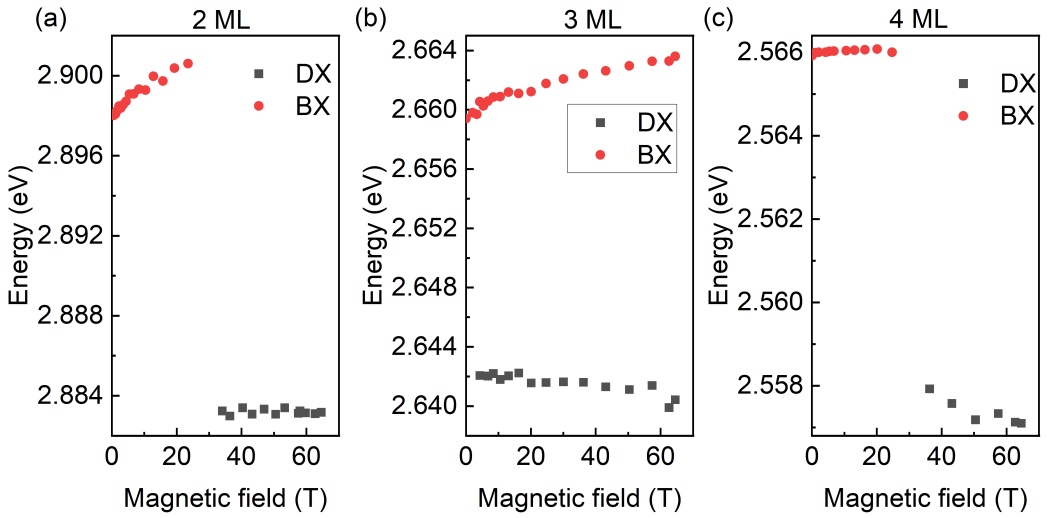

Figure 3.11: Magnetic field dependence of energies of the expected dark (DX) and bright (BX) transitions, which are obtained from the magneto-PL spectra ($\mathbf{E} \parallel \mathbf{B}$) of (a) 2 ML, (b) 3 ML and (c) 4 ML thick nanoplatelets by multiple Gaussian fits in Fig.3.10.

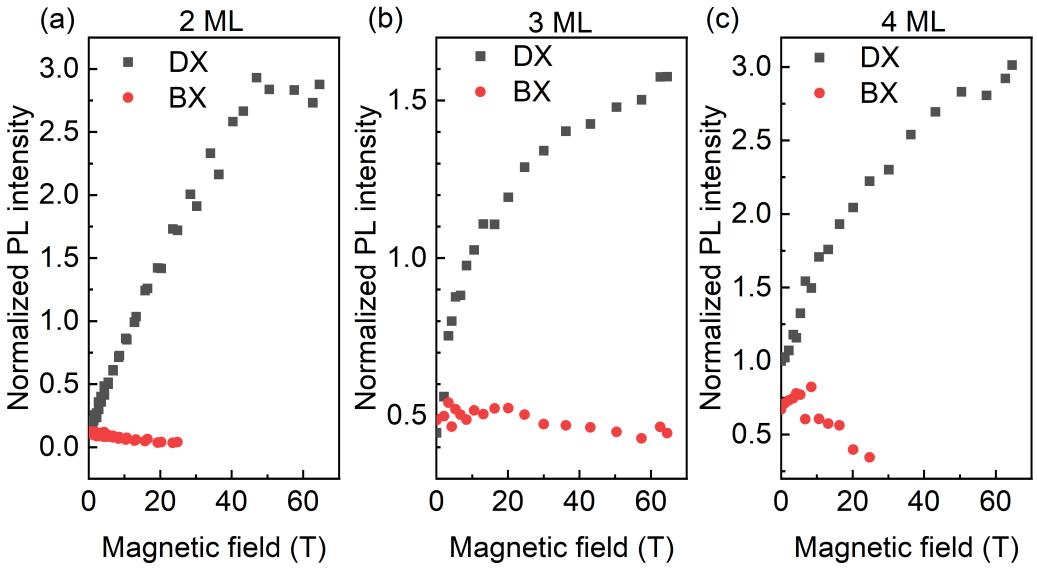

Figure 3.12: Magnetic field dependence of PL intensities of the expected dark (DX) and bright (BX) transitions, which are obtained from the magneto-PL spectra ($\mathbf{E} \parallel \mathbf{B}$) of (a) 2 ML, (b) 3 ML and (c) 4 ML thick nanoplatelets by multiple Gaussian fits in Fig.3.10.

high magnetic field by means of equation 3.4a, as the next section 3.3.1 as shown in Fig. 3.19 (a). More details about how to extrapolate the dark exciton energy to zero-field will be introduced and described in the next section 3.3.1, here we

just show our fitting method on PL spectra at low magnetic fields. In Fig.3.10 (a) bottom panel, we show PL spectrum of 2 ML nanoplatelets at zero-field as well as the fitting results. Since the DX energy value is a known parameter, we fix this energy, which for 2 ML sample at zero-field is 2.882 eV, then we use quadruple Gaussian fits to fit this spectrum. By fixing each value of DX energy at the selected magnetic field, we can determine the energy and intensity values of the BX peak, LE1 peak and LE2 peak, as well as the intensities of the DX peak at lower magnetic fields. In the cases of 3 ML and 4 ML nanoplatelets, we use the same method, as shown in Fig.3.10 (b) and (c), respectively. We start fitting from a high magnetic field to a critical magnetic field (for 3 ML is $\simeq$4 T and 4 ML is $\simeq$30 T), where the energy of the DX peak can no longer be accurately determined. Then we use extrapolated values of the DX peak below the critical magnetic field from the next section 3.3.1, Fig. 3.19 (b) and (c), respectively.

In Fig.3.11, we plot the energies of the DX and BX peaks obtained from multiple Gaussian fits as a function of the magnetic field. For 2 ML, 3 ML and 4 ML samples, the BX peak blue shifts with increasing magnetic field, as shown by the red circles in Fig.3.11 (a), (b) and (c), respectively, whereas the DX peak slightly red shifts with increasing magnetic field (black rectangles). In Fig.3.12, we also plot PL intensities of DX and BX peaks as a function of the magnetic field. For 2 ML, 3 ML and 4 ML samples, the PL intensity of BX peak decreases with increasing magnetic field, as shown by the red circles in Fig.3.12 (a), (b) and (c), respectively, whereas the PL intensity of DX peak rapidly increases with increasing magnetic field (black rectangles).

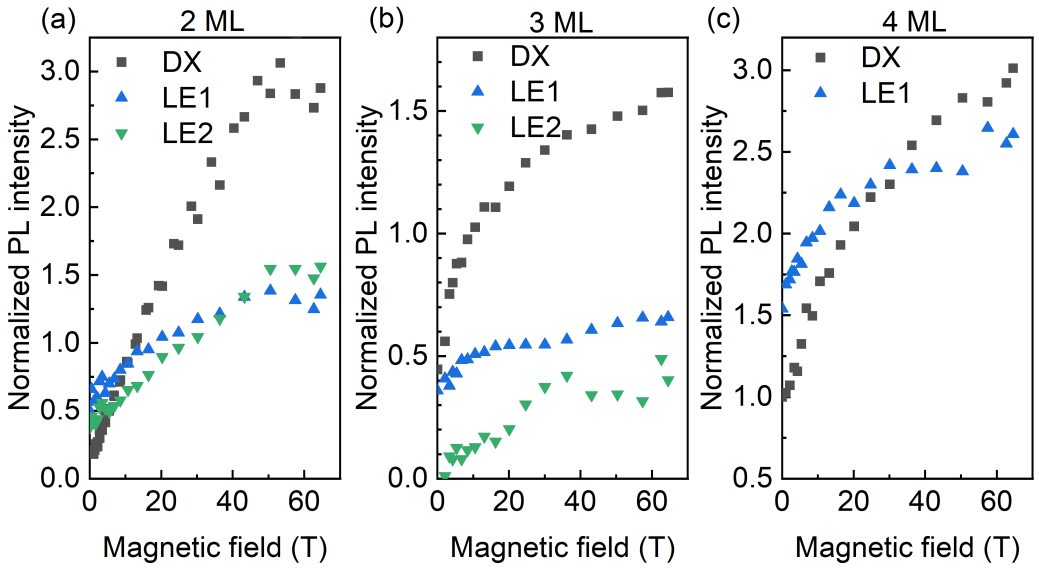

Figure 3.13: Magnetic field dependence of PL intensities of the dark and additional transitions at low energy side (LE1 and LE2), which are obtained from the magneto-PL spectra of (a) 2 ML, (b) 3 ML and (c) 4 ML thick nanoplatelets by multiple Gaussian fits in Fig.3.10.

It is important to note that, our results suggest that the dark state, which in principle is an optically forbidden state in the absence of magnetic field, nevertheless gives rise to PL emission even at zero-field. This is consistent with prior reports on nanoplatelets [Rossi 2020, Gramlich 2022b] and Ruddlesden-Popper perovskites [Ema 2006, Tanaka 2005, Wang 2021, Choi 2021], and is probably related to a mixing of the dark and bright states due to spin-orbit interaction [Tanaka 2005, Goto 1990, Goto 2006, Wang 2021], crystal distortions [Ema 2006, Choi 2021, Dyksik 2021a] or phonon-assisted transitions [Dyksik 2021a, Ema 2006]. The dark emission is further brightened by the much higher occupation probability at low temperatures of the lower energy dark state compared to bright state. Additionally, the dark exciton is only partially responsible for the low energy PL spectrum at zero magnetic field. We observe two additional peaks on the lower energy side of the PL spectra of 2 ML and 3 ML sample, and one additional peak at lower energy side of PL spectra of 4 ML sample (see Fig.3.10). However, the emission intensity of these peaks are only weakly dependent on the magnetic field strength, as shown by the green and blue triangles in Fig.3.13. This suggests that these are related to the random potential landscape, due to the presence of unsaturated bonds at the boundary between the inorganic slabs and the ligands or at lattice defects, which can localize dark [Goto 2006] or bright [Choi 2021] excitons. These results suggest that the PL spectrum of $CsPbBr_3$-based nanoplatelets is richer than initially thought, with features attributed to bright, dark and localized excitonic transitions.

After describing and discussing our magneto-PL spectra of 2 ML, 3 ML and 4 ML thick nanoplatelets in the longitudinal polarization ($\mathbf{E} \parallel \mathbf{B}$), we now move to the magneto-PL spectra of these samples resolved in the transversal polarization ($\mathbf{E} \perp \mathbf{B}$). We start from an overall PL spectra of each samples at selected magnetic fields, then we analyse and discuss our experimental results.

In Fig.3.14, we show the global evolution of the PL spectrum of each samples as a function of the applied in-plane magnetic field with the light polarization transversal to magnetic field ($\mathbf{E} \perp \mathbf{B}$). For 2 ML nanoplatelets, perhaps surprisingly, we find that with increasing magnetic field, the PL spectra at $\mathbf{E} \perp \mathbf{B}$ condition reveal similar trends as the PL spectra at $\mathbf{E} \parallel \mathbf{B}$ condition, as panel (a) and inset shown. The high energy shoulder with energy around 2.9 eV is attributed to the bright exciton emission (marked as BX in inset) and the lower PL peak with an energy around 2.88 eV is expected to be the dark exciton emission (marked as DX). For the magneto-PL spectra of 3 ML sample, we observe a similar line shape for each spectrum and an overall intensity decrease with increasing magnetic field, as shown in Fig.3.14 (b). In Fig.3.14 (c), we show the magneto-PL spectra of 4 ML nanoplatelets, both the line shapes of the PL spectra and the PL intensity do not change significantly with increasing magnetic field.

To fully understand the magneto-PL spectra in the transversal polarization ($\mathbf{E} \perp \mathbf{B}$), we use multiple Gaussian fits on these spectra. In Fig.3.15 (a-c), we show the magneto-PL spectra of 2, 3 and 4 ML thick nanoplatelets at $\simeq 64$ T and $\simeq 30$ T, respectively. Since these spectra are quite similar to the spectra measured in the

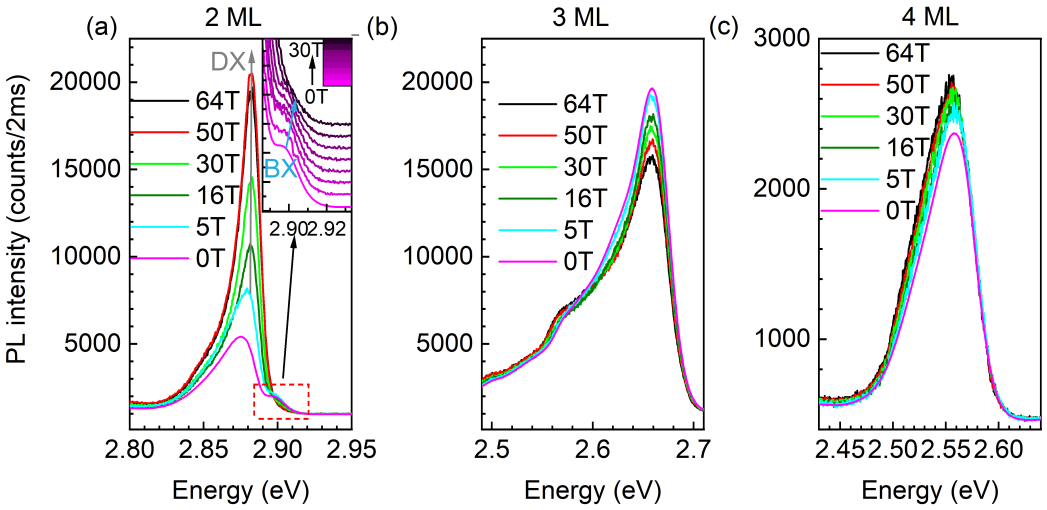

Figure 3.14: Magneto-PL spectra in the Voigt configuration of (a) 2 ML, (b) 3 ML and (c) 4 ML nanoplatelets, measured in transversal polarization ($\mathbf{B} \perp \mathbf{E}$) up to 64 T at $T = 2$ K. The peaks attributed to the bright exciton and dark exciton in panel (a) are marked by BX and DX, respectively. The arrows are drawn as a guide to the eye. Inset of panel (a) is the bright exciton emission at selected magnetic fields up to 30 T.

longitudinal polarization ($\mathbf{E} \parallel \mathbf{B}$, see Fig.3.10), we will not describe all the details of the fitting procedures, but rather focus on the fitting results of 2 ML to 4 ML nanoplatelets.

We plot the fitted energies and intensities of these peaks as a function of the magnetic field in Fig.3.16 and Fig.3.17, respectively. In the case of the 2 ML thick nanoplatelets, to better understand the results from the transversal polarization, we also show energy and PL intensity results obtained from longitudinal polarization in Fig.3.16 (a) and Fig.3.17 (a). We can see that, the DX energy in the transversal polarization red shifts with increasing magnetic field, and the energy value at each magnetic field is almost equal to the value obtained from the longitudinal polarization, whereas the BX energy blue shifts with increasing magnetic field, and the values correspond well to the energy values obtained from the longitudinal polarization as shown in Fig.3.16 (a). This result indicates the same exciton recombination channels between the transversal and longitudinal polarization. The BX PL intensity, from both polarization, equally decreases with increasing magnetic field, as green and blue rectangles shown in Fig.3.17 (a). The DX intensity, as black and red circles shown, increases with increasing magnetic field. However, intensities obtained from the transversal polarization at high magnetic fields are much lower than the intensities from the longitudinal polarization.

To understand the dark exciton behaviours in the transversal polarization, we now have to discuss the nanoplatelet orientation on the substrate. During the drop-casting process, no specific effort was undertaken to force the orientation of

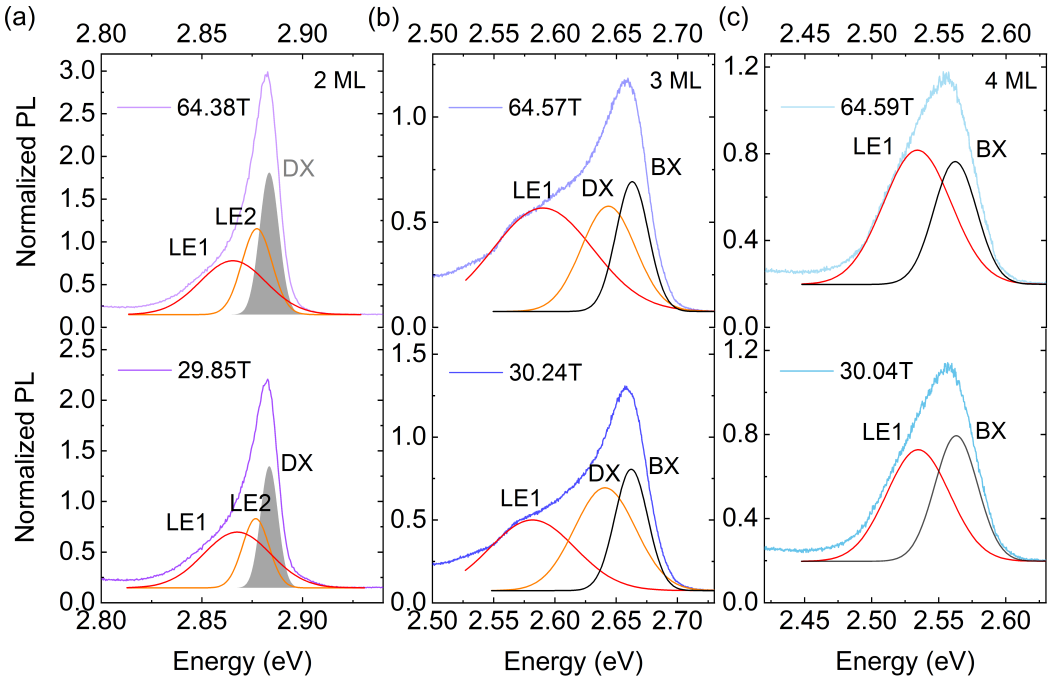

Figure 3.15: PL spectra ($\mathbf{E} \perp \mathbf{B}$) at $\simeq$30 T and $\simeq$ 64 T of (a) 2 ML, (b) 3 ML and (c) 4 ML thick nanoplatelets. Multiple Gaussian fits are also shown. The bright exciton state (BX) is shown with a black curve. Additional peaks are shown in red and orange.

the nanoplatelets in a specific direction. Most of the nanoplatelets lie parallel to the substrate, and these nanocrystals are indeed oriented with the magnetic field perpendicular to the c axis, and thus in the Voigt geometry. However, the nanoplatelets which are oriented edge-on, as in Fig3.18, will have a random direction with respect to the applied magnetic field. For these nanoplatelets, the magnetic field B can be decomposed in an in-plane component $B_{\mathrm{V}} = B \sin\theta$ and in an out-of-plane component $B_{\mathrm{F}} = B \cos\theta$, where θ is the angle between the **c** axis of the nanoplatelet and the magnetic field vector. These magnetic field components will act as if the nanoplatelet was purely in a Voigt (Faraday) configuration, with an effective magnetic field of B_{V} (B_{F}) [Bayer 2000].

In our experimental setup, we use a linear polarizer mounted parallel ($\mathbf{E} \parallel \mathbf{B}$) or perpendicular ($\mathbf{E} \perp \mathbf{B}$) to the magnetic field vector to facilitate the identification of spectral features. In the former configuration, most of the nanoplatelets which lie flat on the substrate, the transmitted light corresponds to the longitudinal exciton state. For the edge-on nanoplatelets, the signal transmitted by the polarizer mainly originates from nanoplatelets with the **c** axis close to parallel to the magnetic field vector (close to Faraday configuration, $\theta \approx 0°$, with the dipole moment of the out-of-plane exciton parallel to the direction of the polarizer, see Fig3.18 right side nanoplatelet shown). In this case, the dark exciton ϕ_{D} will couple with the out-of-

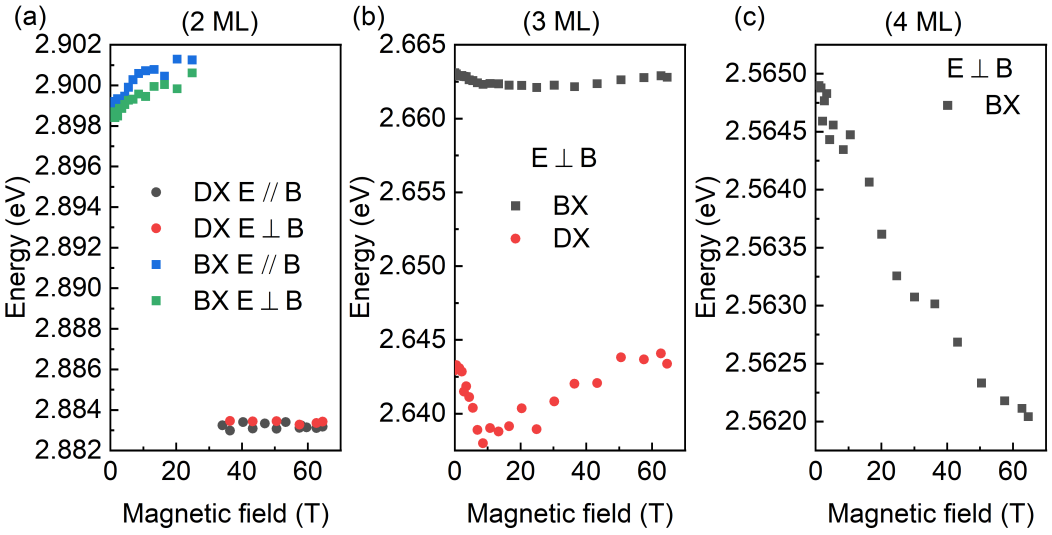

Figure 3.16: Magnetic field dependence of energies of the expected dark (DX) and bright (BX) transitions, which are obtained from the magneto-PL spectra ($\mathbf{E} \perp \mathbf{B}$) of (a) 2 ML, (b) 3 ML and (c) 4 ML thick nanoplatelets by multiple Gaussian fits in Fig.3.15. In panel (a), energies of DX and BX peaks from longitudinal polarization ($\mathbf{E} \parallel \mathbf{B}$) are also shown for comparison.

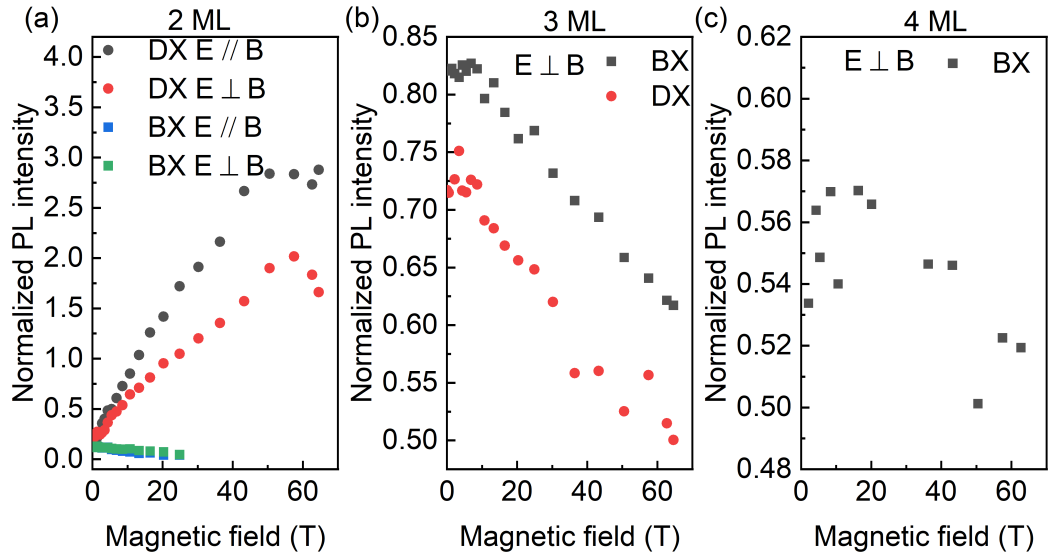

Figure 3.17: Magnetic field dependence of PL intensities of the expected dark (DX) and bright (BX) transitions, which are obtained from the magneto-PL spectra ($\mathbf{E} \perp \mathbf{B}$) of (a) 2 ML, (b) 3 ML and (c) 4 ML thick nanoplatelets by multiple Gaussian fits in Fig.3.15. In panel (a), PL intensities of DX and BX peaks from longitudinal polarization ($\mathbf{E} \parallel \mathbf{B}$) are also shown for comparison.

plane state ϕ_Z. The energy of the magnetic-field brightened dark exciton is,

$$E = \frac{1}{2}\left[E_Z + E_{\mathrm{D}} - \sqrt{(E_Z - E_{\mathrm{D}})^2 + (g_{\mathrm{D}}\mu_{\mathrm{B}}B)^2}\right], \tag{3.10}$$

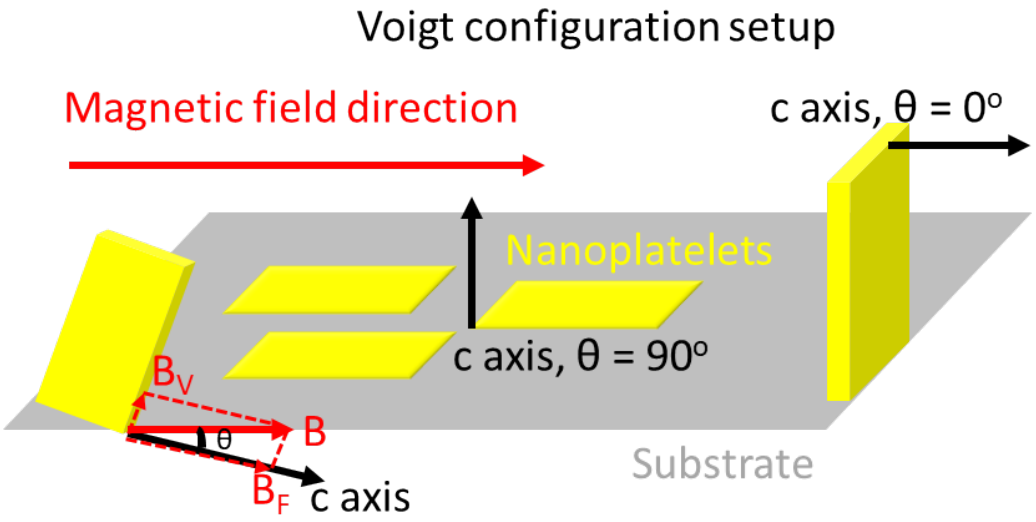

Figure 3.18: Schematics of the nanoplatelet orientation on the substrate. θ represents the angle between the **c** axis of the nanoplatelet and the magnetic field vector.

where E_Z and E_D are the zero-field energies of the out-of-plane exciton and dark exciton, g_D is the g-factor of the dark exciton in the Faraday configuration, and μ_B is the Bohr magneton [Kataoka 1993]. This expression is very similar to equation 3.4a, and the shift rate of the dark exciton is expected to be very similar to that of the dark exciton in the Voigt configuration. The nanoplatelets at intermediate angles (see Fig3.18 left side nanoplatelet shown) will be subjected to an effectively smaller in-plane magnetic field, and exhibit a smaller energy shift of the dark exciton, which might result in a slight asymmetry of the peak related to the dark exciton on the high energy side. However, they can be optically active in the transversal polarization.

In the cases of 3 ML and 4 ML samples, we observe a global red shift of the BX energy with increasing magnetic field, as shown by the black rectangles in Fig.3.16 (b) and (c), respectively. This reflects the negative branch of the transversal exciton states, as equation 3.4b predicts, where excitons relax before recombining radiatively. We also observe a decreased intensity with increasing magnetic field, as shown by the black rectangles in Fig.3.17 (b) and (c). Combining with the eigenstate of the transversal dipole (equation 3.2b), this observation can be explained by the mixing of the out-of-plane bright exciton state with the in-plane bright exciton states, in the hypothesis that the out-of-plane state resides at higher energy for 3 ML and 4 ML nanoplatelets [Kataoka 1993]. In Fig3.16 (b) and Fig.3.17 (b), we also plot the magnetic field dependence of the peak attributed to the dark exciton of the 3 ML thick nanoplatelets (see Fig3.15 (b) DX peak) as a function of the magnetic field in the transversal polarization ($\mathbf{E} \perp \mathbf{B}$). According to the selection rules (see Fig.3.1), the dark state should not couple to the transversal polarization.

The PL of nominally dipole forbidden excitons have been investigated in the Voigt configuration, where transitions forbidden by selection rules have been observed [Ema 2006], due to relaxed selection rules in the presence of crystal distortions [Ema 2006, Choi 2021, Dyksik 2021a] or phonon-assisted transitions [Dyksik 2021a, Ema 2006]. In the transversal polarization, the DX peak at $\simeq 2.64\,\text{eV}$ displays an overall energy blue shift and intensity decrease with increasing magnetic field, as shown by the red circles in Fig3.16 (b) and Fig.3.17 (b), respectively. This behaviour resembles the expected behaviour of the out-of-plane bright state in the transversal polarization. This possibly suggests that the mixing with this state might be one of the mechanisms responsible for the observation of the PL of the dark state even at zero magnetic field [Choi 2021].

3.3 Results and discussion

3.3.1 Dark-bright exciton splitting

The magnetic field dependence of the energy of the bright and dark states, obtained by fitting the magneto-transmission spectra in the longitudinal polarization (see Fig.3.8) and the magneto-PL spectra (see Fig.3.11 (a)), is shown in Fig.3.19 (a-c). The predicted evolution using equation 3.4a reproduces well the observed blue and red-shifts and allows us to extract the zero-field dark-bright splitting. The obtained dark-bright splitting, shown in Fig.3.19 (d), increases with decreasing thickness of the inorganic slab of nanoplatelets from $\simeq 9\,\text{meV}$ for the 4 ML nanoplatelets to $\simeq 21\,\text{meV}$ for the 2 ML nanoplatelets due to the enhanced exciton confinement. The splitting of 2 ML nanoplatelets reported here is slightly smaller than those measured by using optical spectroscopy in nanoplatelets synthesized with a very similar approach [Gramlich 2022b], possibly due to a slightly larger in-plane size of the nanoplatelets investigated in our study and a concomitantly reduced in-plane confinement. However, our splitting values of 3 ML and 4 ML nanoplatelets well correspond to the experimental results reported in the reference of [Gramlich 2022b] and theoretical results reported by Maria Chamarro's group, who theoretically calculated the fine structure splitting of $CsPbBr_3$ nanoplatelets by considering short-range and long-range exchange interactions [Ghribi 2021]. Moreover, the values we presented here are considerably larger than the dark-bright splitting of conventional nanocubes [Tamarat 2019, Chen 2018], which exhibit far less confinement [Takagahara 1993].

A decrease of octahedral layer thickness in nanoplatelets results in an increase of the exciton binding energy, as shown in Fig.3.5 (b), due to the larger dielectric and quantum confinement effects in the colloidal perovskite quantum wells [Fu 1999, Ghribi 2021, Ben Aich 2020], which also lead to the increase of the dark-bright exciton splitting. In Fig.3.20, we show the obtained dark-bright splitting as a function of the exciton binding energy (taken from Fig.3.5 (b)). As expected, the dark-bright splitting systematically increases with increasing exciton binding energy.

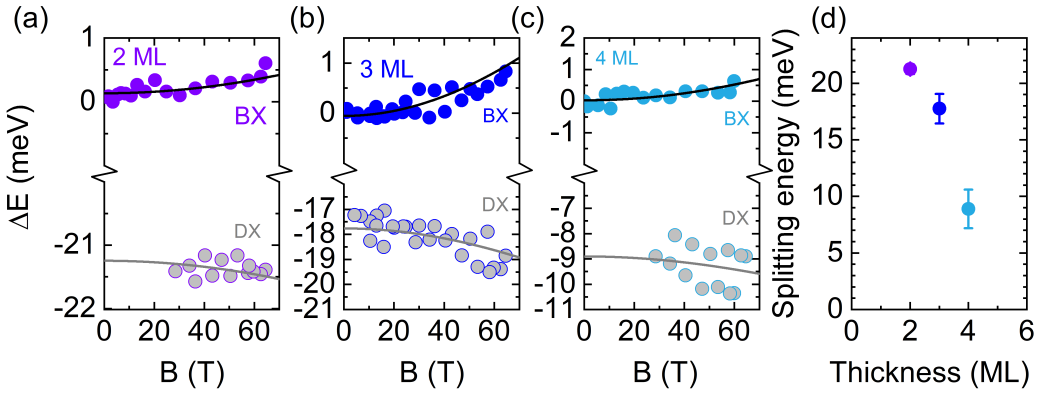

Figure 3.19: (a-c) Magnetic field dependence of the energies of the dark and bright exciton transitions relative to the zero-field transition energy of the bright state ΔE for 2-4 ML nanoplatelets. The lines are fits of the data using equation (3.4a). (d) Measured bright-dark splitting as a function of nanoplatelet thickness.

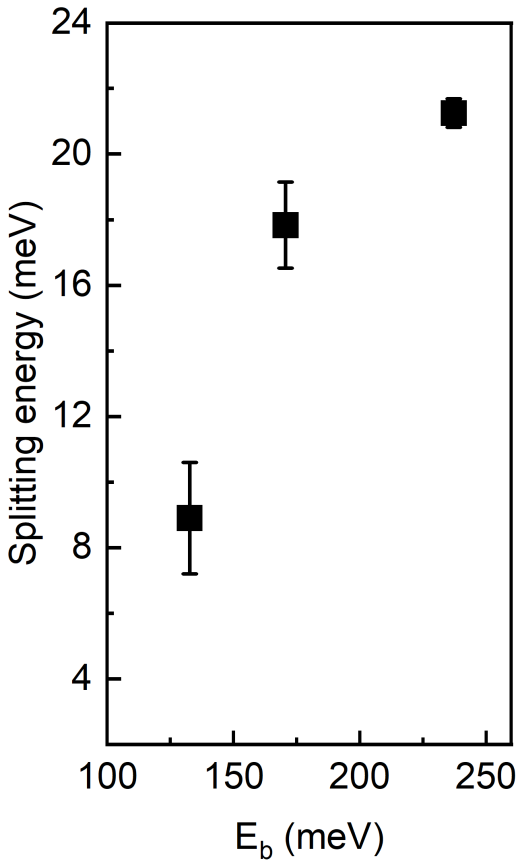

Figure 3.20: Bright-dark energy splitting at $B = 0\,\mathrm{T}$ in function of exciton binding energy E_b (E_b is taken from Fig.3.5 (b)).

3.3.2 Photoluminescence intensity and the phonon bottleneck

To corroborate our PL peak assignment, we analyze the intensities of the bright and dark exciton states, shown in Fig.3.21 (a-c). We normalize all the peaks to the intensity of the dark exciton peak at zero magnetic field. The intensity of the dark state emission increases considerably, while that of the bright states decreases slightly with increasing magnetic field. This is fully consistent with the expected transfer of oscillator strength due to the magnetic field induced bright-dark mixing in the Voigt geometry. The 2 ML thick nanoplatelets exhibit the largest increase in PL intensity. This might appear surprising at first sight, considering that equation (3.3b) predicts that a large dark-bright energy difference corresponds to a small gain in the dark exciton oscillator strength. However, the PL intensity is related to the product of the state occupation and the oscillator strength. Therefore, the significantly larger population of the dark exciton state of the thinnest nanoplatelets can account for its larger magneto-PL intensity, as we discuss below in detail.

In Fig.3.21 (d), we plot the magnetic field dependence of the ratio between the intensity of the dark states, I_{D} and the bright states, I_{B}, which we calculate as

$$\frac{I_{\mathrm{D}}(B)}{I_{\mathrm{B}}(B)} = \frac{d_1^2(B)}{d_{3\mathrm{L}}^2(B) + d_{3\mathrm{T}}^2(B)} e^{-\frac{E_1 - E_{3\mathrm{L}}}{k_B T}}, \tag{3.11}$$

where the Boltzmann factor $e^{-\frac{E_1 - E_{3\mathrm{L}}}{k_B T}}$ accounts for the population ratio between the dark and bright states [Dyksik 2021a], d_1, d_{3L} and d_{3T} are coefficients from equations 3.3b and 3.3d. For simplicity, we neglect here the presence of localized exciton states. Due to the considerably more populated dark state in the 2 ML thick nanoplatelets, the PL intensity of the dark state is stronger in thinner nanoplatelets, as shown in Fig.3.21 (d). Importantly, to reproduce the experimental data (see Fig.3.21 (d)), we had to use an effective exciton temperature of $T = 24\,\mathrm{K}$ for 2 ML, $T = 47\,\mathrm{K}$ for 3 ML and $T = 15\,\mathrm{K}$ for 4 ML according to equation 3.11, as the curves indicated in Fig.3.21 (d). These temperatures are at least an order of magnitude higher than the lattice temperature of $\simeq 2\,\mathrm{K}$ (experimental temperature). This mismatch between the lattice temperature and the effective exciton temperature suggests that the exciton population is not fully thermalized at the moment of the recombination [Dyksik 2021a].

This observation can be explained in light of the energy level structure of the exciton manifold, in combination with the peculiar relaxation processes in metal halide perovskites. Due to the greatly enhanced exchange interaction in a strongly confined system [Takagahara 1993], the splittings in the exciton manifold exceed the energies of longitudinal optical (LO) phonons, with energies from $\simeq 12$ to $15\,\mathrm{meV}$ and $\simeq 30$ to $40\,\mathrm{meV}$ [Du 2019, Gramlich 2021, Straus 2016], to which excitons can couple to efficiently dissipate excess energy. The coupling of excitons to acoustic phonons is weak in soft materials of both bulk and two-dimensional perovskites. Additionally, due to the momentum-energy conservation, the energy change in a single scattering process is in the range of $0.1\,\mathrm{meV}$ [Dyksik 2021a]. Therefore, acoustic phonons cannot efficiently scatter excitons from the bright to the dark state. For

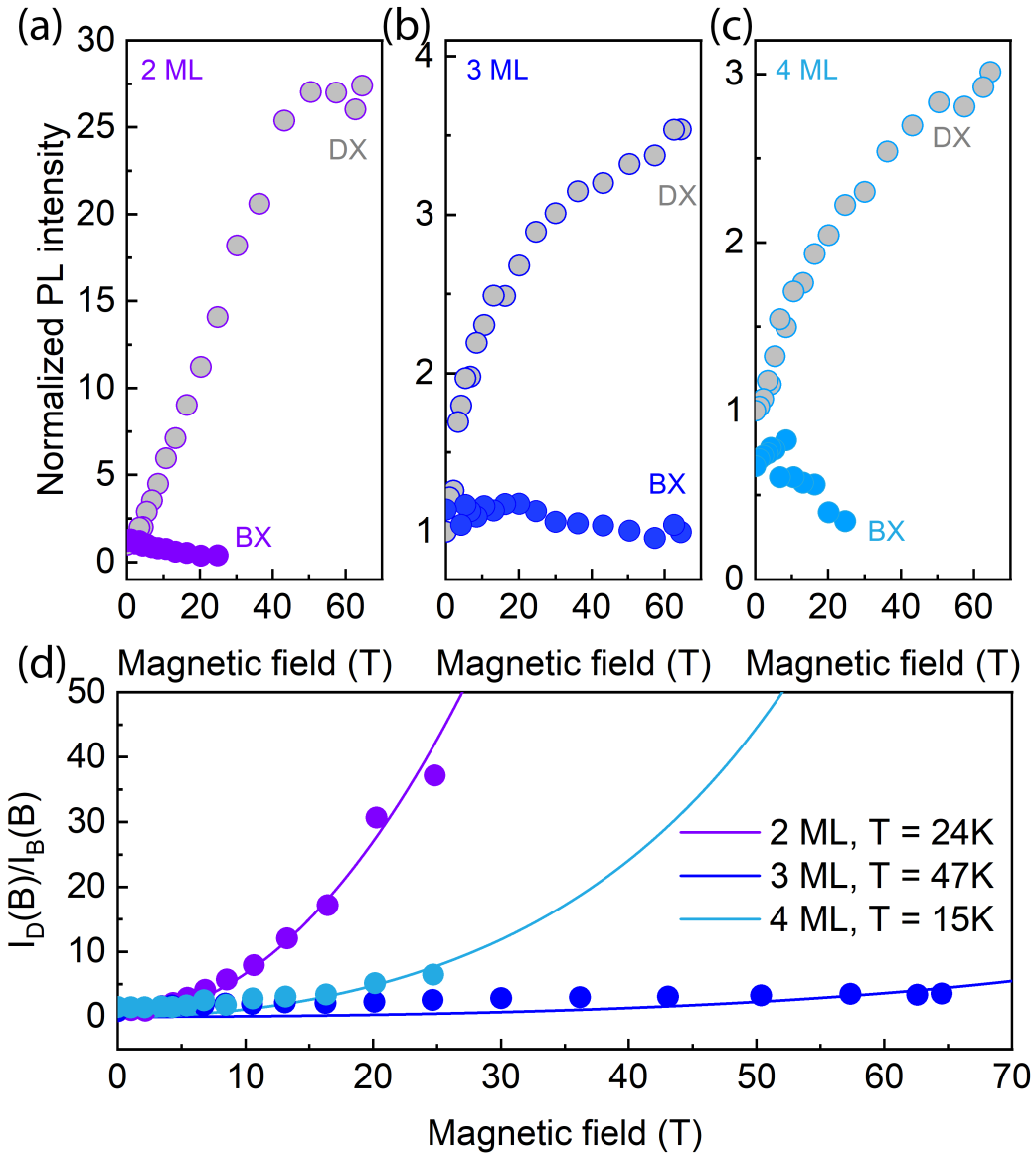

Figure 3.21: (a-c) Magnetic field dependence of the intensity of the dark and bright exciton transitions normalized to the intensity of the dark exciton transition at zero magnetic field for 2-4 ML thick nanoplatelets. (d) PL intensity ratio between dark and bright exciton states for the three nanoplatelet thicknesses investigated as a function of the applied magnetic field. Full circles represent experimental points. The curves are calculated using Eq. (3.11) and the assumed temperature is indicated in the inset.

example, in the case of the 4ML thick nanoplatelets, a more efficient exciton relaxation to the dark state might be driven by an $\simeq 9\,\text{meV}$ LO phonon [Du 2019], to which, however, carriers do not couple very efficiently [Gramlich 2021]. This energy mismatch between LO phonons and dark-bright splittings, together with

the virtually negligible coupling of carriers to acoustic phonons in metal halide perovskites [Straus 2019], leads to the highly non-thermalized exciton population visible in Fig.3.21 (d) and supports the presence of a phonon bottleneck in strongly confined perovskite nanocrystals.

3.3.3 Landé g-factor of the longitudinal states

The fitting of the data presented in Fig.3.19 (a-c) with equation 3.4a allows us not only to determine accurately the splitting between the dark and the bright states, but also the Landé g-factor of the longitudinal states g_{L} in the Voigt configuration. Here, the effective g-factor g_{L} can be estimated as

$$g_{\mathrm{L}} = g_{\mathrm{e}\perp} - g_{\mathrm{h}\perp}, \tag{3.12}$$

where $g_{\mathrm{e}\perp}$ and $g_{\mathrm{h}\perp}$ are the g-factors of the electron and of the hole in the Voigt configuration, normal to the **c** axis, respectively. The values of this quantity for all thicknesses are reported in table 3.1. These values do not differ significantly from the values of other two-dimensional perovskites compounds, such as $(PEA)_2SnI_4$ ($g_{\mathrm{L}} = 2.3$), $(PEA)_2PbBr_4$ ($g_{\mathrm{L}} = 3.2$) and $(PEA)_2PbI_4$ ($g_{\mathrm{L}} = 4.0$), reported from our group by using the same experimental method [Dyksik 2021a]. More recently, g-factors of electrons and holes in the Voigt geometry have been measured in bulk $CsPbBr_3$ by using spin-flip Raman scattering in magnetic fields up to 10 T at cryogenic temperatures [Kirstein 2022]. The g-factor can be determined from the measured Zeeman splitting E_Z by means of

$$E_Z = g\mu_B B. \tag{3.13}$$

Based on this, one can calculate the electron g-factor $g_e = 1.69$ and hole g-factor $g_h = 0.85$ of bulk $CsPbBr_3$ in Voigt configuration, leading to the effective g-factor of the exciton to be 0.84 according to equation 3.12, which is close to our experimental effective g-factors in table 3.1.

Table 3.1: Summary of measured effective g-factors for longitudinal ($g_{\mathrm{L}} = g_{\mathrm{e}\perp} - g_{\mathrm{h}\perp}$) in Voigt geometry.

Thickness	g_{L}
2ML	1.23 ± 0.17
3ML	2.31 ± 0.14
4ML	1.27 ± 0.32

3.4 Conclusion

In conclusion, we have used large in-plane magnetic fields to accurately extract the splitting between the dark and the bright exciton states of $CsPbBr_3$-based

nanoplatelets. In this configuration, the optically inactive states are brightened by the applied magnetic field and become the strongest contribution to the PL spectra, while simultaneously red shifting with increasing magnetic field. The combination of these two observations allows us not only to accurately determine the splitting between the dark and bright excitons, even when this is considerably smaller than the inhomogeneous broadening of the PL spectrum, but also to reveal the presence of additional PL bands, possibly related to the localization of excitons. The approach applied here for the first time to perovskite-based nanoplatelets, enables us to confirm that the lowest-lying exciton state is optically dark and to determine the energy spacing between optically dark and optically bright states. The measured decrease in the dark-bright splitting with increasing thickness of the nanoplatelets nicely reflects the expected increase in carrier confinement as the number of lead-halide octahedral planes is decreased. The energy splittings and magneto-PL intensities determined experimentally suggest that the dark and bright excitons are not fully thermalized with the crystal lattice. We attribute this observation to the mismatch between the large splittings within the exciton manifold and the energies of the LO phonons in metal halide perovskites. This, in combination with the poor coupling with acoustic phonons, leads to the observed non-thermalized exciton distribution, suggestive of the phonon bottleneck.

Chapter 4

Magneto-optical spectroscopy on $(PEA)_2Pb_{1-x}Mn_xI_4$ perovskites

Contents

In this chapter, we show results of magneto-optical measurements on 2D perovskite $(PEA)_2Pb_{1-x}Mn_xI_4$ (PEA is phenethylammonium, $x = 0$, 0.5%, 1%, 2% and 5%, respectively). We start with a brief introduction to dilute magnetic semiconductors (DMS). We then show our experimental results of magneto-optical spectroscopy on 2D $(PEA)_2Pb_{1-x}Mn_xI_4$ materials. By applying large out-of-plane magnetic fields (Faraday configuration) up to 65 T, we extract the Zeeman splittings. We demonstrate that the exciton g-factor increases with increasing Mn concentration up to $x = 2\%$ due to the sp-d exchange interaction between band-edge exciton and magnetic Mn ions. However, when the Mn concentration increases to 5%, the g-factor decreases and the value is comparable to the value of the 0.5% material, which is attributed to the d-d exchange interactions between Mn and Mn ions. Some of the results presented in this chapter have been published in Nature Communications, ***12****, 3489 (2021).*

4.1 Introduction

Dilute magnetic semiconductors (DMS) refer to semiconductors doped with transition metal atoms, such as chromium, manganese, iron, cobalt and nickel, *etc.* In DMS, a transition metal atom is substituted on a small fraction, x, of the host atom sites ($A_{1-x}M_xB$, where M is a transition metal). The transition metal induces magnetic properties in the non-magnetic host semiconductors AB. DMS are halfway

between non-magnetic and magnetic materials, so they are often referred to as semi-magnetic semiconductors [Munekata 1989, Shapira 1991, Cibert 2008]. Since the early 1970s, research has been focused on numerous DMS systems, including transition metal (mainly Mn) doped into II-VI semiconductors such as $Cd_{1-x}Mn_xTe$ [Gaj 1979] or $Cd_{1-x}Mn_xSe$ [Aggarwal 1983], and IV-VI semiconductors such as $Pb_{1-x}Mn_xTe$ and $Pb_{1-x}Mn_xSe$ [Bauer 1992]). Compared to II-VI semiconductors, the solubility of magnetic ions in III-V semiconductors is much lower, which leads to a poor stability of the DMS. For these reasons, for a long time, the development of DMS based on III-V semiconductors was hindered. A breakthrough was made in 1989 by Munekata *et al.* , who successfully prepared III-V-based DMS $In_{1-x}Mn_xAs$ ($x \leq 0.18$) by using molecular beam epitaxy (MBE) [Munekata 1989]. In 1996, based on the results of Munekata *et al.* , Ohno and co-workers fabricated the first Mn doped GaAs DMS $Ga_{1-x}Mn_xAs$ ($x \simeq 0.015$) using MBE. Since then, III-V based DMS have attracted wide interests, in particular researchers tried to push their Curie temperatures from low temperature [Ohno 1998, Matsukura 1998] towards room temperature, DMS also have commercial applications, for example in a metallic version of spintronics [Fert 2007, Gaj 2011]. Indeed, it is widely accepted that DMS are promising materials for spintronic semiconductor devices for information processing and communications due to their combination of both magnetic and semiconducting properties [Huang 2005, Kulkarni 2006, Anbuselvan 2021].

4.1.1 sp-d exchange interactions

In this section, we will introduce the mechanism of the sp-d exchange interactions between the band-edge exciton and the local magnetic ions in DMS. Historically, this mechanism has been elucidated by comparing magnetization and Zeeman splitting results, as well as in combination with a mean field and/or virtual crystal approximations. We will see how the sp-d exchange interactions enhances the excitonic Zeeman splitting energy in DMS. As an example we consider here $Cd_{1-x}Mn_xTe$ ($0.005 < x < 0.3$) DMS, which was firstly investigated by Gaj et al. in 1978 [Gaj 1978, Gaj 1993].

CdTe is a direct-band gap semiconductor at Γ point of the Brillouin zone. Its bulk material possesses a band gap of $\simeq 1.5\,\text{eV}$ [Fonthal 2000]. When Mn ions are doped into a diamagnetic CdTe, the magnetization of a $Cd_{1-x}Mn_xTe$ at low temperature is dominated by the alignment of the Mn ions which possess magnetic moments. Gaj *et al.* performed the magnetization measurements for $Cd_{1-x}Mn_xTe$ ($0.02 < x < 0.3$) DMS at $T = 1.5\,\text{K}$ and at magnetic fields up to $15.5\,\text{T}$, and the results are shown in Fig.4.1. At low field, the magnetization of each sample linearly increases with increasing magnetic field before saturating at higher fields. This saturation is more pronounced for samples with a lower Mn concentration (see *e.g.* the $x = 0.02$ sample). For a system of non-interacting spins (lower Mn doped samples), the magnetization can be described using a Brillouin function [Gaj 2010]

$$B_S(\xi) = \frac{2S+1}{2S}\coth\left(\frac{2S+1}{2S}\xi\right) - \frac{1}{2S}\coth\left(\frac{1}{2s}\xi\right), \tag{4.1}$$

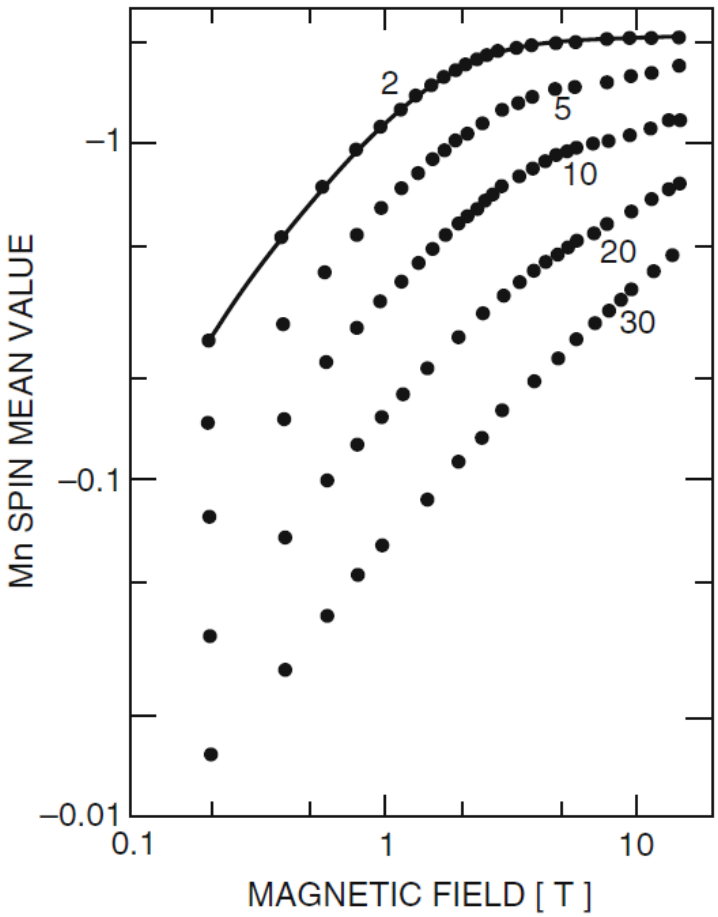

Figure 4.1: Magnetization of $Cd_{1-x}Mn_xTe$ ($0.005 < x < 0.3$) DMS. Mn concentration x values are indicated in %. Solid line represents a Brillouin function. Figure reprinted after reference [Gaj 1993].

where $S = 5/2$ is spin of the Mn. Gaj et al. proposed an empirical model which works for any Mn concentration at $T = 1.5\,\mathrm{K}$ and at magnetic fields up to $\simeq 5\,\mathrm{T}$ by introducing an spin saturation value S_0 and an effective temperature $T_{eff} = T + T_0$, where T_0 is a temperature correction. The magnetization is then described as [Gaj 1993]

$$\langle S_z \rangle = S_0 B_{5/2}\left(\frac{\frac{5}{2} g \mu_B B}{k_B T_{eff}}\right), \tag{4.2}$$

where $g = 2$ is Mn gyromagnetic factor, μ_B is the Bohr magneton and k_B is the Boltzmann constant. By adjusting the values S_0 and T_0, the magnetization data shown with different Mn concentration x in Fig.4.1 can be well fitted. For example, in the case of $x = 0.02$, the magnetization data is well described using $S_0 = 1.97$ and $T_0 = 0.94\,\mathrm{K}$ (solid line in Fig.4.1).

The s-d exchange interaction between magnetic Mn ions and electrons in the

conduction band, and the p-d exchange interaction between Mn ions and holes in the valence band (for example in $Cd_{1-x}Mn_xTe$) can be described using a Heisenberg Hamiltonian,

$$\mathcal{H} = -\sum_i \mathbf{J}(\mathbf{r} - \mathbf{R}_i)\boldsymbol{\sigma} \cdot \mathbf{S}_i, \tag{4.3}$$

where $\mathbf{r}$ and $\boldsymbol{\sigma}$ represent the position and the spin operators of a carrier, respectively. $\mathbf{R}_i$ and $\mathbf{S}_i$ represent the position and the spin operator of the $i-th$ magnetic Mn ion, respectively. $\mathbf{J}$ refers to an effective operator acting on the carrier's spatial coordinates.

In general, the concentration of photo-excited carriers is orders of magnitude lower than the concentration of Mn ions in the DMS, so the influence of carriers on the Mn ions can be neglected. In contrast, when a magnetic field is applied, the spins of Mn ions are aligned and influence the carriers by the ion-carrier interaction. In a mean field approximation, the spin operators of Mn ions are replaced by their thermal average [Gaj 1993, Gaj 2010]. Moreover, Gaj *et al.* also introduced a virtual crystal approximation to restore the crystal periodicity. The random distribution of Mn ions and cations of the host CdTe semiconductors over the cation sublattice is replaced by a periodical structure with artificial cations. The artificial cations simultaneously exhibit properties of the host CdTe cation and the incorporated Mn ions, averaged using occupation probabilities as weights. The modified Hamiltonian for the conduction band electrons is

$$\mathcal{H} = -N_0\alpha x\sigma_z\langle S_z\rangle, \tag{4.4}$$

and for the valence band holes is,

$$\mathcal{H} = -N_0\beta x\sigma_z\langle S_z\rangle, \tag{4.5}$$

where N_0 is the number of unit cells per unit volume, $\alpha = \langle \mathbf{S}\,|\mathbf{J}\,|\mathbf{S}\rangle$ is the exchange integral for the conduction electrons, $\beta = \langle \mathbf{X}\,|\mathbf{J}\,|\mathbf{X}\rangle$ is the exchange integral for the valence carriers, x is Mn concentration and $\langle S_z\rangle$ is the thermal average of zth component of Mn spin.

In $Cd_{1-x}Mn_xTe$ DMS, there are two different mechanisms of the interactions between the sp band carriers and Mn d-electrons (Mn ions have no orbital magnetic moment); (i) a Coulomb type interaction potential introduces the usual exchange mechanism, and (ii) a p-d hybridization induced strong "kinetic" mixing of the p and d-electrons. Although the former one is usually weak, it nevertheless dominates the s-d exchange integral $N_0\alpha$ in the conduction band. The latter one, kinetic exchange, is much stronger than the potential exchange and dominates the p-d exchange integral $N_0\beta$ in the valence band [Bhattacharjee 1983, Larson 1988, Hass 1988]. Combining these two mechanisms with the mean field approximation and virtual crystal approximation, Gaj et al. calculated energy states of conduction and valence electrons of $Cd_{1-x}Mn_xTe$ DMS by $k{\cdot}p$ model [Gaj 1978]. Typical band structure of $Cd_{1-x}Mn_xTe$ DMS at Γ-point of the Brillouin zone is shown in left panel of Fig.4.2.

At the external magnetic field in Faraday configuration ($\mathbf{k} \parallel \mathbf{B}$), the conduction band Γ_6 splits into two sublevels and the valence band Γ_8 splits into four sublevels.

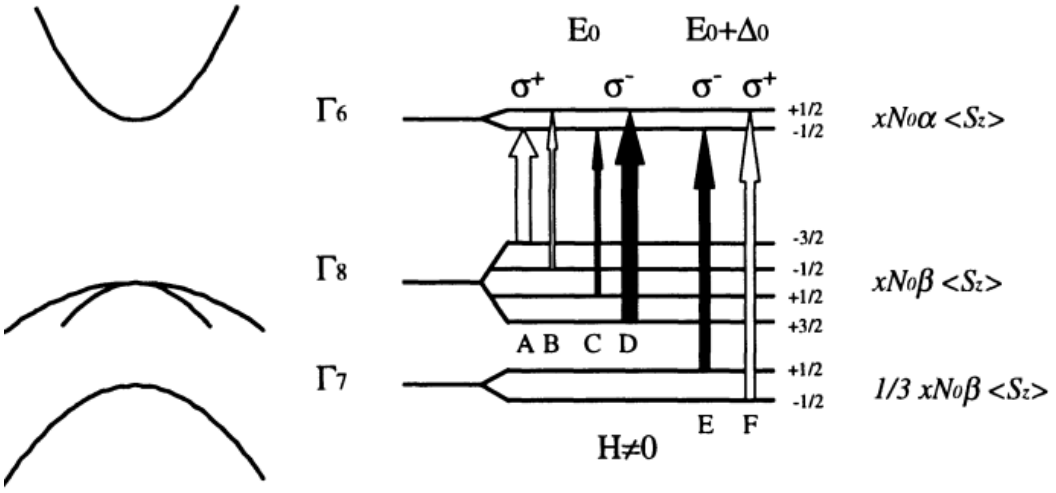

Figure 4.2: Band structure (left) and Zeeman splitting together with σ^+ and σ^- optical transitions at Γ-point of the Brillouin zone in $Cd_{1-x}Mn_xTe$ DMS. H represents the external magnetic field, E_0 is the energy transition of valence band Γ_8 to conduction band Γ_6. $\triangle_0$ represents the spin-orbit splitting energy of the Γ valence band. Figure reprinted after reference [Ando 2000].

The splitting of the conduction band and valence band can be larger because the effective magnetic field acting on the conduction and valence band carriers is amplified by magnetic moments of the Mn ions through the sp-d exchange interaction. Band-edge excitonic Zeeman splitting here refers to the energy difference between Γ_8 to Γ_6 transitions. According to the selection rules, these transitions are coupled to circularly polarized light ($\sigma^{\pm}$) [Gaj 1978, Ando 2000], as shown in Fig.4.2 right side. The transition energy E_A is

$$E_A(\sigma^+) = E_g - \frac{1}{2}x(N_0\beta - N_0\alpha)\langle S_z\rangle \tag{4.6}$$

and transition energy E_D is

$$E_D(\sigma^-) = E_g + \frac{1}{2}x(N_0\beta - N_0\alpha)\langle S_z\rangle. \tag{4.7}$$

The Zeeman splitting in the mean field approximation is described as

$$\triangle E_{ex} = E_D(\sigma^-) - E_A(\sigma^+) = N_0(\beta - \alpha)x\langle S_z\rangle \tag{4.8}$$

Therefore, band-edge excitonic Zeeman splitting in $Cd_{1-x}Mn_xTe$ DMS can be considered as the sum of the intrinsic Zeeman effect and the sp-d exchange interaction:

$$\triangle E_Z = \triangle E_{in} + \triangle E_{ex} = g_0\mu_B B + N_0(\beta - \alpha)x\langle S_z\rangle, \tag{4.9}$$

where g_0 is the exciton g-factor for Mn concentration x = 0.

In this chapter, we show results of magneto-optical spectroscopy performed on novel 2D metal halide perovskite based DMS: $(PEA)_2Pb_{1-x}Mn_xI_4$ (x = 0 ∼ 5%). We measure transmission spectra for all of these samples using high magnetic fields up to 66 T in Faraday configuration at 2.2 K. We find that by inducing a fraction of magnetic ions Mn^{2+} into pure $(PEA)_2PbI_4$, the Zeeman energy splitting of the band-edge exciton is evidently enhanced due to the sp-d exchange interaction between Mn ions and band-edge exciton. Landé g-factor is proportional to the Mn concentration up to 2%. For higher doping levels of magnetic Mn ions, such as $x = 5\%$, Mn-Mn interactions become distinct, result in smaller exciton Zeeman splitting which is comparable to the result for the 0.5% Mn doped sample.

4.2 Sample description

$(PEA)_2Pb_{1-x}Mn_xI_4$ samples were fabricated in the group of Felix Deschler in the Technical University of Munich in Germany. Pure $(PEA)_2PbI_4$ solution was synthesized by dissolving PbI_4 (LumTech, >99.999%) and phenethylammonium iodide (LumTech, >99.5%) salts in N,N-dimethylformamides (Sigma, >99.8% anhydrous) with a molar ratio of 1:2. Then the solution was stirred for 2 hours at 80 °C, filtered with a 0.2 μm pore size PTFE syringe filter.

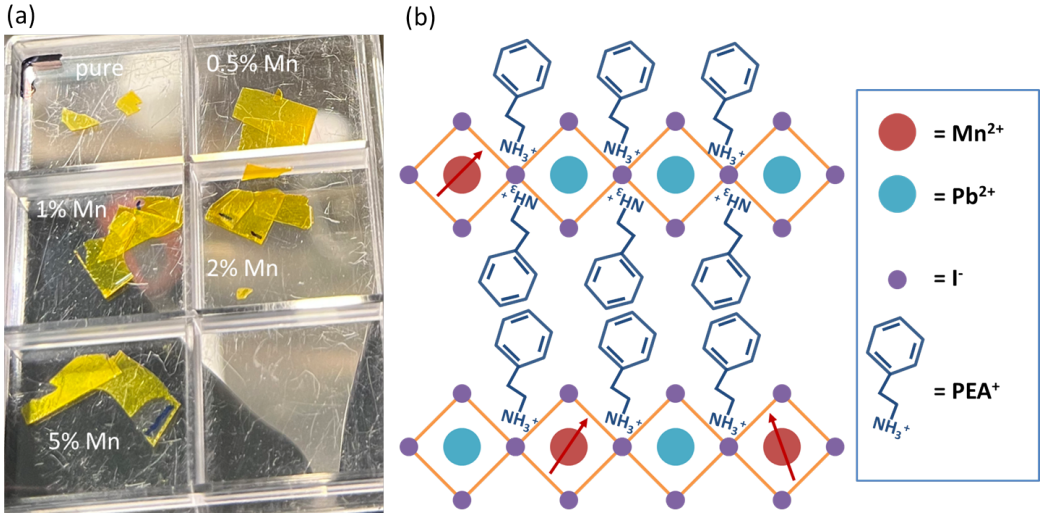

Figure 4.3: (a) Thin films of $(PEA)_2Pb_{1-x}Mn_xI_4$ for manganese concentrations $x = 0$, 0.5%, 1%, 2% and 5%. (b) Schematic crystalline structure of Mn doped layer $(PEA)_2PbI_4$ material. Mn^{2+} ions are located at the center of the octahedrals of the host $(PEA)_2PbI_4$ perovskites by substituting the divalent Pb^{2+} cations.

For Mn doped $(PEA)_2PbI_4$ solutions, all steps and conditions were as the same as for the pure sample synthesis except that the precursor PbI_4 was replaced by the mixed precursors PbI_2 and $MnBr_2$ in a proportion corresponding to the wanted atomic ratio. Thin film samples were prepared from the $(PEA)_2Pb_{1-x}Mn_xI_4$ so-

lutions. Solutions were drop-cast on oxygen-plasma-treated glass cover slips and solvents were evaporated at 120 °C for 2 hours [Neumann 2021]. Representative thin films, including a pure $(PEA)_2PbI_4$ sample, and Mn doped $(PEA)_2PbI_4$ samples with the Mn concentration x from 0.5% up to 5%, are shown in Fig.4.3 (a). They all have a characteristic bright yellow color. To better understand the structural difference between pure perovskite and Mn doped sample, in Fig.4.3 (b), we schematically show the intrinsic crystalline structure of Mn doped $(PEA)_2PbI_4$ perovskite. The magnetic impurities Mn^{2+} ions are located at the center of the octahedrals of the host $(PEA)_2PbI_4$ perovskites by substituting the divalent Pb^{2+} cations.

4.3 Magneto-optical spectroscopy of $(PEA)_2Pb_{1-x}Mn_xI_4$ perovskites

4.3.1 Optical spectra at zero magnetic field

Let us start from the optical spectra of 2D $(PEA)_2Pb_{1-x}Mn_xI_4$ samples obtained at zero magnetic field. In Fig.4.4 we show typical transmission spectra of these materials at the temperature of 4.2 K.

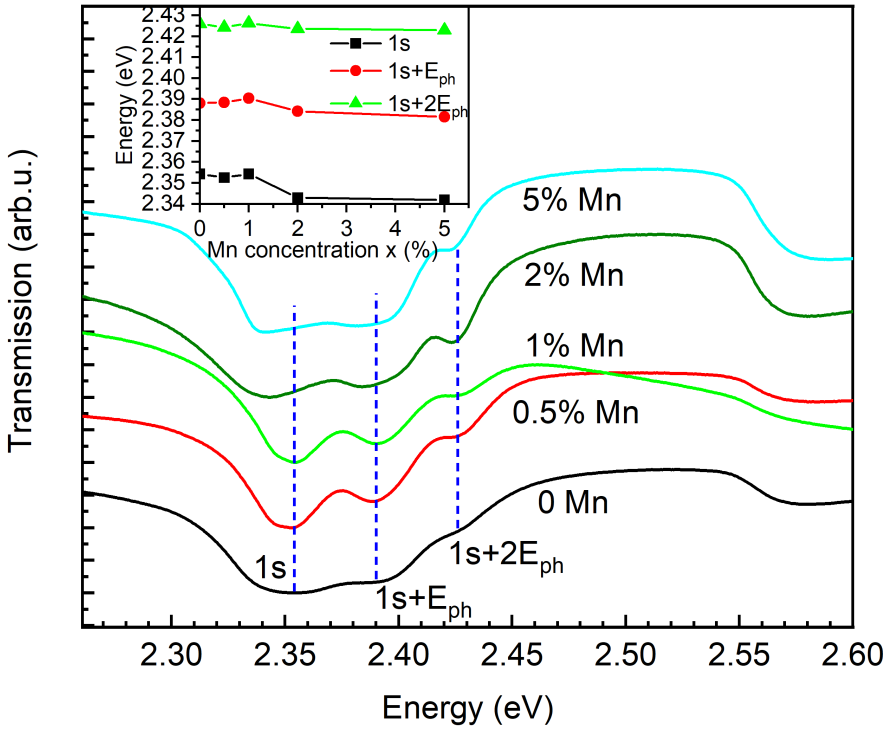

Figure 4.4: Transmission spectra of $(PEA)_2Pb_{1-x}Mn_xI_4$ at $T = 4.2$ K for manganese concentrations $x = 0$, 0.5%, 1%, 2% and 5%. Blue dashed lines are drawn as a guide to the eye. Insert: transition energies as a function of Mn concentration x.

Minimum peaks of these spectra at around 2.35 eV can be identified as the 1s exciton resonance. In Fig.4.4 insert, we show the 1s excitonic transition as well as additional transitions at high energy side as a function of Mn concentration x. The observed overall red-shift of the 1s exciton resonance with increasing Mn concentration up to 5% is accompanied by the red-shift of the equally-spaced higher energy features at $\simeq 2.39\,\text{eV}$ and $\simeq 2.42\,\text{eV}$, which are attributed to a vibronic progression of excitons coupled to a high-energy ($\simeq 37\,\text{meV}$) phonon mode of the organic spacer. This vibronic progression scenario of excitonic transitions has been proved by our group's previous magneto-absorption investigation of $(PEA)_2(CH_3NH_3)_{n-1}Pb_nI_{3n+1}$ for $n = 1, 2, 3$ where all the equally spaced ($\simeq 40\,\text{meV}$) transitions exhibit identical shifts in magnetic field for given n, as expected for phonon replicas [Urban 2020].

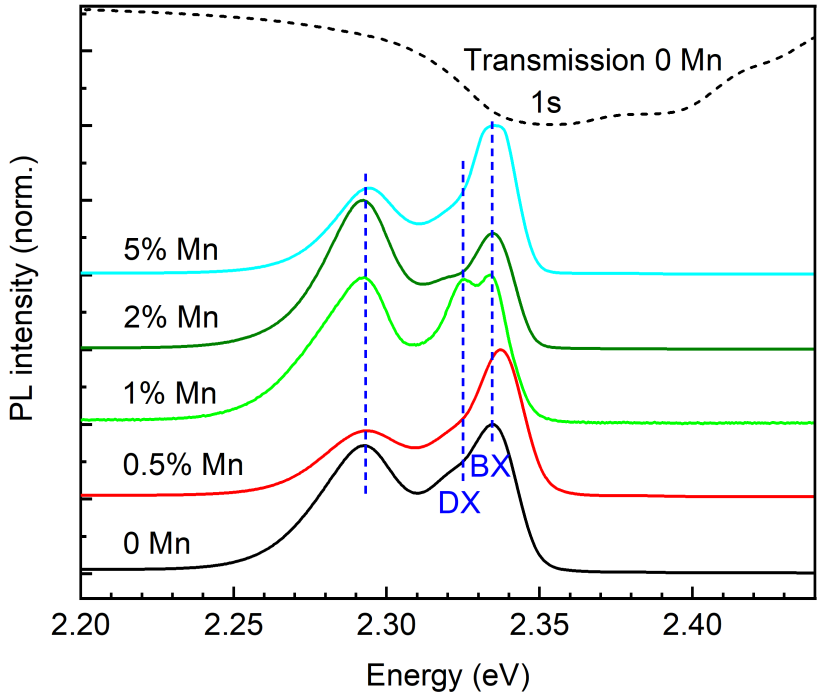

Figure 4.5: Photoluminescence spectra of $(PEA)_2Pb_{1-x}Mn_xI_4$ samples at T = 4.2 K for manganese concentrations x = 0, 0.5%, 1%, 2% and 5%. Blue dashed lines are drawn as a guide to the eyes. BX and DX represent bright exciton and dark exciton, respectively.

Our results of magneto-transmission spectra of $(PEA)_2Pb_{1-x}Mn_xI_4$ samples, which will be discussed in detail in the next section (4.3.2), also confirm the phonon replica scenario of Ref [Urban 2020]. Our group has already demonstrated that the band gap of 2D $(PEA)_2PbI_4$ is around 2.57 eV [Dyksik 2020]. In Fig.4.4, the spectral regions around 2.57 eV exhibit the same characteristic step-like features, which are related to the band-to-band absorption [Dyksik 2020, Hong 1992]. This result, combined with the similar phonon energies (see Fig.4.4 insert), indicate that

the electronic band structures of $(PEA)_2Pb_{1-x}Mn_xI_4$ materials are not significantly changed by doping with Mn impurities, even for Mn concentrations x up to 5%.

In Fig.4.5, we show PL spectra of 2D $(PEA)_2Pb_{1-x}Mn_xI_4$ samples with Mn concentrations x from 0 to 5% at a temperature of $T = 4.2\,K$. The high-energy peaks around 2.345 eV, marked as "BX", are attributed to the bright free exciton emission, since their emission energies correspond to the 1s exciton transmission energies in Fig.4.4. For comparison, we add a transmission spectrum (dashed line) of pure $(PEA)_2PbI_4$ in Fig.4.5. The PL signals around 2.335 eV, especially visible for the 1% Mn doped sample, are attributed to the dark exciton emissions, marked as DX in Fig.4.5. This is demonstrated by Neumann and co-workers magneto-PL results published in [Neumann 2021], where the DX shoulders of both Mn-doped and undoped $(PEA)_2PbI_4$ are brightened in out-of-plane magnetic fields.

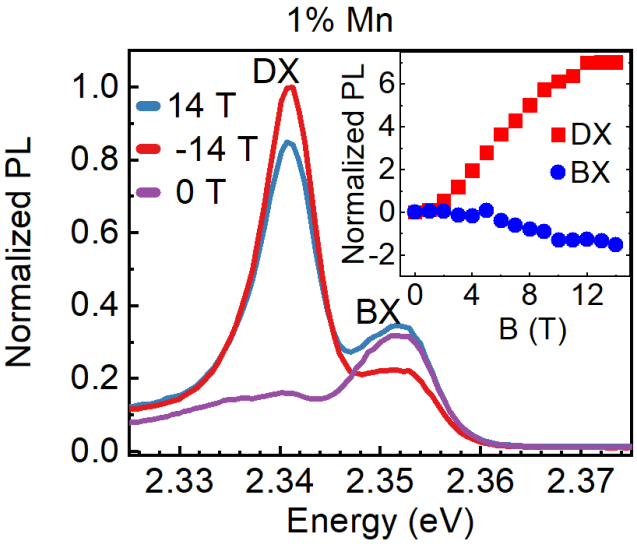

Figure 4.6: Photoluminescence spectra of $(PEA)_2Pb_{1-x}Mn_xI_4$ sample with $x = 1\%$ at 0 T and ±14 T in the Faraday configuration. Inset: PL intensity of BX and DX as a function of magnetic field. Figure reprinted after reference [Neumann 2021].

Here we take results of $(PEA)_2PbI_4$ doped with 1% Mn to illustrate this result. With increasing magnetic field, a new sharp peak appears and dominates the PL emission, as shown in Fig.4.6. The PL intensity of this peak quadratically increases with increasing magnetic field (see red rectangles in inset), which is characteristic for a dark state brightened due to mixing with the bright exciton state in the weak field limit. The dark-bright exciton splitting, if we only focus on the 1% Mn spectrum, which possesses the most distinct dark emission at zero magnetic field, is 10 meV. This value is corresponding to previous results on 2D $(PEA)_2PbI_4$ in our group, which was obtained by applying large magnetic fields to brighten the inactive dark state [Posmyk 2022, Dyksik 2021a]. The lowest energy peaks around 2.293 eV have been proposed to originate from phonon replicas [Hong 1992, Straus 2016], self-trapped excitons [Ishihara 1990] or an out-of-plane oriented magnetic dipole

transition [DeCrescent 2020].

4.3.2 Magneto-transmission spectra on $(PEA)_2Pb_{1-x}Mn_xI_4$ samples

To clarify the origin of complex excitonic features observed in transmission spectra at zero magnetic field, we measure the transmission of Mn-doped 2D $(PEA)_2PbI_4$ perovskites with Mn concentrations x from 0 to 5% at selected positive and negative magnetic fields up to 66 T in the Faraday configuration ($\mathbf{k} \parallel \mathbf{B}$). We use the experimental set-up described in Chapter 2 section 2.3. The magneto-transmission spectra are shown in Fig.4.7(a-e), respectively. The dashed lines highlight the energy shifts of the 1s excitonic transition as well as the phonon replicas, which all show the same energy shifts as the 1s transitions in magnetic field. The transitions shift to higher or lower energy depending on the direction of the magnetic field. Positive magnetic fields represent the right-handed circular polarization components (σ^+), give rise to a blue-shift of the excitonic transition energy, while negative magnetic fields represent the left-handed circular polarization components (σ^-) and result in a red-shift of the transition energy.

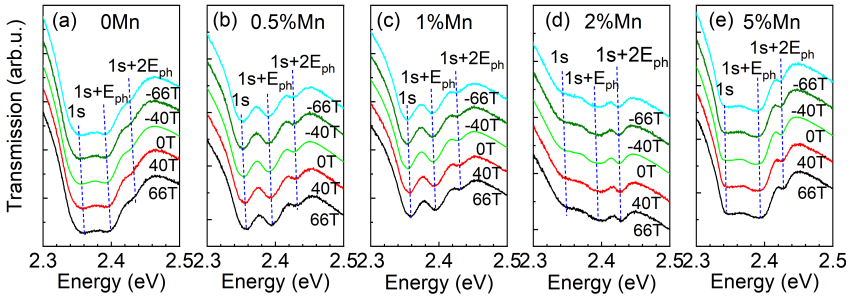

Figure 4.7: Polarization resolved transmission spectra of (a) 0, (b) 0.5%, (c) 1%, (d) 2% and (e) 5% manganese doped samples for selected magnetic fields at $T = 2.2\,\mathrm{K}$. Reversing the magnetic field direction allows us to detect in $\sigma^{\pm}$ polarization. The dashed lines highlight the shift of the 1s excitonic state as well as the phonon replicas in magnetic fields.

4.3.3 Magneto-transmission data analysis

To precisely extract the energy shift of the exciton transition as a function of magnetic field, we calculate ratio spectra, *i.e.* transmission spectra measured at different magnetic fields divided by the spectrum measured at zero field. Here we show the ratio spectra of $(PEA)_2Pb_{1-x}Mn_xI_4$ samples ($x = 0$ to 5%) in Fig.4.8 to clarify our fitting method. The ratio spectra have a characteristic sharp features with a large amplitude, and well defined line width and position, even if the magnetic field induced shift of the transition energy in regard to zero field spectrum is very small. Due to the same line shape of the raw transmission spectra at high field and zero

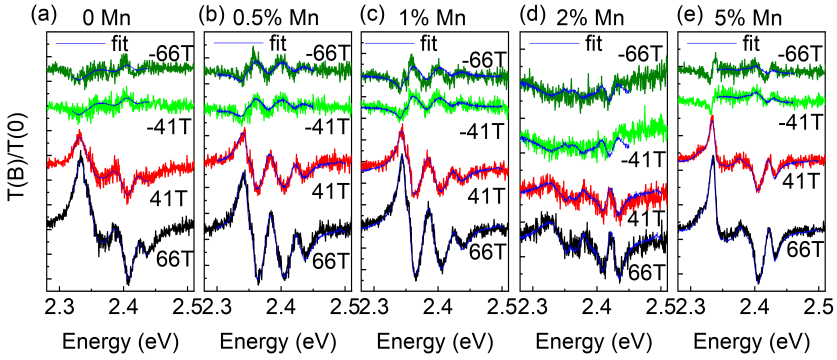

Figure 4.8: Transmission spectra of $(PEA)_2PbI_4$ perovskites doped with (a) 0% Mn, (b) 0.5% Mn, (c) 1% Mn, (d) 2% Mn and (e) 5% Mn taken at selected magnetic fields divided by the zero magnetic field spectra together with the fits (blue curves) using equation 4.10.

field, the ratio spectra can be expressed by the following formula:

$$\frac{T_B(E)}{T_0(E)} = \frac{AT_0(E+\triangle E)+C}{T_0(E)}, \tag{4.10}$$

where $T_B(E)$ and $T_0(E)$ represent transmission spectra at a selected magnetic field and zero field. A and C are constant in order to take any possible change of the transmission amplitude. $\triangle E$ is the energy shift of the transmission resonance at a selected magnetic field. To extract the value of $\triangle E$, we use the least-squares method to fit the experimental curves. In Fig.4.8, blue curves represent fits, which

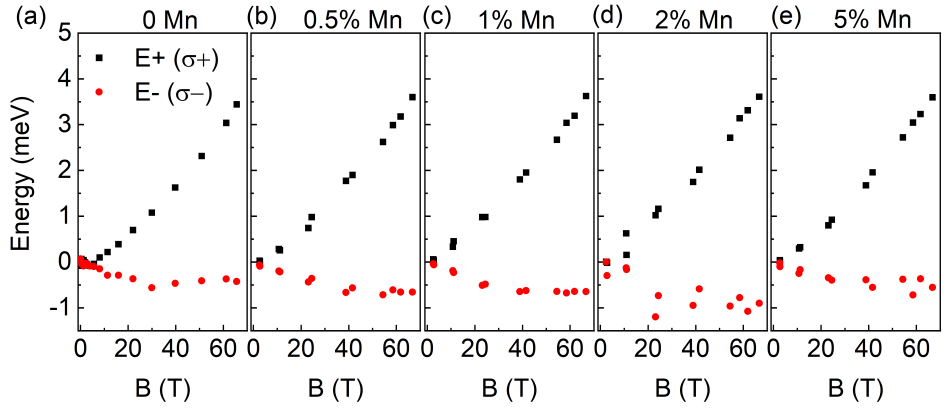

Figure 4.9: Shift of the transmission spectra of $(PEA)_2Pb_{1-x}Mn_xI_4$ samples at positive magnetic fields E_+ (σ^+) and negative magnetic field E_- (σ^-). From (a) to (e), Mn concentration $x = 0$ to 5%, respectively.

agree very well with the experimental results of T(B)/T(0). This method allows us to precisely extract the shift of excitonic transition even at a very low field.

We apply this method to all of our $(PEA)_2Pb_{1-x}Mn_xI_4$ samples to extract the shift of 1s excitonic transition as well as its phonon replicas in magnetic fields, and

the results are shown in Fig.4.9 (a-e) for Mn concentration $x = 0$ to 5%, respectively. The transition energy of the 1s exciton, together with the phonon replicas show a blue-shift in positive magnetic fields, as the black points show in Fig.4.9, labelled as E+ ($\sigma+$), and show a red-shift in the negative magnetic fields, labelled as E- ($\sigma-$), as shown by the red points.

4.3.4 Results and discussion

In the weak field limit, the characteristic transition energy of 2D perovskites related to the Coulomb interaction (the exciton binding energy), is much larger than the cyclotron energy of the carriers ($\hbar eB/\mu$). In the Faraday configuration, with the light wave vector parallel to the magnetic field ($\mathbf{k} \parallel \mathbf{B}$), in the weak field limit, the magnetic field-induced shift of the excitonic transition is described as,

$$\Delta E_{\pm} = \pm\frac{1}{2}g\mu_B B + c_0 B^2, \tag{4.11}$$

where g is the Landé g-factor, μ_B is the Bohr magneton and c_0 is the diamagnetic coefficient. The linear component is related to the Zeeman splitting and the quadratic component is simply the diamagnetic shift. We can rewrite equation 4.11 to separate the different components as follows,

$$E_+ - E_- = g\mu_B B, \tag{4.12}$$

$$\frac{E_+ + E_-}{2} = c_0 B^2. \tag{4.13}$$

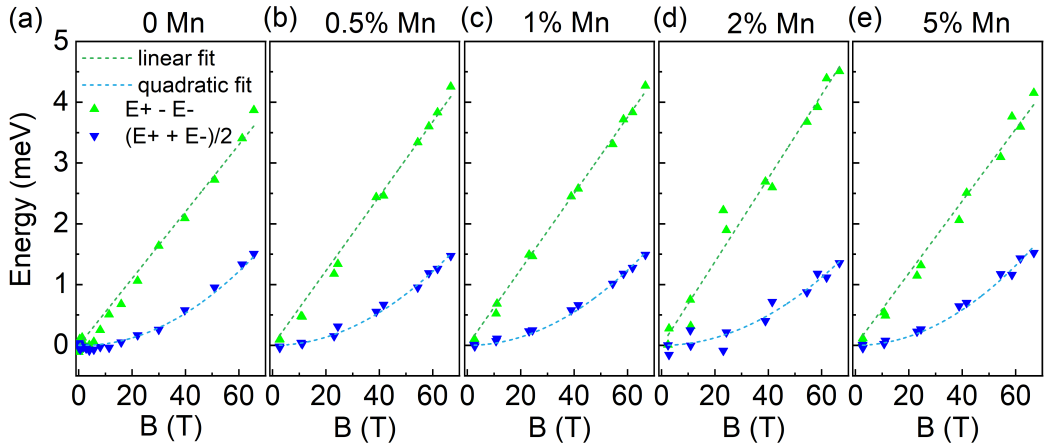

Figure 4.10: Determined Zeeman splitting (green triangles) and diamagnetic shift (blue triangles) together with linear fits and quadratic fits according to equation 4.12 and equation 4.13, respectively. From (a) to (e), Mn concentration x = 0 to 5%, respectively.

According to the experimental results of E_+ and E_- in Fig.4.9, we can easily calculate E_+ - E_- and $(E_+ + E_-)/2$. We start from the pure sample and show

calculated results of E_+ - E_- and $(E_+ + E_-)/2$ in Fig.4.10 (a) as green triangles and blue triangles, respectively. To determine the value of g-factor, we fit the linear branch (green triangles) in Fig.4.10 using equation 4.12. To extract the diamagnetic coefficient, we fit the quadratic branch (blue triangles) using equation 4.13. The linear and quadratic fits are also shown in Fig.4.10 as green dashed line and blue dashed line, respectively. Finally, we apply these methods to other $(PEA)_2Pb_{1-x}Mn_xI_4$ samples ($x = 0.5\%$ to 5%, shown in Fig.4.10 (b-e), respectively) and summarize the fitting results in Table 4.1.

Table 4.1: Summary of fitting results of g-factor and diamagnetic coefficient c_0 according to equation 4.12 and equation 4.13 respectively for $(PEA)_2Pb_{1-x}Mn_xI_4$ samples ($x = 0$ to 5%).

Mn concentration x	g	c_0 ($\mu eV/T^2$)
0	0.949 ± 0.019	0.354 ± 0.007
0.5%	1.058 ± 0.017	0.338 ± 0.007
1%	1.079 ± 0.009	0.343 ± 0.006
2%	1.186 ± 0.033	0.311 ± 0.017
5%	1.023 ± 0.021	0.365 ± 0.009

The value of the diamagnetic coefficient for pure $(PEA)_2PbI_4$ perovskite is $0.354\,\mu eV/T^2$, which agrees well with our group's previous experimental result ($0.36\,\mu eV/T^2$) [Dyksik 2020]. Additionally, we can see from Table 4.1, the values of the diamagnetic coefficient show no significant difference among pure $(PEA)_2PbI_4$ perovskite and 5% Mn doped $(PEA)_2PbI_4$ sample ($0.365\,\mu eV/T^2$), which suggests the similar diamagnetic shifts in magnetic field as well as the correspondingly similar Bohr radii, exciton binding energies and effective masses for all of these samples.

Now let us move to the discussion of the g-factors. To make the trend of g-factors versus Mn concentrations in Table 4.1 more intuitive, we plot the g-factor as a function of Mn concentration, as shown in Fig.4.11. The g-factor increases with the increasing Mn concentration x up to 2%, which can be attributed to the sp-d exchange interaction between the band-edge exciton and the local magnetic moments of the Mn ions. However, the g-factor decreases when x is further increased up to 5% because Mn-Mn interactions become important and couple neighbouring atoms, which will saturate the magnetization of the Mn doped perovskite [Larson 1985, Larson 1988, Furdyna 1988, Gaj 2010].

In order to unravel the contribution to g-factor of the sp-d exchange interaction between the exciton and the local magnetic moments of the Mn ions, we use an empirical model described in the introduction to this chapter (see equation 4.9) in which we modify g in equation 4.12 as the sum of two terms,

$$g_{eff} = g_0 + x g_{\text{sp-d}}, \tag{4.14}$$

where g_{eff} represents the effective g-factor, g_0 is the exciton g-factor for $x = 0$, x is the Mn concentration and $g_{\text{sp-d}}$ is a constant term which accounts for the

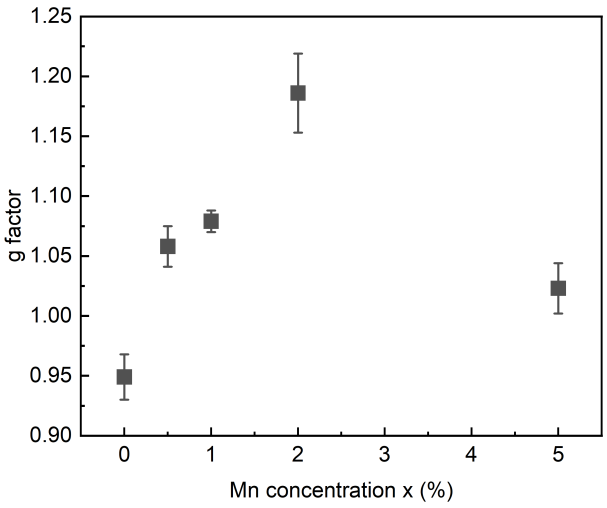

Figure 4.11: g-factor as a function of Mn concentration of $(PEA)_2Pb_{1-x}Mn_xI_4$ samples with $x = 0$ to 5%.

contribution of the sp-d exchange interaction. From the linear fit of the experimental values of g_{eff} (here we neglect the g-factor of $x = 5\,\%$ sample) to equation 4.14, we extract the values of $g_0 = 0.971 \pm 0.023$ and $g_{\text{sp-d}} = 0.111 \pm 0.025$, as shown in Fig.4.12. We find that with increasing Mn concentration up to 2%, the sp-d exchange interaction tends to dominate the intrinsic Zeeman splitting.

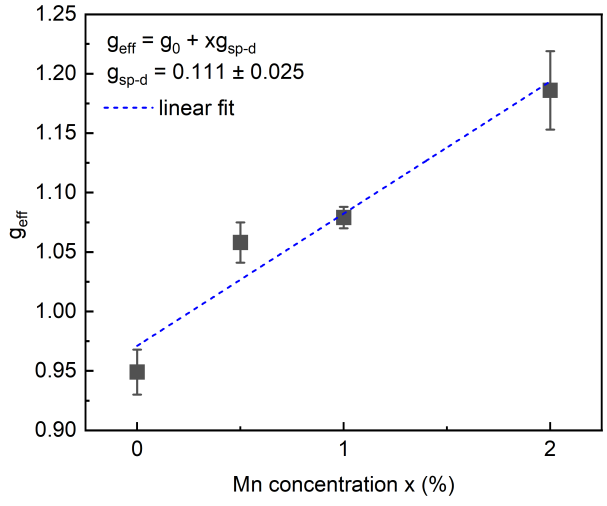

Figure 4.12: g-factor as a function of Mn concentration of $(PEA)_2Pb_{1-x}Mn_xI_4$ samples with $x = 0$ to 2%. Blue dashed line is a linear fit according to equation 4.14.

4.4 Conclusion

In summary, we have presented a systematic change of the magneto-optical properties of 2D $(PEA)_2PbI_4$ perovskite doped with an increasing concentration of magnetic Mn-impurities via applying large out-of-plane magnetic fields up to 66 T at $T = 2.2$ K. We find that the exciton g-factor can be modified by the sp-d exchange interaction between the band-edge exciton and the local magnetic Mn ions. Our magneto-transmission results suggest a systematic increase of the exciton g-factor with increasing Mn concentration from $x = 0$ to 2%. We determine the constant $g_{\text{sp-d}} = 0.111 \pm 0.025$ which represents the contribution of sp-d exchange interaction. However, with further increasing Mn concentration up to 5%, the exciton g factor decreases, which we attributes to the Mn-Mn interactions.

Chapter 5

Conclusions

Two-dimensional (2D) metal halide perovskites are a new class of semiconducting materials that may find applications in various technologically important fields. Because of the better moisture and illumination stability, 2D layered perovskites can be the next generation of materials for light emitting diodes, thin film transistors, photodetectors and lasers. Moreover, the nonmagnetic layered perovskites can be semi magnetic semiconductor by introducing magnetic impurities such as manganese ions into lattices of the host perovskites. Mn-doped layered perovskites simultaneously possess excellent semiconducting and magnetic properties, which can be promising materials for opto-spintronic functionality for information and communication technologies. Understanding the fundamental physical properties of these novel semiconductor materials is essential and beneficial for their potential applications. In this thesis, we reported new results of electronic properties of colloidal $CsPbBr_3$ nanoplatelets and Mn-doped layered $(PEA)_2PbI_4$ perovskites based on magneto-optical spectroscopy.

We have investigated exciton fine structures of $CsPbBr_3$-based nanoplatelets with a different thickness of the lead-halide slab, ranging from two to four layers of the lead-halide octahedral plane (2 ML to 4 ML). The applied large in-plane magnetic fields up to 64 T mixed the dark and bright excitonic states and brightened the optically inactive dark state, which allows us to directly observe an enhancement of the PL emission on the low-energy side of the spectrum, indicating that the dark excitonic state is the lowest-lying state in these nanoplatelets. Furthermore, we have demonstrated the evolution of the dark-bright exciton splitting as a function of octahedral thickness, where with the decreasing inorganic octahedral thickness, the dark-bright exciton splitting increases due to the enhanced exciton confinement. We have also demonstrated that the efficient emission from these materials is due to a phonon bottleneck, which significantly reduces the relaxation of the photon excited excitons to the optically inactive dark state.

Finally, we have explored the electronic properties of Mn-doped layered $(PEA)_2PbI_4$ perovskites with Mn concentration x varying from 0 to 5%. We have precisely determined the electronic g-factor by transmission measurements at out-of-plane magnetic fields up to 66 T. Moreover, we have demonstrated the evolution of the g-factor as a function of Mn concentration. We have observed a systematic increase of the exciton g-factor with increasing Mn concentration from x = 0 to 2% due to the sp-d exchange interaction between the band-edge exciton and the local magnetic Mn ions. We have determined the constant $g_{sp-d} = 0.111 \pm 0.025$ which represents the contribution of sp-d exchange interaction. Additionally, we

have observed that with further increasing Mn concentration up to 5%, the exciton g-factor decreases, which attributes to the Mn-Mn interactions.

Appendix A

Résumé de la thèse en français

Dans cette annexe, nous présentons un résumé en français de ce travail de thèse. Le lecteur ne trouvera aucune nouvelle information et les figures utilisées sont les mêmes que dans la version anglaise.

A.1 Introduction

A.1.1 Structure pérovskite

L'origine des matériaux pérovskites remonte à la découverte du titanate de calcium ($CaTiO_3$) dans les montagnes de l'Ural, en Russie, en 1839. Les pérovskites doivent leur nom à leur découvreur, le minéralogiste russe Lev Perovski [Katz 2020]. Aujourd'hui, tous les matériaux ayant la même structure cristalline que le minéral $CaTiO_3$ sont appelés pérovskites. La formule chimique générique des pérovskites-cristaux ioniques- est ABX_3, où A et B sont deux cations de tailles très différentes, et X est un anion.

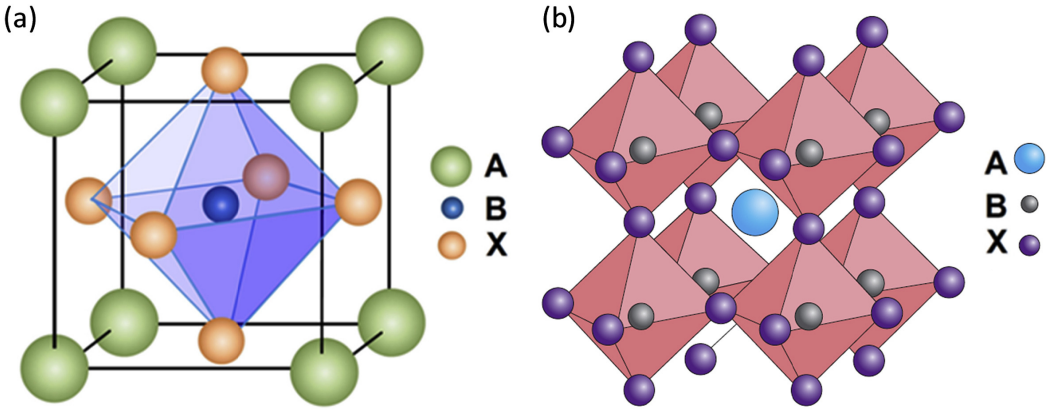

Figure A.1: (a) Cellule unitaire de pérovskite avec la formule chimique ABX_3. Les sphères vertes, bleu foncé et orange représentent les cations A, B et l'anion X. (b) La structure en réseau étendu des pérovskites liées par l'octaèdre BX_6. Les sphères bleu clair, grises et violettes représentent les cations A, B et l'anion X. Figure réimprimée après référence [Moniruddin 2018].

Dans la Fig.A.1 (a), nous montrons schématiquement une cellule unitaire de pérovskite en phase cubique. Le plus grand cation A est situé à l'angle, le plus petit cation B se trouve au centre du corps, et six anions X sont situés au centre de la

face cubique. Dans une structure pérovskite, le plus petit cation B et les six anions X forment un octaèdre BX_6, où le cation B est situé au centre de l'octaèdre, et les anions X sont situés aux angles autour du cation B. L'octaèdre BX_6 forme un réseau tridimensionnel en connectant tous les coins, tandis que les cations A remplissent les vides parmi l'octaèdre, comme le montre la Fig.A.1 (b).

A.1.2 Pérovskites à halogénures métalliques bidimensionnelles

Dans le cas des pérovskites à halogénure métallique, B est généralement un métal divalent lourd, typiquement du plomb (Pb^{2+}) ou de l'étain (Sn^2+), X sont des ions halogénure, le plus souvent du chlorure (Cl^-), du bromure (Br^-) ou de l'iodure (I^-), ou une combinaison alliée de ceux-ci. Les pérovskites d'halogénure métallique bidimensionnelles (2D), en tant que matériaux en couches, peuvent être structurellement dérivées des matériaux en vrac par adaptation le long de la direction cristallographique $< 100 >$ [Mitzi 1995, Liang 2020]. La séparation entre les couches et l'épaisseur des couches octaédriques du BX_6 peuvent être réglées par le choix de grands cations organiques pendant la croissance du cristal. Les grands cations organiques ne s'intègrent pas dans la structure octaédrique. En fait, ils jouent le rôle de "barrière" et de "couvercle" pour les pérovskites en vrac, ce qui conduit à la formation de la structure en couches (voir Fig.A.2). En général, la formule chimique de ces pérovskites en couches est $A'_2A_{n-1}B_nX_{3n+1}$ ($1 \leq n \leq \infty$), où A′ représente un grand cation organique tel que le monoammonium (R-NH_3^+) et diammonium (^+H_3N-R-NH_3^+, R désigne une chaîne alkyle ou un ligand aromatique) [Zhang 2021].

Par rapport aux matériaux pérovskites massifs, une meilleure stabilité environnementale a été observée dans les pérovskites hybrides 2D. En effet, dans une structure de pérovskite 2D, de grands ligands organiques incorporés protègent efficacement les cages octaédriques BX_6 [Lin 2018, Smith 2014]. De plus, les pérovskites 2D peuvent être considérées comme une nouvelle classe de matériaux à structure confinée qui possèdent d'excellentes propriétés physiques. En 1986, Maruyama *et al.* ont rapporté pour la première fois ce nouveau matériau stratifié: des pérovskites hybrides organiques-inorganiques à base de plomb avec $n = 1$ [Dolzhenko 1986]. En 1988, Ishihara *et al.* ont étudié l'état excitonique dans la pérovskite 2D $(C_{10}H_{21}NH_3)_2PbI_4$. Ils ont trouvé que l'exciton a une grande énergie de liaison de 370 meV et est très stable même à température ambiante [Ishihara 1989]. Une grande énergie de liaison des excitons réduit les performances photovoltaïques des pérovskites en couches en raison de la structure confinée des puits quantiques. Cependant, elle fait des pérovskites 2D des candidats prometteurs pour l'application des diodes électroluminescentes (LED) en raison de la recombinaison radiative hautement efficace résultant de leur structure de puits quantique [Zhang 2021, Bohn 2018, Vescio 2022, Yuan 2020]. Le premier dispositif LED basé sur une pérovskite en couches a été signalé en 1994 par Era *et al.* , qui ont fabriqué un émetteur en pérovskite $C_6H_5C_2H_4NH_3PbI_4$ présentant une excellente électroluminescence à la température de l'azote liquide [Era 1994]. En 2014, Tan

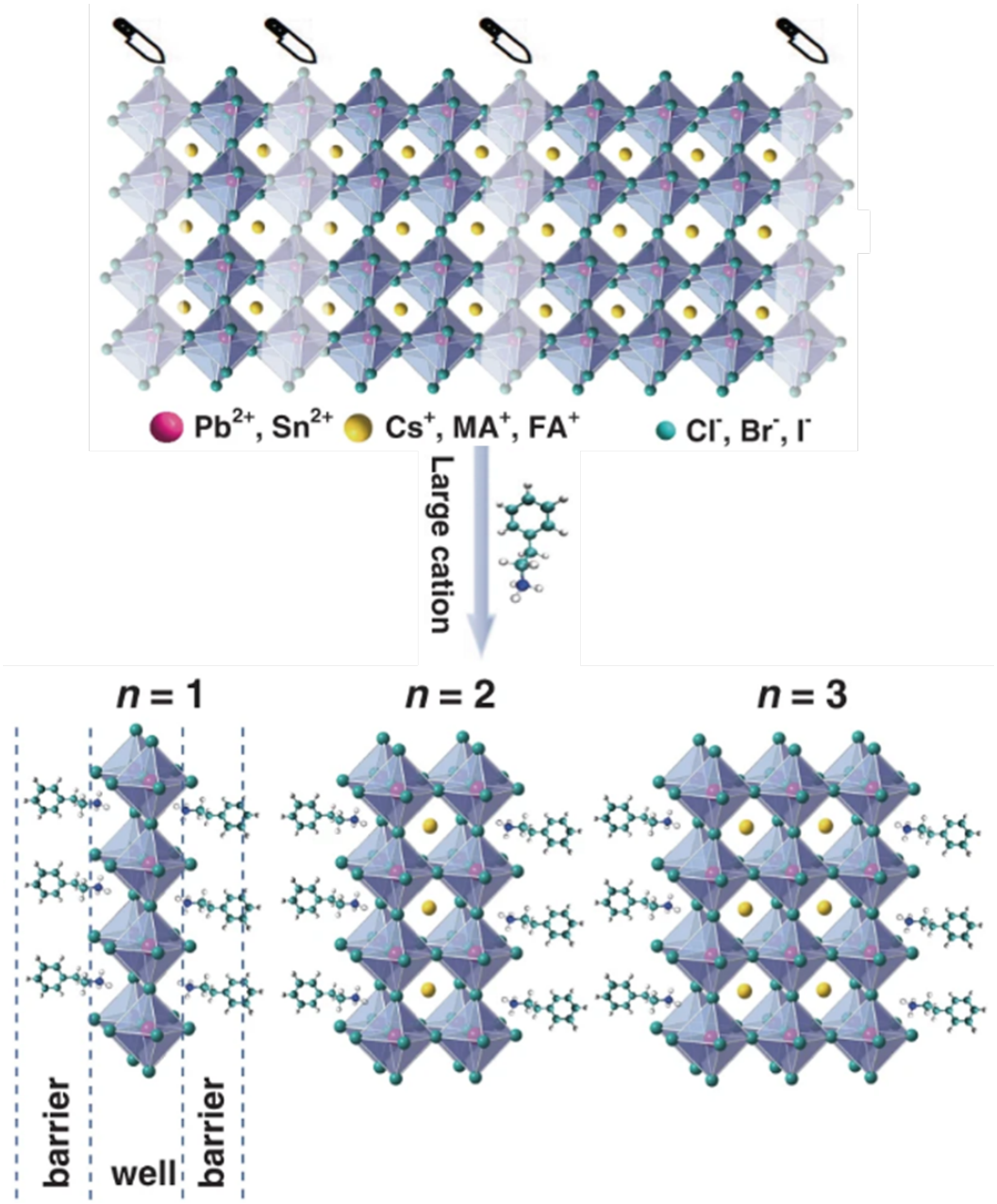

Figure A.2: Structures cristallines schématiques de la pérovskite brute (en haut) et de la pérovskite 2D avec différentes épaisseurs de couches octaédriques (en bas). Les pérovskites 2D sont obtenues en adaptant la pérovskite brute le long de la direction cristallographique $< 100 >$. Figure réimprimée après référence [Zhang 2021].

et al. ont rapporté le premier dispositif LED à température ambiante basé sur la pérovskite stratifiée $CH_3NH_3PbI_{3-x}Cl_3$ avec le rendement quantique externe (EQE) et le rendement quantique interne les plus élevés de $0,76\%$ et $3,4\%$, respectivement [Tan 2014]. Depuis lors, des progrès significatifs ont été réalisés dans les dispositifs

LED à base de pérovskite 2D, où l'EQE a dépassé 23% [Bao 2023].

A.2 Techniques expérimentales

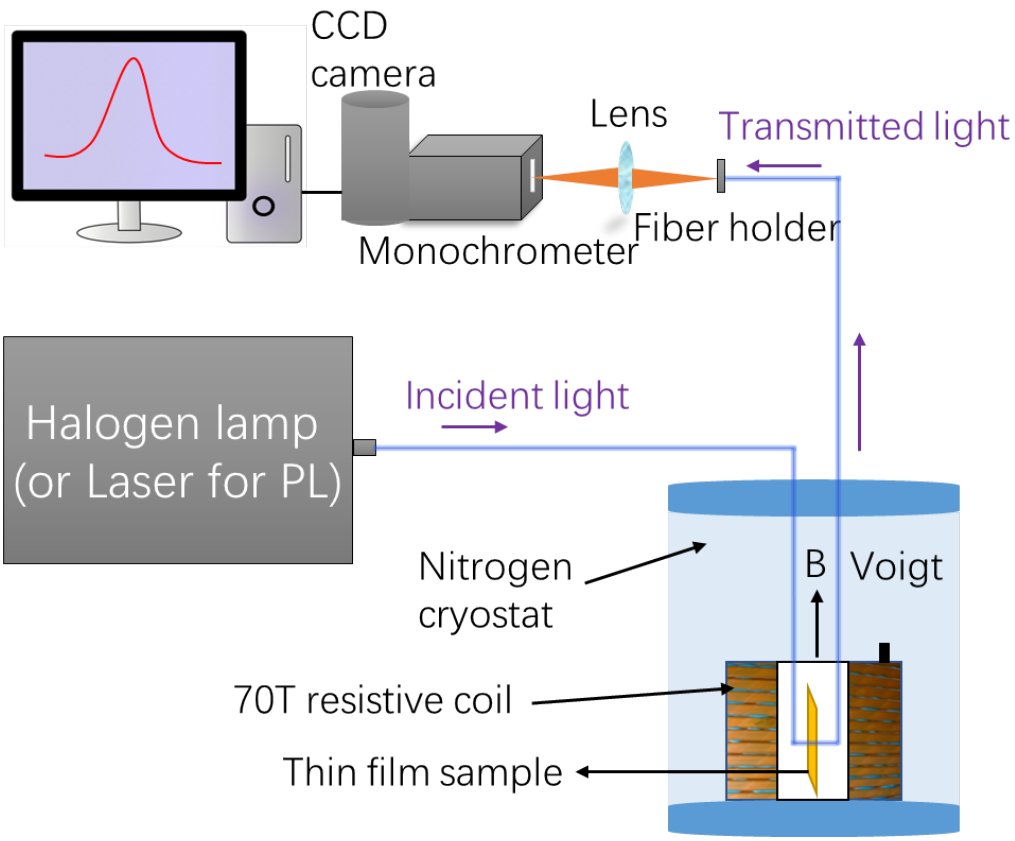

Figure A.3: Dessin schématique (non à l'échelle) de la mesure de la transmission en champ magnétique pulsé (représenté ici dans la géométrie de Voigt). La même configuration est également utilisée pour la mesure de la photoluminescence (PL) dans un champ magnétique pulsé.

Afin d'explorer les propriétés optiques des pérovskites 2D dans un champ magnétique élevé, un dispositif spécial, qui nous permet de mesurer à la fois la transmission et la photoluminescence (PL) de l'échantillon de film mince dans le champ magnétique, a été construit dans le LNCMI-T. La Fig.A.3 montre schématiquement le schéma de cette installation.

En général, un échantillon de film mince est placé au centre de l'aimant. Pour la mesure de la magnéto-transmission, une lampe halogène à large bande est utilisée pour fournir la lumière incidente à l'aide d'une fibre optique. La lumière transmise, collectée par une deuxième fibre optique, est dispersée par un monochromateur équipé d'un réseau de diffraction, et détectée à l'aide d'une caméra CCD refroidie à l'azote liquide, qui est synchronisée avec l'impulsion du champ magnétique. De

même, pour la mesure du magnéto-PL, nous utilisons un laser à onde continue comme excitation, et nous recueillons la lumière émise par l'échantillon qui est envoyée au monochromètre. Devant la fente du monochromètre, nous plaçons un filtre passe long correspondant pour bloquer le laser transmis afin que seul le signal de l'échantillon soit détecté.

A.3 Spectroscopie magnéto-optique sur des nanoplaquettes à base de $CsPbBr_3$

Dans cette section, les résultats de la division d'exciton sombre-brillant dépendant de l'épaisseur dans les nanoplaquettes à base de $CsPbBr_3$, révélés par spectroscopie magnéto-optique sont présentés. En appliquant de grands champs magnétiques dans le plan jusqu'à 65 T, les états sombres optiquement inactifs des nanoplaquettes à base de $CsPbBr_3$ ont été éclaircis pour la première fois. Nous démontrons que l'état sombre optiquement inactif est l'état le plus bas dans ces nanoplaquettes de différentes épaisseurs. Avec la diminution de l'épaisseur de l'octaèdre inorganique, la séparation des excitons sombres et brillants augmente en raison du confinement accru des excitons. Par ailleurs, le spectre de magnéto-photoluminescence (PL) suggère que les populations des états sombre et brillant ne sont pas thermalisées, ce qui confirme la présence d'un goulot d'étranglement phononique dans le processus de relaxation de l'exciton. Les résultats présentés dans cette section ont été publiés dans Nano Letters, **22**, 7011-7019 (2022).

A.3.1 Description des échantillons

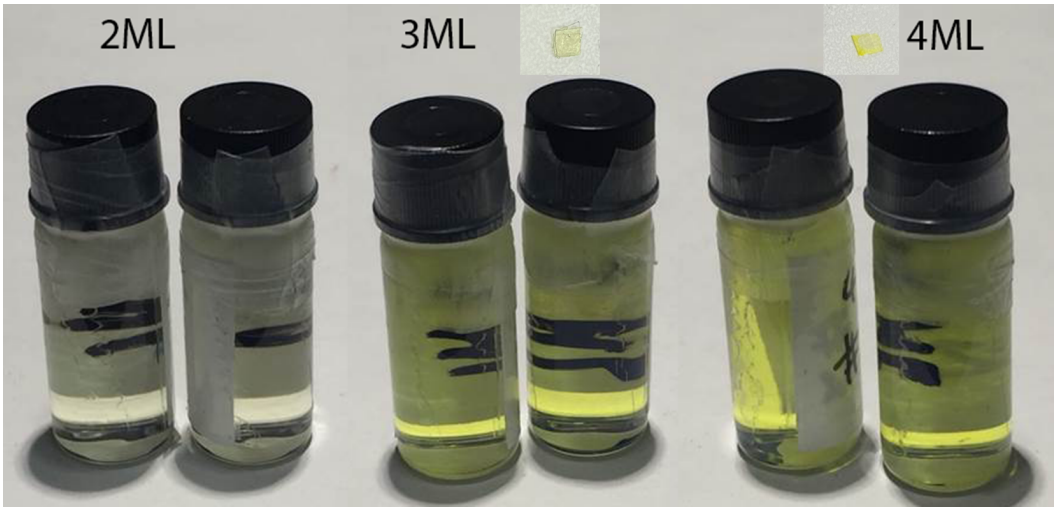

Figure A.4: Solutions de nanoplaquettes à base de $CsPbBr_3$ avec l'épaisseur de 2-4 plans d'octaèdres d'halogénure de plomb (2-4 ML). L'encart montre des films minces coulés en gouttes représentatifs pour des nanoplaquettes de 3 ML et 4 ML.

Les nanoplaquettes à base de $CsPbBr_3$ ont été produites dans le groupe d'Alexander Urban à la Ludwig-Maximilians-Universität München (LMU). Ces nanoplaquettes colloïdales ont été synthétisées par une méthode de reprécipitation à température ambiante, et l'épaisseur, qui varie de 2 à 4 plans d'octaèdres d'halogénure de plomb (2-4 ML), peut être contrôlée avec précision en modifiant le rapport molaire des précurseurs. La Fig.A.4 présente les solutions de nanoplaquettes à base de $CsPbBr_3$ avec des épaisseurs de 2 ML à 4 ML. Ces solutions de nanoplaquettes hautement dispersées présentent une différence de couleur caractéristique, même à la lumière naturelle. Les nanoplaquettes de 4 ML présentent une couleur jaune vif, qui devient progressivement plus claire pour les solutions de 3 ML et 2 ML. Afin d'avoir des échantillons frais, nous avons fabriqué les films minces au LNCMI-T en utilisant les solutions colloïdales synthétisées en Allemagne. Pour le dépôt à la goutte, la solution de nanoplaquettes a été aspirée dans une seringue puis déposée, goutte à goutte, sur un substrat en verre de $1.8 \times 5\,\text{mm}$, que nous avions préalablement nettoyé aux ultrasons dans de l'éthanol et séché à l'air libre. Des films minces représentatifs de nanoplaquettes de 3 ML et 4 ML d'épaisseur sont présentés dans l'encart de la Fig.A.4. La couleur jaune de la couche mince constitue une indication fiable de la présence d'un nombre suffisant de nanoplaquettes à la surface du substrat de verre.

A.3.2 Mesures optiques sur des nanoplaquettes de $CsPbBr_3$

Commençons par les spectres optiques des nanoplaquettes de $CsPbBr_3$ d'une épaisseur de 2 ML à 4 ML, mesurés à champ magnétique nul et à $T = 5\,\text{K}$. Dans la Fig.A.5, nous montrons les spectres d'absorption pour chaque épaisseur. Chacun des spectres montre une seule résonance excitonique. Afin de déterminer exactement l'énergie de transition excitonique 1s et la bande interdite, nous avons modélisé les spectres d'absorption avec une formule généralisée d'Elliott 2D (voir equation3.5) [Elliott 1957, Shinada 1966, Campi 1995, Chen 2021]. Les énergies extraites de la transition de l'exciton 1s (E_{1s}) et de la bande interdite (E_g) sont représentées en fonction de l'épaisseur de la nanoplaquette dans la Fig.A.6 (a). Nous observons que les deux énergies augmentent lorsque l'épaisseur des couches octaédriques diminue. En effet, d'une part, le confinement quantique décale les bandes de conduction et de valence de d'une part, le confinement quantique déplace les bandes de conduction et de valence de $\hbar^2\pi^2/2m_{e,h}d^2$, où m_e et m_h sont la masse de l'électron et du trou, respectivement, et d est l'épaisseur du puits quantique, et d'autre part, le changement des forces de Coulomb dans le puits quantique à constante diélectrique plus élevée renormalise également les niveaux d'énergie, ce qui entraîne une augmentation de la bande interdite et de l'énergie de transition excitonique 1s avec la diminution de l'épaisseur d du puits quantique.

Pour l'état excitonique fondamental, l'énergie de liaison de l'exciton est donnée par $E_b = E_g - E_{1s}$. Les effets de confinement quantique et diélectrique augmentent non seulement la bande interdite mais aussi l'énergie de liaison des excitons. Dans la Fig.A.6 (b), nous présentons les énergies de liaison des excitons (E_b) en fonction de

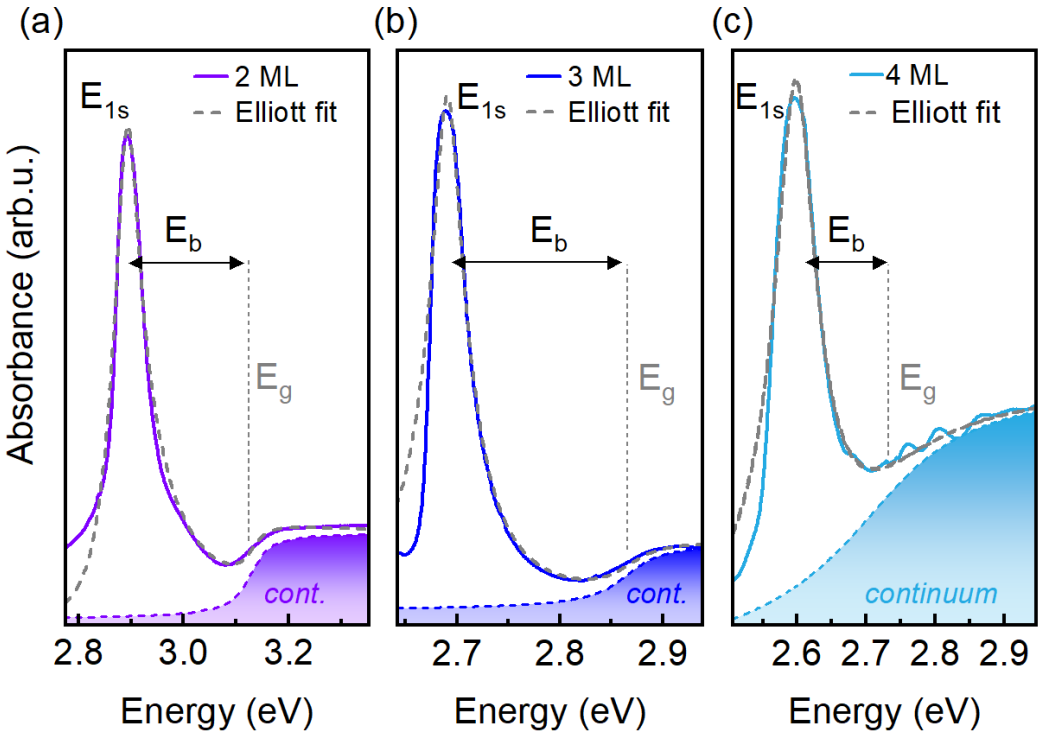

Figure A.5: (a-c) Spectres d'absorption de nanoplaquettes de 2-4 ML d'épaisseur (lignes continues) ajustés à l'aide de la formule d'Elliot, *i.e.* équation 3.5 (lignes grises en pointillés). La contribution du continuum au spectre d'absorption est représentée par une courbe ombrée sous chaque spectre.

l'épaisseur de la nanoplaquette. L'énergie de liaison des excitons des nanoplaquettes 4 ML est de 133 meV. Avec la diminution de l'épaisseur des couches octaédriques, l'énergie de liaison des excitons augmente jusqu'à 177 meV (3 ML) et jusqu'à 237 meV (2 ML), en raison des effets de confinement quantique et diélectrique fortement renforcés. Cette tendance correspond bien au résultat rapporté pour les pérovskites 2D à halogénure de Ruddlesden-Popper $(BA)_2(MA)_{n-1}Pb_nI_{3n+1}$ (BA et MA représentent respectivement $CH_3(CH_2)_3NH_3$ et CH_3NH_3) avec le nombre de couches n variant de 5 à 1, ce qui conduit à une augmentation de l'énergie de liaison de l'exciton de 125 meV à 470 meV [Blancon 2018], et notre résultat précédent de pérovskites 2D $(PEA)_2(MA)_{n-1}Pb_nI_{3n+1}$ (PEA représente $C_6H_5C_2H_4NH_3$) avec n variant de 3 à 1 donnant lieu à l'augmentation de E_b de 78 meV à 265 meV [Dyksik 2021b]. La valeur E_b de 237 meV des nanoplaquettes les plus fines (2 ML), correspond aux résultats du groupe d'Alexander Urban, qui a obtenu une valeur de 280 meV à température ambiante [Bohn 2018], et du groupe de Jing Li qui a déterminé cette valeur à 127 meV [Li 2017].

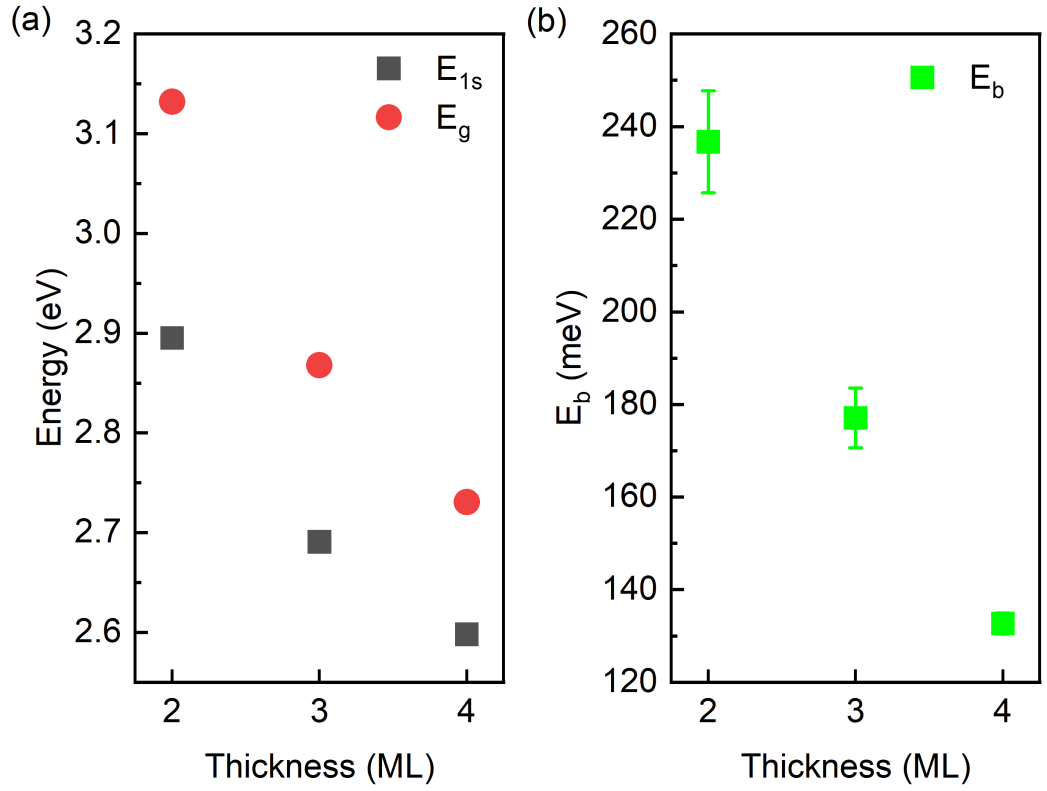

Figure A.6: (a) Energies de la transition de l'exciton 1s (E_{1s}) et de la bande interdite (E_g). (b) Énergie de liaison de l'exciton (E_b) mesurée en fonction de l'épaisseur de la nanoplaquette.

A.3.3 Spectres magnéto-optiques

Nous nous intéressons maintenant aux spectres optiques des nanoplaquettes de $CsPbBr_3$ mesurés à des champs magnétiques élevés jusqu'à 65 T dans la configuration de Voigt ($\mathbf{k} \perp \mathbf{B}$) et à $T = 2.2$ K. Ici, nous montrons d'abord les spectres de magnéto-transmission résolus dans la polarisation longitudinale ($\mathbf{E} \parallel \mathbf{B}$) de nanoplaquettes de 2 ML, 3 ML et 4 ML d'épaisseur dans la Fig.A.7. Pour chaque échantillon, la forme de la ligne des spectres de magnétotransmission ne change pas avec l'augmentation du champ magnétique, même jusqu'à 65 T, ce qui suggère que la caractéristique de transmission est principalement liée à l'absorption des états exciton brillants (BX).

Pour explorer davantage la structure fine de l'exciton, nous effectuons des mesures magnéto-PL sur des nanoplaquettes à base de $CsPbBr_3$ dont l'épaisseur des octaèdres varie de 2 ML à 4 ML. Nous partons de la polarisation de la lumière longitudinale au champ magnétique ($\mathbf{E} \parallel \mathbf{B}$). Dans la Fig.A.8, nous montrons l'évolution globale du spectre PL en fonction du champ magnétique appliqué dans le plan. Le spectre PL des nanoplaquettes de 2 ML d'épaisseur, représenté sur la Fig.A.8 (a), se compose du pic principal et d'un pic plus faible à haute énergie,

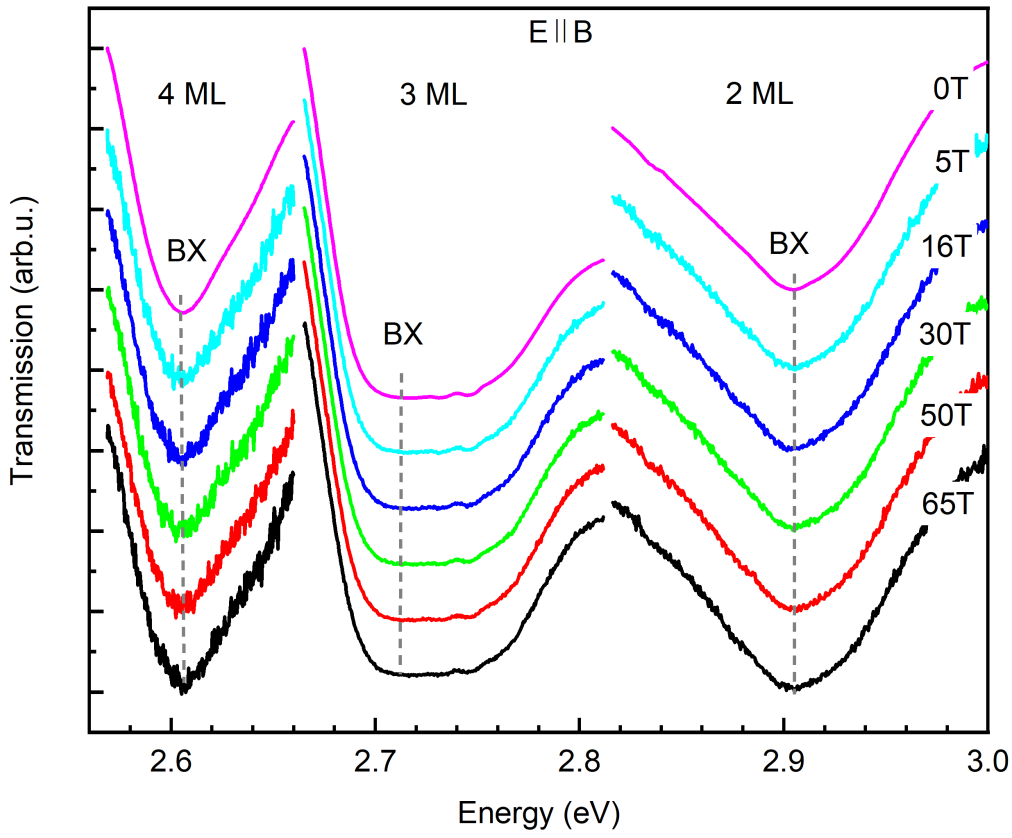

Figure A.7: Spectres de transmission de nanoplaquettes de 2 ML, 3 ML et 4 ML d'épaisseur mesurés aux valeurs indiquées du champ magnétique pour **E** ∥ **B**. BX représente l'exciton brillant et les lignes pointillées grises sont dessinées pour guider l'œil.

dont l'énergie correspond au minimum du spectre de transmission (≃2.90 eV) à champ nul. Ceci suggère fortement que le pic de haute énergie est lié à la recombinaison d'excitons brillants (BX), la seule espèce ayant une force d'oscillation suffisamment forte pour produire une absorption significative à champ magnétique nul. L'émission BX s'affaiblit avec l'augmentation du champ magnétique avant de disparaître à un champ magnétique intermédiaire autour de 30 T, comme le montre l'encart de la Fig.A.8 (a). Simultanément, le pic aux énergies inférieures augmente significativement en amplitude, et domine complètement l'émission PL aux champs magnétiques élevés jusqu'à 64 T. Nous attribuons ce phénomène à l'exciton sombre (DX), qui, en tant qu'état le plus bas, a une grande occupation thermique, ce qui conduit à un éclaircissement significatif lorsque la force de l'oscillateur est considérablement augmentée par le mélange des états induit par le champ magnétique. Pour les nanoplaquettes 3 ML, dans l'ensemble, l'intensité PL du pic principal avec une énergie autour de 2.66 eV augmente fortement avec l'augmentation

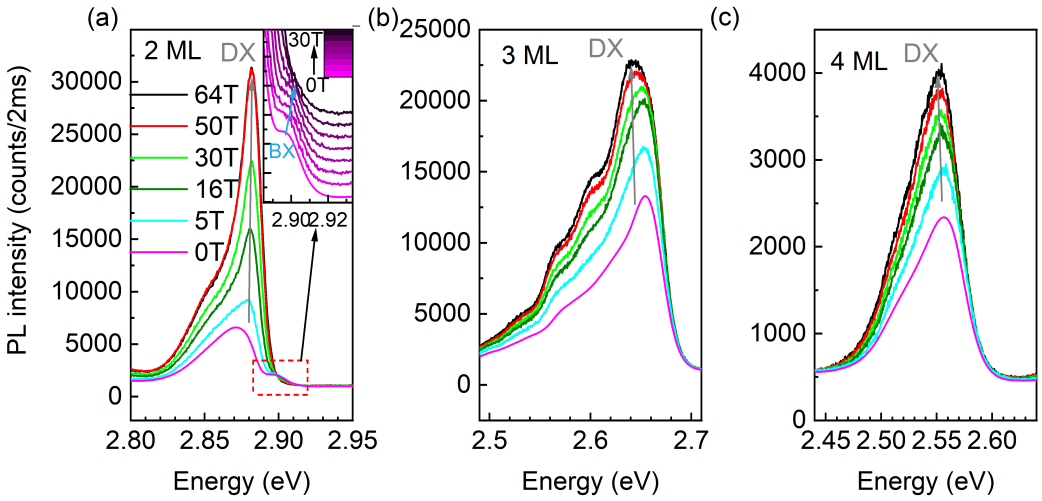

Figure A.8: Spectres Magnéto-PL dans la configuration Voigt de (a) 2 ML, (b) 3 ML et (c) 4 ML nanoplaquettes, mesurés en polarisation longitudinale ($\mathbf{B} \parallel \mathbf{E}$) jusqu'à 64 T à $T = 2.2$ K. Les pics attribués à l'exciton brillant et à l'exciton sombre sont marqués par BX et DX, respectivement. Les flèches sont dessinées pour guider l'œil. L'encart du panneau (a) montre l'émission brillante d'exciton à des champs magnétiques sélectionnés jusqu'à 30 T.

du champ magnétique, comme le montre la Fig.A.8 (b). De plus, un épaulement supplémentaire à $\simeq 2.64$ eV est observé sur le spectre PL à 64 T, qui pourrait également être attribué à l'émission d'exciton sombre éclaircie. La Fig.A.8 (c) montre les spectres magnéto-PL de l'échantillon 4 ML. Nous pouvons clairement voir que l'énergie du pic principal se décale légèrement vers le rouge (comme prévu pour l'émission d'exciton sombre) et que l'intensité PL augmente considérablement avec l'augmentation du champ magnétique.

A.3.4 Résultats de la division d'exciton sombre-brillant

La dépendance du champ magnétique de l'énergie des états brillant et sombre, obtenue en ajustant les spectres de magnéto-transmission dans la polarisation longitudinale (voir Fig.A.7) et les spectres de magnéto-PL (voir Fig.A.8), est montrée dans la Fig.A.9 (a-c). L'évolution prédite à l'aide de l'équation (3.4a) reproduit bien les décalages vers le bleu et vers le rouge observés et nous permet d'extraire le fractionnement obscurité-lumière du champ nul. Le fractionnement sombre-brillant obtenu, illustré à la Fig.A.9 (d), augmente avec la diminution de l'épaisseur de la dalle inorganique de nanoplaquettes, passant de $\simeq 9$ meV pour les nanoplaquettes de 4 ML à $\simeq 21$ meV pour les nanoplaquettes de 2 ML, en raison du confinement accru des excitons. Les fractionnements rapportés ici sont légèrement plus petits que ceux mesurés dans des nanoplaquettes synthétisées avec une approche très similaire [Gramlich 2022b], ce qui peut être dû à une taille légèrement plus grande dans

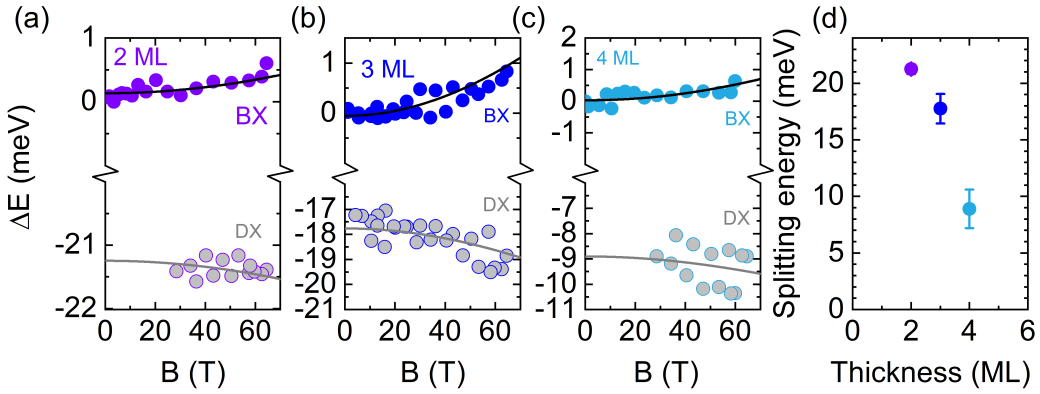

Figure A.9: (a-c) Dépendance du champ magnétique des énergies des transitions d'exciton sombre et brillant par rapport à l'énergie de transition à champ nul de l'état brillant ΔE pour des nanoplaquettes de 2-4 ML. Les lignes sont des ajustements des données en utilisant l'équation (3.4a). (d) Mesure du fractionnement clair-obscur en fonction de l'épaisseur de la nanoplaquette.

le plan des nanoplaquettes étudiées dans notre étude et à un confinement dans le plan réduit de manière concomitante. Cependant, ces valeurs sont toujours considérablement plus importantes que la division sombre-brillant des nanocubes conventionnels [Tamarat 2019, Chen 2018], qui présentent un confinement bien moindre [Takagahara 1993].

Une diminution de l'épaisseur de la couche octaédrique dans les nanoplaquettes entraîne une augmentation de l'énergie de liaison de l'exciton, comme le montre la Fig.A.6 (b), en raison des effets diélectriques et de confinement quantique plus importants dans les puits quantiques de pérovskite colloïdale [Fu 1999, Ghribi 2021, Ben Aich 2020], qui conduisent également à l'augmentation de la division sombre-lumineuse de l'exciton. Dans la Fig.A.10, nous montrons la division obscurité-lumière obtenue en fonction de l'énergie de liaison de l'exciton (reprise de la Fig.A.6 (b)). Comme prévu, le fractionnement sombre-brillant augmente systématiquement avec l'augmentation de l'énergie de liaison des excitons.

A.3.5 Résultats de l'intensité de la photoluminescence et du goulot d'étranglement des phonons

.

Pour corroborer notre affectation des pics PL, nous analysons les intensités des états d'exciton brillants et sombres, présentés à la Fig.A.11 (a-c). Nous normalisons tous les pics à l'intensité du pic de l'exciton sombre à champ magnétique nul. L'intensité de l'émission de l'état sombre augmente considérablement, tandis que celle de l'état brillant diminue légèrement avec l'augmentation du champ magnétique. Ce résultat est tout à fait cohérent avec le transfert attendu de la force de l'oscillateur dû au mélange clair-obscur induit par le champ magnétique dans la géométrie de Voigt. Les nanoplaquettes de 2 ML d'épaisseur présentent la plus

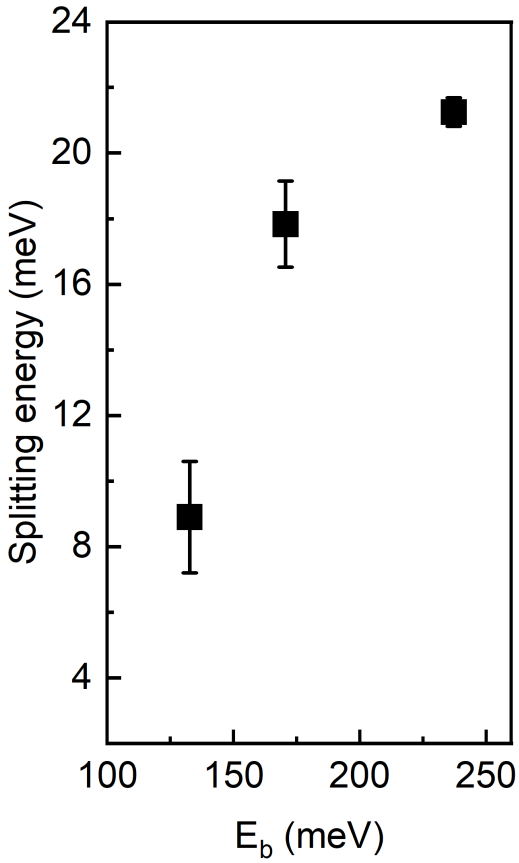

Figure A.10: Séparation de l'énergie sombre et lumineuse à $B = 0$ T en fonction de l'énergie de liaison de l'exciton E_b (E_b est tiré de la Fig.A.6 (b)).

forte augmentation de l'intensité PL. Cela peut paraître surprenant à première vue, étant donné que l'équation (3.3b) prévoit qu'une grande différence d'énergie entre l'obscurité et la lumière correspond à un petit gain de la force de l'oscillateur de l'exciton obscur. Cependant, l'intensité du PL est liée au produit de l'occupation de l'état et de la force de l'oscillateur. Par conséquent, la population nettement plus importante de l'état d'exciton sombre des nanoplaquettes les plus fines peut expliquer sa plus grande intensité magnéto-PL, comme nous l'expliquons en détail ci-dessous.

Dans la Fig.A.11 (d), nous traçons la dépendance du champ magnétique du rapport entre l'intensité des états sombres, I_D, et des états brillants, I_B, que nous calculons comme suit

$$\frac{I_{\mathrm{D}}(B)}{I_{\mathrm{B}}(B)} = \frac{d_1^2(B)}{d_{3\mathrm{L}}^2(B) + d_{3\mathrm{T}}^2(B)} e^{-\frac{E_1 - E_{3\mathrm{L}}}{k_B T}}, \tag{A.1}$$

où le facteur de Boltzmann $e^{-\frac{E_1 - E_{3\mathrm{L}}}{k_B T}}$ tient compte du rapport de population entre les états sombre et brillant [Dyksik 2021a], d_1, d_{3L} et d_{3T} sont des coefficients issus

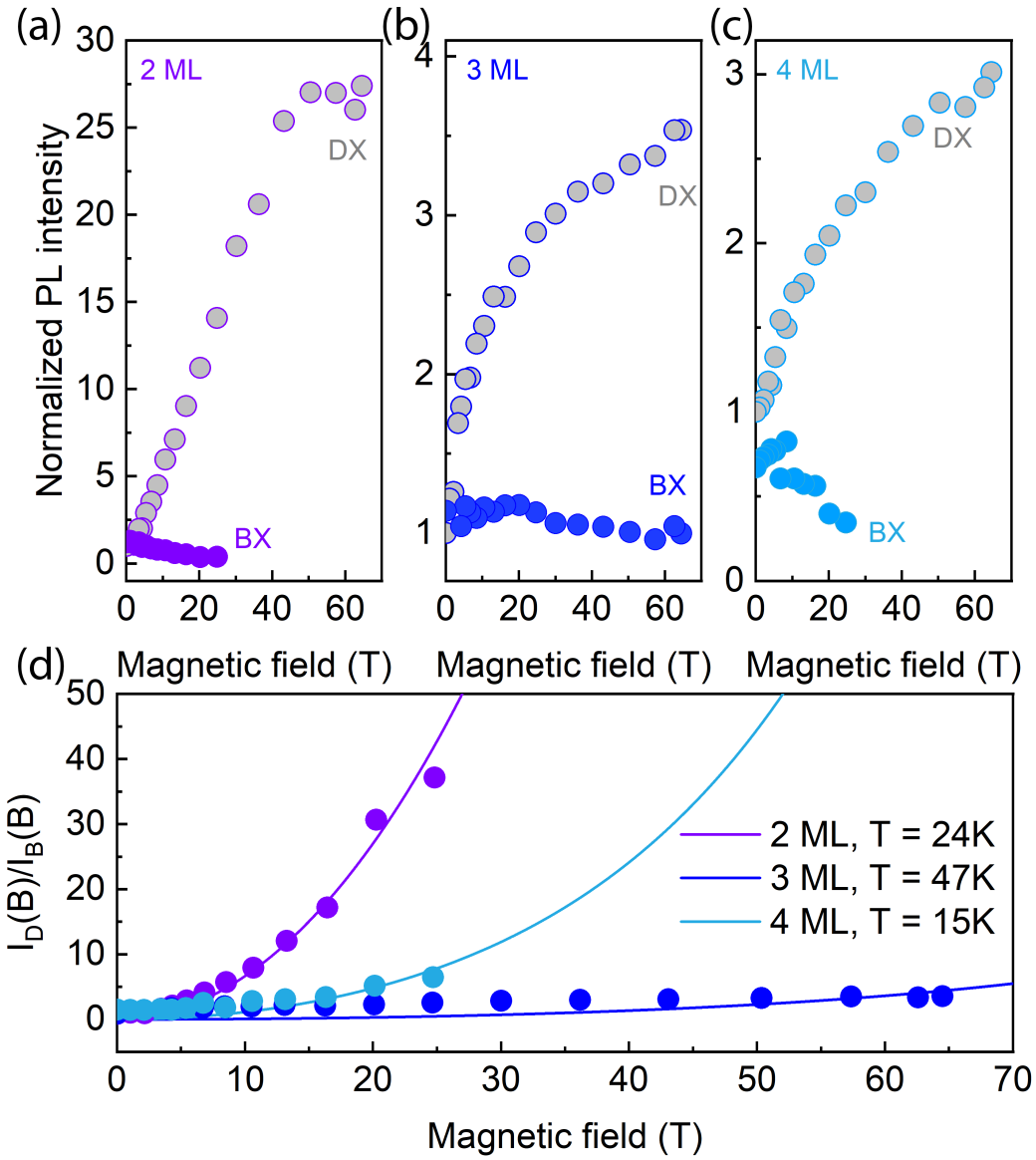

Figure A.11: (a-c) Dépendance au champ magnétique de l'intensité des transitions d'exciton sombre et brillant normalisée à l'intensité de la transition d'exciton sombre à champ magnétique nul pour des nanoplaquettes de 2-4 ML d'épaisseur. (d) Rapport d'intensité PL entre les états sombres et brillants des excitons pour les trois épaisseurs de nanoplaquettes étudiées en fonction du champ magnétique appliqué. Les cercles pleins représentent les points expérimentaux. Les courbes sont calculées à l'aide de l'équation (3.11) et la température supposée est indiquée dans l'encadré.

des équations 3.3b et 3.3d. Pour simplifier, nous négligeons ici la présence d'états excitoniques localisés. En raison de l'état sombre considérablement plus peuplé dans les nanoplaquettes de 2 ML d'épaisseur, l'intensité PL de l'état sombre est plus forte dans les nanoplaquettes plus fines, comme le montre la Fig.A.11 (d). Il est important

de noter que pour reproduire les données expérimentales (voir Fig.A.11 (d)), nous avons dû utiliser une température effective d'exciton de $T = 24\,\mathrm{K}$ pour 2 ML, $T = 47\,\mathrm{K}$ pour 3 ML et $T = 15\,\mathrm{K}$ pour 4 ML selon l'équation A.1, comme les courbes indiquées à la Fig.A.11 (d). Ces températures sont au moins d'un ordre de grandeur supérieur à la température du réseau de $\simeq 2\,\mathrm{K}$ (température expérimentale). Ce décalage entre la température du réseau et la température effective de l'exciton suggère que la population d'exciton n'est pas complètement thermalisée au moment de la recombinaison [Dyksik 2021a].

Cette observation peut être expliquée à la lumière de la structure des niveaux d'énergie du collecteur d'exciton, en combinaison avec les processus de relaxation particuliers des pérovskites à halogénure métallique. En raison de l'interaction d'échange fortement renforcée dans un système fortement confiné [Takagahara 1993], les fractionnements dans le collecteur d'excitons dépassent les énergies des phonons optiques longitudinaux (LO), avec des énergies de $\simeq 12$ à $15\,\mathrm{meV}$ et $\simeq 30$ à $40\,\mathrm{meV}$ [Du 2019, Gramlich 2021, Straus 2016], auxquels les excitons peuvent se coupler pour dissiper efficacement l'énergie excédentaire. Le couplage des excitons aux phonons acoustiques est faible dans les matériaux mous des pérovskites en vrac et bidimensionnelles. En outre, en raison de la conservation de la quantité de mouvement et de l'énergie, le changement d'énergie dans un processus de diffusion unique est de l'ordre de $0.1\,\mathrm{meV}$ [Dyksik 2021a]. Par conséquent, les phonons acoustiques ne peuvent pas diffuser efficacement les excitons de l'état brillant à l'état sombre. Par exemple, dans le cas des nanoplaquettes de 4 ML d'épaisseur, une relaxation plus efficace de l'exciton vers l'état sombre pourrait être conduite par un phonon LO de $\simeq 9\,\mathrm{meV}$ [Du 2019], auquel, cependant, les porteurs ne se couplent pas très efficacement [Gramlich 2021]. Ce décalage énergétique entre les phonons LO et les séparations sombre-lumineux, associé au couplage pratiquement négligeable des porteurs aux phonons acoustiques dans les pérovskites à halogénure métallique [Straus 2019], conduit à la population d'excitons hautement non-thermalisés visible sur la Fig.A.11 (d) et soutient la présence d'un goulot d'étranglement phononique dans les nanocristaux de pérovskite fortement confinés. dans les nanocristaux de pérovskite fortement confinés.

A.4 Spectroscopie de magnéto-transmission sur les pérovskites $(PEA)_2Pb_{1-x}Mn_xI_4$

Dans cette section, nous présentons les résultats des mesures de magnéto-transmission sur la perovskite 2D $(PEA)_2Pb_{1-x}Mn_xI_4$ (PEA est le phénéthylammonium, $x = 0$, 0.5%, 1%, 2% et 5%, respectivement). En appliquant de grands champs magnétiques hors du plan (configuration Faraday) jusqu'à $66\,\mathrm{T}$, nous extrayons les splits Zeeman. Nous démontrons que le facteur g de l'exciton augmente avec la concentration de Mn jusqu'à $x = 2\%$ en raison de l'interaction d'échange sp-d entre l'exciton de bord de bande et les ions magnétiques de Mn. Cependant, lorsque la concentration en Mn augmente à 5%, le facteur g diminue et la valeur

est comparable à celle du matériau à 0.5%, ce qui est attribué aux interactions d'échange d-d entre les ions Mn et Mn. Certains des résultats présentés dans cette section ont été publiés dans Nature Communications, **12**, 3489 (2021).

A.4.1 Description des échantillons

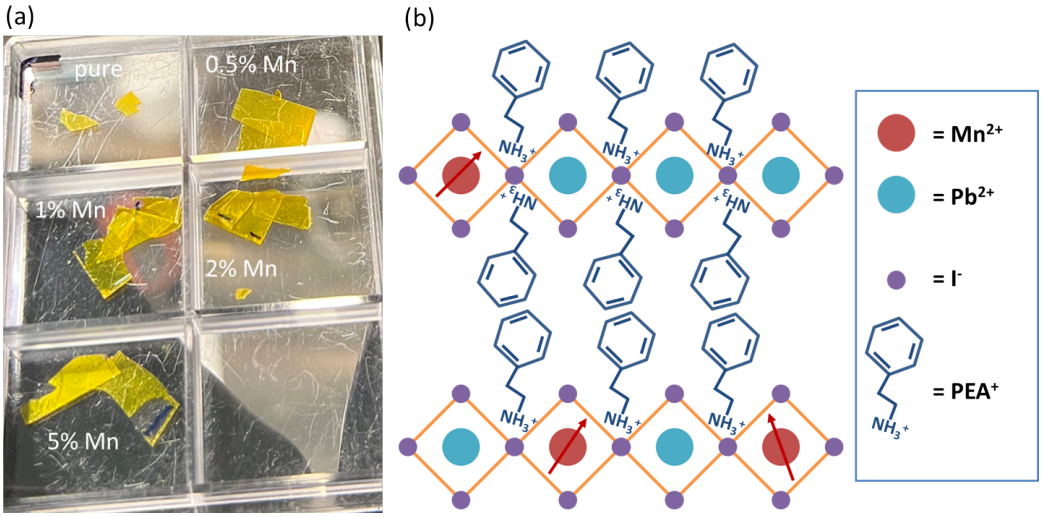

Figure A.12: (a) (a) Films minces de $(PEA)_2Pb_{1-x}Mn_xI_4$ pour des concentrations de manganèse $x = 0$, 0.5%, 1%, 2% et 5%. (b) Structure cristalline schématique de la couche dopée au Mn $(PEA)_2PbI_4$. Les ions Mn^{2+} sont situés au centre des octaèdres des pérovskites hôtes $(PEA)_2PbI_4$ en substituant les cations divalents Pb^{2+}.

Les échantillons de $(PEA)_2Pb_{1-x}Mn_xI_4$ ont été fabriqués dans le groupe de Felix Deschler à l'Université technique de Munich en Allemagne. Une solution pure de $(PEA)_2PbI_4$ a été synthétisée en dissolvant des sels de PbI_4 (LumTech, >99.999%) et d'iodure de phénéthylammonium (LumTech, >99.5%) dans des N,N-diméthylformamides (Sigma, >99.8% anhydre) dans un rapport molaire de 1:2. Puis la solution a été agitée pendant 2 heures à 80 °C, filtrée. avec un filtre à seringue en PTFE de 0.2 μm de porosité.

Pour les solutions de $(PEA)_2PbI_4$ dopées au Mn, toutes les étapes et les conditions ont été les mêmes que pour la synthèse de l'échantillon pur, sauf que le précurseur PbI_4 a été remplacé par les précurseurs mélangés PbI_2 et $MnBr_2$ dans une proportion correspondant au rapport atomique recherché rapport atomique souhaité. Des échantillons de films minces ont été préparés à partir des solutions de $(PEA)_2Pb_{1-x}Mn_xI_4$. Les solutions ont été coulées en gouttes sur des lamelles de verre traitées par plasma d'oxygène et les solvants ont été évaporés à 120 °C pendant 2 heures [Neumann 2021]. Des films minces représentatifs, comprenant un échantillon de $(PEA)_2PbI_4$ pur, et des échantillons de $(PEA)_2PbI_4$ dopés au Mn avec une concentration en Mn x de 0.5% à 5%, sont présentés sur la Fig.A.12 (a).

Ils ont tous une couleur jaune vif caractéristique. Pour mieux comprendre la différence structurelle entre la pérovskite pure et l'échantillon dopé au Mn, dans la Fig.A.12 (b), nous montrons schématiquement la structure cristalline intrinsèque de la pérovskite $(PEA)_2PbI_4$ dopée au Mn. Les impuretés magnétiques, les ions Mn^{2+}, sont situées au centre des octaèdres des pérovskites hôtes $(PEA)_2PbI_4$ en substituant les cations divalents Pb^{2+} divalents.

A.4.2 Spectres de magnéto-transmission sur des échantillons de $(PEA)_2Pb_{1-x}Mn_xI_4$

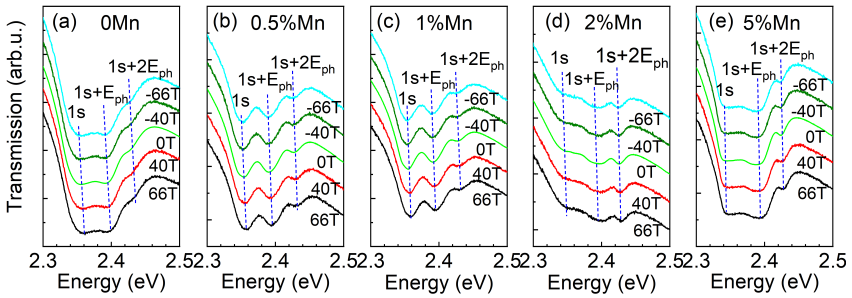

Figure A.13: Spectres de transmission résolus en polarisation d'échantillons dopés au manganèse (a) 0, (b) 0.5%, (c) 1%, (d) 2% et (e) 5% pour des champs magnétiques sélectionnés à $T = 2.2\,\mathrm{K}$. L'inversion de la direction du champ magnétique nous permet de détecter la polarisation en $\sigma^{\pm}$. Les lignes pointillées mettent en évidence le déplacement de l'état excitonique 1s ainsi que des répliques de phonons dans les champs magnétiques.

Dans la Fig.A.13, nous montrons la transmission des pérovskites 2D $(PEA)_2PbI_4$ dopées au Mn avec des concentrations de Mn x de 0 à 5% mesurées à des champs magnétiques positifs et négatifs sélectionnés jusqu'à 66 T dans la configuration Faraday ($\mathbf{k} \parallel \mathbf{B}$). Les lignes pointillées mettent en évidence les décalages d'énergie de la transition excitonique 1s ainsi que les répliques de phonons, qui présentent toutes les mêmes décalages d'énergie que les transitions 1s dans le champ magnétique. Les transitions passent à une énergie supérieure ou inférieure selon la direction du champ magnétique. Les champs magnétiques positifs représentent les composantes de polarisation circulaire à droite (σ^+) et donnent lieu à un décalage vers le bleu de l'énergie de transition excitonique, tandis que les champs magnétiques négatifs représentent les composantes de polarisation circulaire à gauche (σ^-) et entraînent un décalage vers le rouge de l'énergie de transition.

A.4.3 Résultats et discussion

Dans la limite du champ faible, l'énergie de transition caractéristique des pérovskites 2D liée à l'interaction de Coulomb (l'énergie de liaison des excitons), est beaucoup plus grande que l'énergie cyclotronique des porteurs ($\hbar eB/\mu$). Dans la configuration

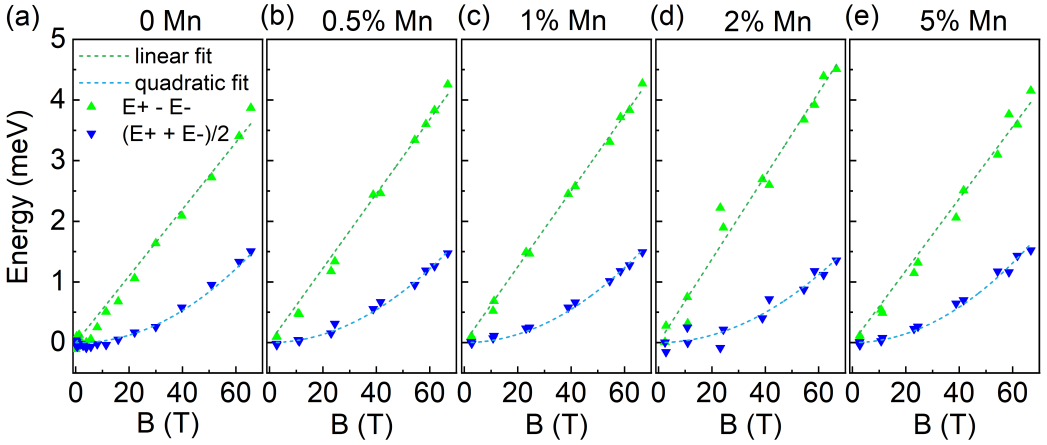

Figure A.14: Détermination du fractionnement Zeeman (triangles verts) et du déplacement diamagnétique (triangles bleus) ainsi que des ajustements linéaires et quadratiques selon l'équation A.3 et l'équation A.4, respectivement. De (a) à (e), concentration de Mn $x = 0$ à 5%, respectivement.

de Faraday, avec le vecteur d'onde lumineux parallèle au champ magnétique ($\mathbf{k} \parallel \mathbf{B}$), dans la limite du champ faible, le décalage de la transition excitonique induit par le champ magnétique est décrit comme suit,

$$\Delta E_{\pm} = \pm\frac{1}{2} g\mu_B B + c_0 B^2, \tag{A.2}$$

où g est le facteur g de Land'e, μ_B est le magnéton de Bohr et c_0 est le coefficient diamagnétique. La composante linéaire est liée au fractionnement Zeeman et la composante quadratique est simplement le déplacement diamagnétique. Nous pouvons réécrire l'équation A.2 pour séparer les différentes composantes comme suit,

$$E_+ - E_- = g\mu_B B, \tag{A.3}$$

$$\frac{E_+ + E_-}{2} = c_0 B^2. \tag{A.4}$$

D'après les résultats expérimentaux de E_+ et E_-, obtenus en ajustant les spectres de transmission de la Fig.A.13, nous pouvons facilement calculer E_+ - E_- et $(E_+ + E_-)/2$. Nous partons de l'échantillon pur et montrons les résultats calculés de E_+ - E_- et $(E_+ + E_-)/2$ dans la Fig.A.14 (a) sous forme de triangles verts et de triangles bleus, respectivement. Pour déterminer la valeur du facteur g, nous ajustons la branche linéaire (triangles verts) de la Fig.A.14 en utilisant l'équation A.3. Pour extraire le coefficient diamagnétique, nous ajustons la branche quadratique (triangles bleus) en utilisant l'équation A.4. Les ajustements linéaires et quadratiques sont également présentés à la Fig.A.14 sous forme de ligne pointillée verte et de ligne pointillée bleue, respectivement. Enfin, nous appliquons ces méthodes à d'autres échantillons de $(PEA)_2Pb_{1-x}Mn_xI_4$ ($x = 0.5\%$ à 5%, représentés sur les Fig.A.14 (b-e), respectivement) et résumons les résultats de l'ajustement dans le Tableau A.1.

Table A.1: Résumé des résultats de l'ajustement du facteur g et du coefficient diamagnétique c_0 selon l'équation A.3 et l'équation A.4 respectivement pour les échantillons $(PEA)_2Pb_{1-x}Mn_xI_4$ ($x = 0$ à 5%).

Mn concentration x	g	c_0 ($\mu eV/T^2$)
0	0.949 ± 0.019	0.354 ± 0.007
0.5%	1.058 ± 0.017	0.338 ± 0.007
1%	1.079 ± 0.009	0.343 ± 0.006
2%	1.186 ± 0.033	0.311 ± 0.017
5%	1.023 ± 0.021	0.365 ± 0.009

La valeur du coefficient diamagnétique pour la pérovskite $(PEA)_2PbI_4$ pure est de $0.354\,\mu eV/T^2$, ce qui correspond bien au résultat expérimental précédent de notre groupe ($0.36\,\mu eV/T^2$) [Dyksik 2020]. De plus, nous pouvons voir dans le Tableau A.1 que les valeurs du coefficient diamagnétique ne présentent aucune différence significative entre la pérovskite $(PEA)_2PbI_4$ pure et l'échantillon $(PEA)_2PbI_4$ dopé à 5% de Mn ($0.365\,\mu eV/T^2$), ce qui suggère des décalages diamagnétiques similaires dans le champ magnétique ainsi que des rayons de Bohr, des énergies de liaison des excitons et des masses effectives correspondants similaires pour tous ces échantillons.

Passons maintenant à la discussion des facteurs g. Le facteur g augmente avec l'augmentation de la concentration en Mn x jusqu'à 2%, ce qui peut être attribué à l'interaction d'échange sp-d entre l'exciton de bord de bande et les moments magnétiques locaux des ions Mn. Cependant, le facteur g diminue lorsque x est augmenté jusqu'à 5% car les interactions Mn-Mn deviennent importantes et couplent les atomes voisins, ce qui sature la magnétisation de la pérovskite dopée au Mn [Larson 1985, Larson 1988, Furdyna 1988, Gaj 2010].

Afin d'élucider la contribution au facteur g de l'interaction d'échange sp-d entre l'exciton et les moments magnétiques locaux des ions Mn, nous utilisons un modèle empirique (voir l'équation 4.9) dans lequel nous modifions g dans l'équation A.3 comme la somme de deux termes,

$$g_{eff} = g_0 + x g_{\text{sp-d}}, \tag{A.5}$$

où g_{eff} représente le facteur g effectif, g_0 est le facteur g de l'exciton pour $x = 0$, x est la concentration en Mn et $g_{\text{sp-d}}$ est un terme constant qui prend en compte la contribution de l'interaction d'échange sp-d. De l'ajustement linéaire des valeurs expérimentales de g_{eff} (nous négligeons ici le facteur g de l'échantillon $x = 5\%$) à l'équation A.5, nous extrayons les valeurs de $g_0 = 0.971 \pm 0.023$ et $g_{\text{sp-d}} = 0.111 \pm 0.025$, comme le montre la Fig.A.15. Nous constatons qu'avec l'augmentation de la concentration en Mn jusqu'à 2%, l'interaction d'échange sp-d tend à dominer la division Zeeman intrinsèque.

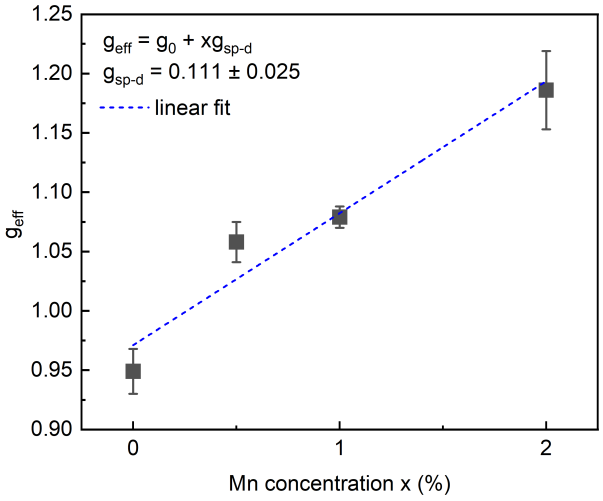

Figure A.15: Facteur g en fonction de la concentration en Mn des échantillons de $(PEA)_2Pb_{1-x}Mn_xI_4$ avec $x = 0$ à 2%. La ligne pointillée bleue est un ajustement linéaire selon l'équation A.5.

A.5 Conclusions

Les pérovskites d'halogénures métalliques bidimensionnels (2D) constituent une nouvelle classe de matériaux semi-conducteurs qui pourraient trouver des applications dans divers domaines technologiquement importants. En raison de leur meilleure stabilité à l'humidité et à l'illumination, les pérovskites en couches 2D peuvent constituer la prochaine génération de matériaux pour les diodes électroluminescentes, les transistors à couche mince, les photodétecteurs et les lasers. De plus, les pérovskites en couches non magnétiques peuvent devenir des semi-conducteurs magnétiques en introduisant des impuretés magnétiques telles que ions manganèse dans les réseaux des pérovskites hôtes. Les pérovskites en couches dopées au Mn possèdent simultanément d'excellentes propriétés semi-conductrices et magnétiques, qui peuvent être des matériaux prometteurs pour la fonctionnalité opto-spintronique des technologies de l'information et de la communication. La compréhension des propriétés physiques fondamentales de ces nouveaux matériaux semi-conducteurs est essentielle et bénéfique pour leurs applications potentielles. Dans cette thèse, nous avons rapporté de nouveaux résultats sur les propriétés électroniques des nanoplaquettes colloïdales de $CsPbBr_3$ et des pérovskites $(PEA)_2PbI_4$ dopées au Mn, basés sur la spectroscopie magnéto-optique. sur la base de la spectroscopie magnéto-optique. Nous avons étudié les structures fines d'exciton des nanoplaquettes à base de $CsPbBr_3$ avec une épaisseur différente de la dalle de plomb-halogénure, allant de deux à quatre couches du plan octaédrique du plomb-halogénure (2 ML à 4 ML). Les grands champs magnétiques appliqués dans le plan jusqu'à 64 T mélangent les états excitoniques sombres et brillants et éclaircissent l'état sombre optiquement inactif, ce qui nous permet d'observer directement une augmentation de l'émission PL du

côté basse énergie du spectre, indiquant que l'état excitonique sombre est l'état le plus bas dans ces nanoplaquettes. De plus, nous avons démontré l'évolution de la division de l'exciton sombre et brillant en fonction de l'épaisseur de l'octaèdre, où avec la diminution de l'épaisseur de l'octaèdre inorganique, la division de l'exciton sombre et brillant augmente en raison du confinement accru de l'exciton. Nous avons également démontré que l'émission efficace de ces matériaux est due à un goulot d'étranglement phononique, qui réduit considérablement la relaxation des excitons excités par des photons vers l'état sombre optiquement inactif.

Enfin, nous avons exploré les propriétés électroniques des pérovskites à couches $(PEA)_2PbI_4$ dopées au Mn avec une concentration en Mn x variant de 0 à 5%. Nous avons déterminé avec précision le facteur g électronique par des mesures de transmission à des champs magnétiques hors du plan jusqu'à 66 T. De plus, nous avons démontré l'évolution du facteur g en fonction de la concentration en Mn. Nous avons observé une augmentation systématique du facteur g de l'exciton avec l'augmentation de la concentration en Mn de $x = 0$ à 2%, due à l'interaction d'échange sp-d entre l'exciton de bord de bande et les ions magnétiques locaux de Mn. Nous avons déterminé la constante $g_{\text{sp-d}} = 0.111 \pm 0.025$ qui représente la contribution de l'interaction d'échange sp-d. De plus, nous avons observé qu'avec l'augmentation de la concentration en Mn jusqu'à 5%, le facteur g de l'exciton diminue, ce qui est attribué aux interactions Mn-Mn.

Appendix B

Publications

Publications based on the results of this thesis:

1. **S. Wang**, M. Dyksik, C. Lampe, M. Gramlich, D. K. Maude, M. Baranowski, A. S. Urban, P. Plochocka, and A. Surrente
   "Thickness-Dependent Dark-Bright Exciton Splitting and Phonon Bottleneck in $CsPbBr_3$-Based Nanoplatelets Revealed via Magneto-Optical Spectroscopy"
   Nano Letters **22(17)**, 7011-7019 (2022)

2. T. Neumann, S. Feldmann, P. Moser, A. Delhomme, J. Zerhoch, T. van de Goor, **S. Wang**, M. Dyksik, T. Winkler, J. J. Finley, P. Plochocka, M. S. Brandt, C. Faugeras, A. V. Stier and F. Deschler
   "Manganese doping for enhanced magnetic brightening and circular polarization control of dark excitons in paramagnetic layered hybrid metal-halide perovskites"
   Nature Communications **12**, 3489 (2021)

Other publications:

1. M. Dyksik, **S. Wang**, W. Paritmongkol, D. K. Maude, W. A. Tisdale, M. Baranowski and P. Plochocka
   "Tuning the Excitonic Properties of the 2D $(PEA)_2(MA)_{n-1}Pb_nI_{3n+1}$ Perovskite Family via Quantum Confinement"
   The Journal of Physical Chemistry Letters **12(6)**, 1638-1643 (2021)

2. D. Feldstein, R. P. Causin, **S. Wang**, M. Dyksik, K. Watanabe, T. Taniguchi, P. Plochocka and E. Malic
   "Microscopic Picture of Electron-Phonon Interaction in Two-Dimensional Halide Perovskites"
   The Journal of Physical Chemistry Letters **11(23)**, 9975-9982 (2020)

Bibliography

[Aggarwal 1983] RL Aggarwal, n SN Jasperson, z J Stankiewicz, Y Shapira, S Foner, B Khazai and A Wold. *Magnetoreflectance at the band edge in Cd 1- x Mn x Se.* Physical Review B, vol. 28, no. 12, page 6907, 1983. (Cited on page 64.)

[Anbuselvan 2021] D Anbuselvan, S Nilavazhagan, A Santhanam, N Chidhambaram, KV Gunavathy, Tansir Ahamad and Saad M Alshehri. *Room temperature ferromagnetic behavior of nickel-doped zinc oxide dilute magnetic semiconductor for spintronics applications.* Physica E: Low-dimensional Systems and Nanostructures, vol. 129, page 114665, 2021. (Cited on page 64.)

[Ando 2000] K Ando. *Magneto-optics of diluted magnetic semiconductors: New materials and applications.* Magneto-optics, pages 211–244, 2000. (Cited on page 67.)

[Andreani 1990] Lucio Claudio Andreani and Alfredo Pasquarello. *Accurate theory of excitons in GaAs-Ga 1- x Al x As quantum wells.* Physical Review B, vol. 42, no. 14, page 8928, 1990. (Cited on page 17.)

[Azpiroz 2015] Jon M Azpiroz, Edoardo Mosconi, Juan Bisquert and Filippo De Angelis. *Defect migration in methylammonium lead iodide and its role in perovskite solar cell operation.* Energy & Environmental Science, vol. 8, no. 7, pages 2118–2127, 2015. (Cited on page 10.)

[Bao 2023] Xinyu Bao, Yanbo Gao, Yue Liu, Zehua Xu, Fujun Zhang, Min Lu, Zhennan Wu, Yanjie Wu, Quan Wang, Yu Zhang*et al. Molecular Bridging Strategy Enables High Performance and Stable Quasi-2D Perovskite Light-Emitting Devices.* ACS Energy Letters, vol. 8, pages 1018–1025, 2023. (Cited on pages 12 and 84.)

[Baranowski 2019] Michał Baranowski, Krzysztof Galkowski, Alessandro Surrente, Joanna Urban, Łukasz Kłopotowski, Sebastian Mackowski, Duncan K Maude, Rim Ben Aich, Kais Boujdaria, Maria Chamarro, Christophe Testelin, Pabrita K Nayak, Markus Dollman, Henry J Snaith, Robin J Nicholas and P Plochocka. *Giant fine structure splitting of the bright exciton in a bulk $MAPbBr_3$ single crystal.* Nano Letters, vol. 19, no. 10, pages 7054–7061, 2019. (Cited on pages 18 and 19.)

[Bauer 1992] G Bauer, Harald Pascher and W Zawadzki. *Magneto-optical properties of semimagnetic lead chalcogenides.* Semiconductor science and technology, vol. 7, no. 6, page 703, 1992. (Cited on page 64.)

[Bayer 2000] M Bayer, O Stern, A Kuther and A Forchel. *Spectroscopic study of dark excitons in $In_xGa_{1-x}As$ self-assembled quantum dots by a magnetic-field-induced symmetry breaking.* Physical Review B, vol. 61, no. 11, page 7273, 2000. (Cited on page 54.)

[Bayer 2002] M Bayer, G Ortner, O Stern, A Kuther, AA Gorbunov, A Forchel, Pawel Hawrylak, S Fafard, K Hinzer, TL Reinecke*et al. Fine structure of neutral and charged excitons in self-assembled In (Ga) As/(Al) GaAs quantum dots.* Physical Review B, vol. 65, no. 19, page 195315, 2002. (Cited on page 18.)

[Ben Aich 2020] R Ben Aich, S Ben Radhia, K Boujdaria, M Chamarro and C Testelin. *Multiband k· p model for tetragonal crystals: application to hybrid halide perovskite nanocrystals.* Journal of Physical Chemistry Letters, vol. 11, no. 3, pages 808–817, 2020. (Cited on pages 57 and 91.)

[Berry 2017] Joseph J Berry, Jao van de Lagemaat, Mowafak M Al-Jassim, Sarah Kurtz, Yanfa Yan and Kai Zhu. *Perovskite photovoltaics: the path to a printable terawatt-scale technology.* ACS Energy Letters, vol. 2, no. 11, pages 2540–2544, 2017. (Cited on page 3.)

[Bhattacharjee 1983] AK Bhattacharjee, G Fishman and B Coqblin. *Virtual bound state model for the exchange interaction in semimagnetic semiconductors such as Cd1- xMnxTe.* Physica B+ C, vol. 117, pages 449–451, 1983. (Cited on page 66.)

[Blancon 2018] J-C Blancon, Andreas V Stier, Hsinhan Tsai, Wanyi Nie, Costas C Stoumpos, Boubacar Traore, L Pedesseau, Mikael Kepenekian, Fumiya Katsutani, GT Noe*et al. Scaling law for excitons in 2D perovskite quantum wells.* Nature communications, vol. 9, no. 1, pages 1–10, 2018. (Cited on pages 15, 16, 44 and 87.)

[Bohn 2018] Bernhard J Bohn, Yu Tong, Moritz Gramlich, May Ling Lai, Markus Döblinger, Kun Wang, Robert LZ Hoye, Peter Müller-Buschbaum, Samuel D Stranks, Alexander S Urban*et al. Boosting tunable blue luminescence of halide perovskite nanoplatelets through postsynthetic surface trap repair.* Nano letters, vol. 18, no. 8, pages 5231–5238, 2018. (Cited on pages 12, 14, 15, 44, 82 and 87.)

[Boschker 2019] Hans Boschker, T Harada, T Asaba, R Ashoori, AV Boris, H Hilgenkamp, CR Hughes, ME Holtz, Lu Li, DA Muller*et al. Ferromagnetism and conductivity in atomically thin SrRuO 3.* Physical review X, vol. 9, no. 1, page 011027, 2019. (Cited on page 2.)

[Buttner 1992] RH Buttner and EN Maslen. *Structural parameters and electron difference density in BaTiO3.* Acta Crystallographica Section B: Structural Science, vol. 48, no. 6, pages 764–769, 1992. (Cited on page 2.)

[Béard 2018] Jérôme Béard, Julien Billette, Nelson Ferreira, Paul Frings, Jean-Marc Lagarrigue, Florence Lecouturier and Jean-Pierre Nicolin. *Design and Tests of the 100-T Triple Coil at LNCMI.* IEEE Transactions on Applied Superconductivity, vol. 28, no. 3, pages 1–5, 2018. (Cited on page 25.)

[Campi 1995] Domenico Campi and Claudio Coriasso. *Optical nonlinearities in multiple quantum wells: Generalized Elliott formula.* Physical Review B, vol. 51, no. 16, page 10719, 1995. (Cited on pages 42 and 86.)

[Chen 2018] Lan Chen, Bin Li, Chunfeng Zhang, Xinyu Huang, Xiaoyong Wang and Min Xiao. *Composition-dependent energy splitting between bright and dark excitons in lead halide perovskite nanocrystals.* Nano Letters, vol. 18, no. 3, pages 2074–2080, 2018. (Cited on pages 57 and 91.)

[Chen 2021] Xihan Chen, Haipeng Lu, Kang Wang, Yaxin Zhai, Vladimir Lunin, Peter C Sercel and Matthew C Beard. *Tuning spin-polarized lifetime in two-dimensional metal–halide perovskite through exciton binding energy.* Journal of the American Chemical Society, vol. 143, no. 46, pages 19438–19445, 2021. (Cited on pages 42 and 86.)

[Chernikov 2014] Alexey Chernikov, Timothy C Berkelbach, Heather M Hill, Albert Rigosi, Yilei Li, Burak Aslan, David R Reichman, Mark S Hybertsen and Tony F Heinz. *Exciton binding energy and nonhydrogenic Rydberg series in monolayer WS 2.* Physical review letters, vol. 113, no. 7, page 076802, 2014. (Cited on page 15.)

[Choi 2021] Wonkyung Choi, Seo Hyun Nam, Hyeon-Kyeong So, Sang-Eon Lee, Myung-Hwa Jung and Joon I Jang. *Impact of Dark Excitons on the Population and Relaxation Kinetics of Two-Dimensional Biexcitons in* $[CH_3(CH_2)_3NH_3]_2Pb_{1-x}Mn_xBr_4$ *(*$x = 0 - 0.09$*).* Journal of the American Chemical Society, vol. 143, no. 47, pages 19785–19793, 2021. (Cited on pages 52 and 57.)

[Cibert 2008] Joel Cibert and Denis Scalbert. *Diluted magnetic semiconductors: Basic physics and optical properties.* In Spin physics in semiconductors, pages 389–431. Springer, 2008. (Cited on page 64.)

[Davies 2018] Christopher L Davies, Marina R Filip, Jay B Patel, Timothy W Crothers, Carla Verdi, Adam D Wright, Rebecca L Milot, Feliciano Giustino, Michael B Johnston and Laura M Herz. *Bimolecular recombination in methylammonium lead triiodide perovskite is an inverse absorption process.* Nature communications, vol. 9, no. 1, pages 1–9, 2018. (Cited on page 6.)

[DeCrescent 2020] Ryan A DeCrescent, Naveen R Venkatesan, Clayton J Dahlman, Rhys M Kennard, Xie Zhang, Wenhao Li, Xinhong Du, Michael L Chabinyc, Rashid Zia and Jon A Schuller. *Bright magnetic dipole radiation from two-dimensional lead-halide perovskites.* Science advances, vol. 6, no. 6, page eaay4900, 2020. (Cited on page 72.)

[Dolzhenko 1986] Yuriy Dolzhenko, Tamotsu Inabe and Yusei. Maruyama. *In Situ X-Ray Observation on the Intercalation of Weak Interaction Molecules into Perovskite-Type Layered Crystals (C9H19NH3)2PbI4 and (C10H21NH3)2CdCl4*. Bulletin of the Chemical Society of Japan, vol. 59, pages 563–567, 1986. (Cited on pages 12 and 82.)

[Dong 2015] Qingfeng Dong, Yanjun Fang, Yuchuan Shao, Padhraic Mulligan, Jie Qiu, Lei Cao and Jinsong Huang. *Electron-hole diffusion lengths> 175 μm in solution-grown CH3NH3PbI3 single crystals*. Science, vol. 347, no. 6225, pages 967–970, 2015. (Cited on page 3.)

[Du 2019] Wenna Du, Shuai Zhang, Zhiyong Wu, Qiuyu Shang, Yang Mi, Jie Chen, Chaochao Qin, Xiaohui Qiu, Qing Zhang and Xinfeng Liu. *Unveiling lasing mechanism in $CsPbBr_3$ microsphere cavities*. Nanoscale, vol. 11, no. 7, pages 3145–3153, 2019. (Cited on pages 59, 60 and 94.)

[Dyksik 2020] Mateusz Dyksik, Herman Duim, Xiangzhou Zhu, Zhuo Yang, Masaki Gen, Yoshimitsu Kohama, Sampson Adjokatse, Duncan K Maude, Maria Antonietta Loi, David A Egger*et al.* *Broad tunability of carrier effective masses in two-dimensional halide perovskites*. ACS Energy Letters, vol. 5, no. 11, pages 3609–3616, 2020. (Cited on pages 15, 70, 75 and 98.)

[Dyksik 2021a] Mateusz Dyksik, Herman Duim, Duncan K Maude, Michal Baranowski, Maria Antonietta Loi and Paulina Plochocka. *Brightening of dark excitons in 2D perovskites*. Science Advances, vol. 7, no. 46, page eabk0904, 2021. (Cited on pages 40, 52, 57, 59, 61, 71, 92 and 94.)

[Dyksik 2021b] Mateusz Dyksik, Shuli Wang, Watcharaphol Paritmongkol, Duncan K Maude, William A Tisdale, Michal Baranowski and Paulina Plochocka. *Tuning the Excitonic Properties of the 2D (PEA) 2 (MA) n- 1Pb n I3 n+ 1 Perovskite Family via Quantum Confinement*. The Journal of Physical Chemistry Letters, vol. 12, no. 6, pages 1638–1643, 2021. (Cited on pages 44 and 87.)

[Elliott 1957] RJ Elliott. *Intensity of optical absorption by excitons*. Physical Review, vol. 108, no. 6, page 1384, 1957. (Cited on pages 42 and 86.)

[Elumalai 2016] Naveen Kumar Elumalai, Md Arafat Mahmud, Dian Wang and Ashraf Uddin. *Perovskite solar cells: progress and advancements*. Energies, vol. 9, no. 11, page 861, 2016. (Cited on page 4.)

[Ema 2006] K Ema, K Umeda, M Toda, C Yajima, Y Arai, H Kunugita, D Wolverson and JJ Davies. *Huge exchange energy and fine structure of excitons in an organic-inorganic quantum well material*. Physical Review B, vol. 73, no. 24, page 241310, 2006. (Cited on pages 52 and 57.)

[Era 1994] M Era, S Morimoto, T Tsutsui and S Saito. *Organic-inorganic heterostructure electroluminescent device using a layered perovskite semiconductor (C6H5C2H4NH3) 2PbI4.* Applied physics letters, vol. 65, no. 6, pages 676–678, 1994. (Cited on pages 12 and 82.)

[Even 2013] Jacky Even, Laurent Pedesseau, Jean-Marc Jancu and Claudine Katan. *Importance of spin–orbit coupling in hybrid organic/inorganic perovskites for photovoltaic applications.* The Journal of Physical Chemistry Letters, vol. 4, no. 17, pages 2999–3005, 2013. (Cited on pages 9 and 10.)

[Even 2014a] Jacky Even, Laurent Pedesseau, Jean-Marc Jancu and Claudine Katan. *DFT and k· p modelling of the phase transitions of lead and tin halide perovskites for photovoltaic cells.* physica status solidi (RRL)–Rapid Research Letters, vol. 8, no. 1, pages 31–35, 2014. (Cited on page 6.)

[Even 2014b] Jacky Even, Laurent Pedesseau and Claudine Katan. *Analysis of multivalley and multibandgap absorption and enhancement of free carriers related to exciton screening in hybrid perovskites.* The Journal of Physical Chemistry C, vol. 118, no. 22, pages 11566–11572, 2014. (Cited on pages 6, 7 and 8.)

[Even 2015] Jacky Even, Laurent Pedesseau, Claudine Katan, Mikaël Kepenekian, Jean-Sébastien Lauret, Daniel Sapori and Emmanuelle Deleporte. *Solid-state physics perspective on hybrid perovskite semiconductors.* The Journal of Physical Chemistry C, vol. 119, no. 19, pages 10161–10177, 2015. (Cited on pages 6, 7 and 9.)

[Fert 2007] Albert Fert, Peter Grünberg, Gerhard Ertl, Mario R Capecchi, Martin J Evans and Oliver Smithies. *Nobel Prize 2007.* RESONANCE, 2007. (Cited on page 64.)

[Fonthal 2000] G Fonthal, L Tirado-Mejıa, JI Marın-Hurtado, H Ariza-Calderón and JG Mendoza-Alvarez. *Temperature dependence of the band gap energy of crystalline CdTe.* Journal of Physics and Chemistry of Solids, vol. 61, no. 4, pages 579–583, 2000. (Cited on page 64.)

[Fu 1999] Huaxiang Fu, Lin-Wang Wang and Alex Zunger. *Excitonic exchange splitting in bulk semiconductors.* Physical Review B, vol. 59, no. 8, page 5568, 1999. (Cited on pages 57 and 91.)

[Furdyna 1988] Jacek K Furdyna. *Diluted magnetic semiconductors.* Journal of Applied Physics, vol. 64, no. 4, pages R29–R64, 1988. (Cited on pages 75 and 98.)

[Gaj 1978] JA Gaj, J Ginter and RR Gałązka. *Exchange interaction of manganese 3d5 states with band electrons in Cd1- xMnxTe.* physica status solidi (b), vol. 89, no. 2, pages 655–662, 1978. (Cited on pages 64, 66 and 67.)

[Gaj 1979] JA Gaj, R Planel and G Fishman. *Relation of magneto-optical properties of free excitons to spin alignment of Mn2+ ions in Cd1- xMnxTe*. Solid State Communications, vol. 29, no. 5, pages 435–438, 1979. (Cited on page 64.)

[Gaj 1993] JA Gaj, R Planel and G Fishman. *Relation of magneto-optical properties of free excitons to spin alignment of Mn2+ ions in Cd1- xMnxTe*. Solid State Communications, vol. 88, no. 11-12, pages 927–930, 1993. (Cited on pages 64, 65 and 66.)

[Gaj 2010] Jan A Gaj and Jacek Kossut. *Basic Consequences of sp–d and d–d Interactions in DMS*. In Introduction to the Physics of Diluted Magnetic Semiconductors, pages 1–36. Springer, 2010. (Cited on pages 64, 66, 75 and 98.)

[Gaj 2011] Jan A Gaj and Jacek Kossut. Introduction to the physics of diluted magnetic semiconductors, volume 144. Springer Science & Business Media, 2011. (Cited on page 64.)

[Galkowski 2016] Krzysztof Galkowski, Anatolie Mitioglu, Atsuhiko Miyata, Paulina Plochocka, Oliver Portugall, Giles E Eperon, Jacob Tse-Wei Wang, Thomas Stergiopoulos, Samuel D Stranks, Henry J Snaith*et al. Determination of the exciton binding energy and effective masses for methylammonium and formamidinium lead tri-halide perovskite semiconductors*. Energy & Environmental Science, vol. 9, no. 3, pages 962–970, 2016. (Cited on pages 6 and 14.)

[Ghaithan 2021] Hamid M Ghaithan, Zeyad A Alahmed, Saif MH Qaid and Abdullah S Aldwayyan. *Density Functional Theory Analysis of Structural, Electronic, and Optical Properties of Mixed-Halide Orthorhombic Inorganic Perovskites*. ACS omega, vol. 6, no. 45, pages 30752–30761, 2021. (Cited on page 6.)

[Ghribi 2021] Amal Ghribi, Rim Ben Aich, Kaïs Boujdaria, Thierry Barisien, Laurent Legrand, Maria Chamarro and Christophe Testelin. *Dielectric Confinement and Exciton Fine Structure in Lead Halide Perovskite Nanoplatelets*. Nanomaterials, vol. 11, no. 11, page 3054, 2021. (Cited on pages 45, 57 and 91.)

[Goldschmidt 1926] Victor Moritz Goldschmidt. *Die gesetze der krystallochemie*. Naturwissenschaften, vol. 14, no. 21, pages 477–485, 1926. (Cited on page 2.)

[Goto 1990] Takenari Goto, Satoshi Taguchi, Kikuo Cho, Yasushi Nagamune, Shojiro Takeyama and Noboru Miura. *Magneto-optical effect of the Wannier exciton in a biaxial ZnP_2 crystal. III*. Journal of the Physical Society of Japan, vol. 59, no. 2, pages 773–778, 1990. (Cited on page 52.)

[Goto 2006] T Goto, H Makino, T Yao, CH Chia, T Makino, Y Segawa, George A Mousdis and George C Papavassiliou. *Localization of*

triplet excitons and biexcitons in the two-dimensional semiconductor $(CH_3C_6H_4CH_2NH_3)_2PbBr_4$. Physical Review B, vol. 73, no. 11, page 115206, 2006. (Cited on page 52.)

[Gramlich 2021] Moritz Gramlich, Carola Lampe, Jan Drewniok and Alexander S Urban. *How Exciton–Phonon Coupling Impacts Photoluminescence in Halide Perovskite Nanoplatelets*. Journal of Physical Chemistry Letters, vol. 12, no. 46, pages 11371–11377, 2021. (Cited on pages 22, 59, 60 and 94.)

[Gramlich 2022a] Moritz Gramlich, Michael W Swift, Carola Lampe, John L Lyons, Markus Döblinger, Alexander L Efros, Peter C Sercel and Alexander S Urban. *Dark and Bright Excitons in Halide Perovskite Nanoplatelets*. Advanced Science, vol. 9, no. 5, page 2103013, 2022. (Cited on page 22.)

[Gramlich 2022b] Moritz Gramlich, Michael W Swift, Carola Lampe, John L Lyons, Markus Döblinger, Alexander L Efros, Peter C Sercel and Alexander S Urban. *Dark and Bright Excitons in Halide Perovskite Nanoplatelets*. Advanced Science, vol. 9, no. 5, page 2103013, 2022. (Cited on pages 52, 57 and 90.)

[Hass 1988] KC Hass and H Ehrenreich. *Electronic and magnetic properties of II–VI diluted magnetic semiconductors*. Journal of Crystal Growth, vol. 86, no. 1-4, pages 8–14, 1988. (Cited on page 66.)

[He 1991] Xing-Fei He. *Excitons in anisotropic solids: The model of fractional-dimensional space*. Physical Review B, vol. 43, no. 3, page 2063, 1991. (Cited on page 15.)

[Hoke 2015] Eric T Hoke, Daniel J Slotcavage, Emma R Dohner, Andrea R Bowring, Hemamala I Karunadasa and Michael D McGehee. *Reversible photo-induced trap formation in mixed-halide hybrid perovskites for photovoltaics*. Chemical Science, vol. 6, no. 1, pages 613–617, 2015. (Cited on pages 4 and 5.)

[Hong 1992] X Hong, T Ishihara and AV Nurmikko. *Dielectric confinement effect on excitons in PbI 4-based layered semiconductors*. Physical Review B, vol. 45, no. 12, page 6961, 1992. (Cited on pages 70 and 71.)

[Huang 2005] Xiangyang Huang, Adi Makmal, James R Chelikowsky and Leeor Kronik. *Size-dependent spintronic properties of dilute magnetic semiconductor nanocrystals*. Physical review letters, vol. 94, no. 23, page 236801, 2005. (Cited on page 64.)

[Ishihara 1989] Teruya Ishihara, Jun Takahashi and Takenari Goto. *Exciton state in two-dimensional perovskite semiconductor (C10H21NH3) 2PbI4*. Solid state communications, vol. 69, no. 9, pages 933–936, 1989. (Cited on pages 12 and 82.)

[Ishihara 1990] Teruya Ishihara, Jun Takahashi and Takenari Goto. *Optical properties due to electronic transitions in two-dimensional semiconductors (C n H 2 n+ 1 NH 3) 2 PbI 4*. Physical review B, vol. 42, no. 17, page 11099, 1990. (Cited on page 71.)

[Jeong 2021] Jaeki Jeong, Minjin Kim, Jongdeuk Seo, Haizhou Lu, Paramvir Ahlawat, Aditya Mishra, Yingguo Yang, Michael A Hope, Felix T Eickemeyer, Maengsuk Kim*et al.* *Pseudo-halide anion engineering for α-FAPbI3 perovskite solar cells*. Nature, vol. 592, no. 7854, pages 381–385, 2021. (Cited on page 3.)

[Jia 2010] Aizhong Jia, Zhiqian Su, Lan-Lan Lou and Shuangxi Liu. *Synthesis and characterization of highly-active nickel and lanthanum co-doped SrTiO3*. Solid state sciences, vol. 12, no. 7, pages 1140–1145, 2010. (Cited on page 2.)

[Johnsson 2005] Mats Johnsson and Peter Lemmens. *Crystallography and chemistry of perovskites*. arXiv preprint cond-mat/0506606, 2005. (Cited on page 2.)

[Kataoka 1993] Takeshi Kataoka, Takashi Kondo, Ryoichi Ito, Satoshi Sasaki, Kazuhito Uchida and Noboru Miura. *Magneto-optical study on excitonic spectra in* $(C_6H_{13}NH_3)_2PbI_4$. Physical Review B, vol. 47, no. 4, page 2010, 1993. (Cited on pages 40 and 56.)

[Katz 2020] Eugene A Katz. *Perovskite: name puzzle and German-Russian odyssey of discovery*. Helvetica Chimica Acta, vol. 103, no. 6, page e2000061, 2020. (Cited on pages 1 and 81.)

[Keldysh 1979] LV Keldysh. *Coulomb interaction in thin semiconductor and semimetal films*. Soviet Journal of Experimental and Theoretical Physics Letters, vol. 29, page 658, 1979. (Cited on page 16.)

[Kim 2014] Jongseob Kim, Sung-Hoon Lee, Jung Hoon Lee and Ki-Ha Hong. *The role of intrinsic defects in methylammonium lead iodide perovskite*. The journal of physical chemistry letters, vol. 5, no. 8, pages 1312–1317, 2014. (Cited on page 10.)

[Kirstein 2022] E Kirstein, DR Yakovlev, MM Glazov, EA Zhukov, D Kudlacik, IV Kalitukha, VF Sapega, GS Dimitriev, MA Semina, MO Nestoklon*et al.* *The Landé factors of electrons and holes in lead halide perovskites: universal dependence on the band gap*. Nature Communications, vol. 13, no. 1, pages 1–8, 2022. (Cited on pages 8 and 61.)

[Kojima 2009] Akihiro Kojima, Kenjiro Teshima, Yasuo Shirai and Tsutomu Miyasaka. *Organometal halide perovskites as visible-light sensitizers for photovoltaic cells*. Journal of the american chemical society, vol. 131, no. 17, pages 6050–6051, 2009. (Cited on page 3.)

[Kulkarni 2006] Jaideep S Kulkarni, O Kazakova and Justin D Holmes. *Dilute magnetic semiconductor nanowires.* Applied Physics A, vol. 85, no. 3, pages 277–286, 2006. (Cited on page 64.)

[LakeShoreCryotronics-company 2022] LakeShoreCryotronics-company. *DT-670 Silicon Diodes.* https://www.lakeshore.com/products/categories/overview/temperature-products/cryogenic-temperature-sensors/dt-670-silicon-diodes, 2022. (Cited on pages 32 and 33.)

[Larson 1985] BE Larson, KC Hass, H Ehrenreich and AE Carlsson. *Exchange mechanisms in diluted magnetic semiconductors.* Solid state communications, vol. 56, no. 4, pages 347–350, 1985. (Cited on pages 75 and 98.)

[Larson 1988] BE Larson, KC Hass, H Ehrenreich and AE Carlsson. *Theory of exchange interactions and chemical trends in diluted magnetic semiconductors.* Physical Review B, vol. 37, no. 8, page 4137, 1988. (Cited on pages 66, 75 and 98.)

[Leguy 2016] Aurélien MA Leguy, Pooya Azarhoosh, M Isabel Alonso, Mariano Campoy-Quiles, Oliver J Weber, Jizhong Yao, Daniel Bryant, Mark T Weller, Jenny Nelson, Aron Walsh*et al. Experimental and theoretical optical properties of methylammonium lead halide perovskites.* Nanoscale, vol. 8, no. 12, pages 6317–6327, 2016. (Cited on page 5.)

[Li 2016] Zhen Li, Mengjin Yang, Ji-Sang Park, Su-Huai Wei, Joseph J Berry and Kai Zhu. *Stabilizing perovskite structures by tuning tolerance factor: formation of formamidinium and cesium lead iodide solid-state alloys.* Chemistry of Materials, vol. 28, no. 1, pages 284–292, 2016. (Cited on page 2.)

[Li 2017] Jing Li, Laihao Luo, Hongwen Huang, Chao Ma, Zhizhen Ye, Jie Zeng and Haiping He. *2D behaviors of excitons in cesium lead halide perovskite nanoplatelets.* The Journal of Physical Chemistry Letters, vol. 8, no. 6, pages 1161–1168, 2017. (Cited on pages 44 and 87.)

[Liang 2020] Hongyan Liang, Fanglong Yuan, Andrew Johnston, Congcong Gao, Hitarth Choubisa, Yuan Gao, Ya-Kun Wang, Laxmi Kishore Sagar, Bin Sun, Peicheng Li*et al. High color purity lead-free perovskite light-emitting diodes via Sn stabilization.* Advanced Science, vol. 7, no. 8, page 1903213, 2020. (Cited on pages 12 and 82.)

[Lin 2018] Yun Lin, Yang Bai, Yanjun Fang, Zhaolai Chen, Shuang Yang, Xiaopeng Zheng, Shi Tang, Ye Liu, Jingjing Zhao and Jinsong Huang. *Enhanced thermal stability in perovskite solar cells by assembling 2D/3D stacking structures.* The journal of physical chemistry letters, vol. 9, no. 3, pages 654–658, 2018. (Cited on pages 11 and 82.)

[Liu 2023] Ping Liu, Boyang Yu, Wanqing Cai, Xiongxian Yao, Kai Chang, Xinyan Zhao, Zhichun Si, Weiwei Deng, Yuanyuan Zhou, Guangmin Zhou*et al. Air-stable High-PLQY Cesium Lead Halide Perovskites for Laser-Patterned Displays.* Journal of Materials Chemistry C, 2023. (Cited on page 12.)

[Mathieu 1992] Henry Mathieu, Pierre Lefebvre and Philippe Christol. *Simple analytical method for calculating exciton binding energies in semiconductor quantum wells.* Physical Review B, vol. 46, no. 7, page 4092, 1992. (Cited on page 17.)

[Matsukura 1998] F Matsukura, H Ohno, A Shen and Y Sugawara. *Transport properties and origin of ferromagnetism in (Ga, Mn) As.* Physical Review B, vol. 57, no. 4, page R2037, 1998. (Cited on page 64.)

[Megaw 1952] Helen D Megaw. *Origin of ferroelectricity in barium titanate and other perovskite-type crystals.* Acta Crystallographica, vol. 5, no. 6, pages 739–749, 1952. (Cited on page 2.)

[Mitzi 1995] DB Mitzi, S Wang, CA Feild, CA Chess and AM Guloy. *Conducting layered organic-inorganic halides containing< 110>-oriented perovskite sheets.* Science, vol. 267, no. 5203, pages 1473–1476, 1995. (Cited on pages 12 and 82.)

[Miyata 2015] Atsuhiko Miyata, Anatolie Mitioglu, Paulina Plochocka, Oliver Portugall, Jacob Tse-Wei Wang, Samuel D Stranks, Henry J Snaith and Robin J Nicholas. *Direct measurement of the exciton binding energy and effective masses for charge carriers in organic–inorganic tri-halide perovskites.* Nature Physics, vol. 11, no. 7, pages 582–587, 2015. (Cited on pages 6 and 14.)

[Møller 1958] Chr Kn Møller. *Crystal structure and photoconductivity of caesium plumbohalides.* Nature, vol. 182, no. 4647, pages 1436–1436, 1958. (Cited on page 3.)

[Moniruddin 2018] Md Moniruddin, Baurzhan Ilyassov, Xiao Zhao, Eric Smith, Timur Serikov, Niyazbek Ibrayev, Ramazan Asmatulu and Nurxat Nuraje. *Recent progress on perovskite materials in photovoltaic and water splitting applications.* Materials Today Energy, vol. 7, pages 246–259, 2018. (Cited on pages 2 and 81.)

[Munekata 1989] H Munekata, H Ohno, S Von Molnar, Armin Segmüller, LL Chang and L Esaki. *Diluted magnetic III-V semiconductors.* Physical Review Letters, vol. 63, no. 17, page 1849, 1989. (Cited on page 64.)

[Neumann 2021] Timo Neumann, Sascha Feldmann, Philipp Moser, Alex Delhomme, Jonathan Zerhoch, Tim Van De Goor, Shuli Wang, Mateusz Dyksik, Thomas Winkler, Jonathan J Finley*et al. Manganese doping for enhanced magnetic brightening and circular polarization control of dark excitons in*

paramagnetic layered hybrid metal-halide perovskites. Nature Communications, vol. 12, no. 1, pages 1–8, 2021. (Cited on pages 69, 71 and 95.)

[Ohno 1998] Hideo Ohno. *Making nonmagnetic semiconductors ferromagnetic.* science, vol. 281, no. 5379, pages 951–956, 1998. (Cited on page 64.)

[Oku 2015] Takeo Oku. *Crystal structures of CH3NH3PbI3 and related perovskite compounds used for solar cells.* Solar Cells-New Approaches and Reviews, vol. 1, pages 77–92, 2015. (Cited on page 6.)

[Pelant 2012] Ivan Pelant and Jan Valenta. Luminescence spectroscopy of semiconductors. Oxford University Press, 2012. (Cited on pages 13, 14 and 15.)

[Pena 2001] MA Pena and JLG Fierro. *Chemical structures and performance of perovskite oxides.* Chemical reviews, vol. 101, no. 7, pages 1981–2018, 2001. (Cited on page 2.)

[Posmyk 2022] Katarzyna Posmyk, Natalia Zawadzka, Mateusz Dyksik, Alessandro Surrente, Duncan K Maude, Tomasz Kazimierczuk, Adam Babinnski, Maciej R Molas, Watcharaphol Paritmongkol, Mirosław Maczka*et al. Quantification of Exciton Fine Structure Splitting in a Two-Dimensional Perovskite Compound.* The Journal of Physical Chemistry Letters, vol. 13, pages 4463–4469, 2022. (Cited on page 71.)

[Qin 2020] Chuanjiang Qin, Atula SD Sandanayaka, Chenyang Zhao, Toshinori Matsushima, Dezhong Zhang, Takashi Fujihara and Chihaya Adachi. *Stable room-temperature continuous-wave lasing in quasi-2D perovskite films.* Nature, vol. 585, no. 7823, pages 53–57, 2020. (Cited on page 12.)

[Qiu 2021] Longbin Qiu, Sisi He, Yan Jiang and Yabing Qi. *Metal halide perovskite solar cells by modified chemical vapor deposition.* Journal of Materials Chemistry A, vol. 9, no. 40, pages 22759–22780, 2021. (Cited on page 10.)

[Raja 2017] Archana Raja, Andrey Chaves, Jaeeun Yu, Ghidewon Arefe, Heather M Hill, Albert F Rigosi, Timothy C Berkelbach, Philipp Nagler, Christian Schüller, Tobias Korn*et al. Coulomb engineering of the bandgap and excitons in two-dimensional materials.* Nature communications, vol. 8, no. 1, page 15251, 2017. (Cited on page 18.)

[Rossi 2020] Daniel Rossi, Xiaohan Liu, Yangjin Lee, Mohit Khurana, Joseph Puthenpurayil, Kwanpyo Kim, Alexey V Akimov, Jinwoo Cheon and Dong Hee Son. *Intense Dark Exciton Emission from Strongly Quantum-Confined CsPbBr3 Nanocrystals.* Nano Letters, vol. 20, no. 10, pages 7321–7326, 2020. (Cited on page 52.)

[Shapira 1991] Y Shapira. *Semimagnetic semiconductors and diluted magnetic semiconductors.* Physical Sciences, vol. 55, 1991. (Cited on page 64.)

[Shinada 1966] Masaki Shinada and Satoru Sugano. *Interband optical transitions in extremely anisotropic semiconductors. I. Bound and unbound exciton absorption.* Journal of the Physical Society of Japan, vol. 21, no. 10, pages 1936–1946, 1966. (Cited on pages 42 and 86.)

[Smith 2014] Ian C Smith, Eric T Hoke, Diego Solis-Ibarra, Michael D McGehee and Hemamala I Karunadasa. *A layered hybrid perovskite solar-cell absorber with enhanced moisture stability.* Angewandte Chemie International Edition, vol. 53, no. 42, pages 11232–11235, 2014. (Cited on pages 11 and 82.)

[Stranks 2014] Samuel D Stranks, Victor M Burlakov, Tomas Leijtens, James M Ball, Alain Goriely and Henry J Snaith. *Recombination kinetics in organic-inorganic perovskites: excitons, free charge, and subgap states.* Physical Review Applied, vol. 2, no. 3, page 034007, 2014. (Cited on page 3.)

[Straus 2016] Daniel B Straus, Sebastian Hurtado Parra, Natasha Iotov, Julian Gebhardt, Andrew M Rappe, Joseph E Subotnik, James M Kikkawa and Cherie R Kagan. *Direct observation of electron–phonon coupling and slow vibrational relaxation in organic–inorganic hybrid perovskites.* Journal of the American Chemical Society, vol. 138, no. 42, pages 13798–13801, 2016. (Cited on pages 59, 71 and 94.)

[Straus 2018] Daniel B Straus and Cherie R Kagan. *Electrons, excitons, and phonons in two-dimensional hybrid perovskites: connecting structural, optical, and electronic properties.* The journal of physical chemistry letters, vol. 9, no. 6, pages 1434–1447, 2018. (Cited on pages 16, 17 and 18.)

[Straus 2019] Daniel B Straus, Natasha Iotov, Michael R Gau, Qinghua Zhao, Patrick J Carroll and Cherie R Kagan. *Longer cations increase energetic disorder in excitonic 2D hybrid perovskites.* Journal of Physical Chemistry Letters, vol. 10, no. 6, pages 1198–1205, 2019. (Cited on pages 61 and 94.)

[Surrente 2021] Alessandro Surrente, Michał Baranowski and Paulina Plochocka. *Perspective on the physics of two-dimensional perovskites in high magnetic field.* Applied Physics Letters, vol. 118, no. 17, page 170501, 2021. (Cited on page 40.)

[Tai 2019] Qidong Tai, Xuyun Guo, Guanqi Tang, Peng You, Tsz-Wai Ng, Dong Shen, Jiupeng Cao, Chun-Ki Liu, Naixiang Wang, Ye Zhu*et al. Antioxidant grain passivation for air-stable tin-based perovskite solar cells.* Angewandte Chemie International Edition, vol. 58, no. 3, pages 806–810, 2019. (Cited on page 10.)

[Takagahara 1993] T Takagahara. *Effects of dielectric confinement and electron-hole exchange interaction on excitonic states in semiconductor quantum dots.* Physical Review B, vol. 47, no. 8, page 4569, 1993. (Cited on pages 57, 59, 91 and 94.)

[Tamarat 2019] Philippe Tamarat, Maryna I Bodnarchuk, Jean-Baptiste Trebbia, Rolf Erni, Maksym V Kovalenko, Jacky Even and Brahim Lounis. *The ground exciton state of formamidinium lead bromide perovskite nanocrystals is a singlet dark state.* Nature Materials, vol. 18, no. 7, pages 717–724, 2019. (Cited on pages 57 and 91.)

[Tan 2014] Zhi-Kuang Tan, Reza Saberi Moghaddam, May Ling Lai, Pablo Docampo, Ruben Higler, Felix Deschler, Michael Price, Aditya Sadhanala, Luis M Pazos, Dan Credgington, Fabian Hanusch, Thomas Bein, Henrgy J Snaith and Richard H Friend. *Bright light-emitting diodes based on organometal halide perovskite.* Nature Nanotechnology, vol. 9, no. 9, pages 687–692, 2014. (Cited on pages 12 and 83.)

[Tanaka 2003] Kenichiro Tanaka, Takayuki Takahashi, Takuma Ban, Takashi Kondo, Kazuhito Uchida and Noboru Miura. *Comparative study on the excitons in lead-halide-based perovskite-type crystals CH3NH3PbBr3 CH3NH3PbI3.* Solid state communications, vol. 127, no. 9-10, pages 619–623, 2003. (Cited on page 9.)

[Tanaka 2005] Kenichiro Tanaka, Takayuki Takahashi, Takashi Kondo, Kenichi Umeda, Kazuhiro Ema, Tsutomu Umebayashi, Keisuke Asai, Kazuhito Uchida and Noboru Miura. *Electronic and excitonic structures of inorganic–organic perovskite-type quantum-well crystal* $(C_4H_9NH_3)_2PbBr_4$. Japanese Journal of Applied Physics, vol. 44, no. 8R, page 5923, 2005. (Cited on pages 9, 10 and 52.)

[Tao 2017] Shu Xia Tao, Xi Cao and Peter A Bobbert. *Accurate and efficient band gap predictions of metal halide perovskites using the DFT-1/2 method: GW accuracy with DFT expense.* Scientific reports, vol. 7, no. 1, pages 1–9, 2017. (Cited on pages 5 and 6.)

[Tokura 1998] Y Tokura, Y Okimoto, S Yamaguchi, H Taniguchi, T Kimura and H Takagi. *Thermally induced insulator-metal transition in LaCoO 3: A view based on the Mott transition.* Physical Review B, vol. 58, no. 4, page R1699, 1998. (Cited on page 3.)

[Umebayashi 2003] T Umebayashi, K Asai, T Kondo and A Nakao. *Electronic structures of lead iodide based low-dimensional crystals.* Physical Review B, vol. 67, no. 15, page 155405, 2003. (Cited on page 8.)

[Urban 2020] Joanna M Urban, Gabriel Chehade, Mateusz Dyksik, Matan Menahem, Alessandro Surrente, Gaëlle Trippé-Allard, Duncan K Maude, Damien Garrot, Omer Yaffe, Emmanuelle Deleporte*et al.* *Revealing Excitonic Phonon Coupling in (PEA) 2 (MA) n- 1Pb n I3 n+ 1 2D Layered Perovskites.* The Journal of Physical Chemistry Letters, vol. 11, no. 15, pages 5830–5835, 2020. (Cited on page 70.)

[Varma 2018] PC Reshmi Varma. *Low-dimensional perovskites*. In Perovskite Photovoltaics, pages 197–229. Elsevier, 2018. (Cited on page 10.)

[Vescio 2022] Giovanni Vescio, Jesus Sanchez-Diaz, Juan Luis Frieiro, Rafael S Sánchez, Sergi Hernández, Albert Cirera, Iván Mora-Seró and Blas Garrido. *2D PEA2SnI4 Inkjet-Printed Halide Perovskite LEDs on Rigid and Flexible Substrates*. ACS Energy Letters, vol. 7, no. 10, pages 3653–3655, 2022. (Cited on pages 12 and 82.)

[Walters 2018] G Walters, M Wei, Oleksandr Voznyy, R Quintero-Bermudez, A Kiani, D-M Smilgies, Rahim Munir, Aram Amassian, S Hoogland and E Sargent. *The quantum-confined Stark effect in layered hybrid perovskites mediated by orientational polarizability of confined dipoles*. Nature communications, vol. 9, no. 1, pages 1–11, 2018. (Cited on pages 21 and 22.)

[Wang 2021] Yunuan Wang, Feilong Song, Yu Yuan, Jianchen Dang, Xin Xie, Sibai Sun, Sai Yan, Yanbing Hou, Zhidong Lou and Xiulai Xu. *Strong Triplet-Exciton–LO-Phonon Coupling in Two-Dimensional Layered Organic–Inorganic Hybrid Perovskite Single Crystal Microflakes*. Journal of Physical Chemistry Letters, vol. 12, no. 8, pages 2133–2141, 2021. (Cited on page 52.)

[Weber 1978] Dieter Weber. *CH3NH3PbX3, ein Pb (II)-system mit kubischer perowskitstruktur/CH3NH3PbX3, a Pb (II)-system with cubic perovskite structure*. Zeitschrift für Naturforschung B, vol. 33, no. 12, pages 1443–1445, 1978. (Cited on page 3.)

[Weidman 2017] Mark C Weidman, Aaron J Goodman and William A Tisdale. *Colloidal halide perovskite nanoplatelets: an exciting new class of semiconductor nanomaterials*. Chemistry of Materials, vol. 29, no. 12, pages 5019–5030, 2017. (Cited on pages 15 and 16.)

[Whitfield 2016] PS Whitfield, N Herron, WE Guise, K Page, YQ Cheng, I Milas and MK Crawford. *Structures, phase transitions and tricritical behavior of the hybrid perovskite methyl ammonium lead iodide*. Scientific reports, vol. 6, no. 1, pages 1–16, 2016. (Cited on pages 5 and 6.)

[Wu 1987] Maw-Kuen Wu, Jo R Ashburn, ClJ Torng, Pei-Herng Hor, Rl L Meng, Lo Gao, Z Jo Huang, YQ Wang and aCW Chu. *Superconductivity at 93 K in a new mixed-phase Y-Ba-Cu-O compound system at ambient pressure*. Physical review letters, vol. 58, no. 9, page 908, 1987. (Cited on page 3.)

[Yin 2014] Wan-Jian Yin, Tingting Shi and Yanfa Yan. *Unique properties of halide perovskites as possible origins of the superior solar cell performance*. Advanced Materials, vol. 26, no. 27, pages 4653–4658, 2014. (Cited on page 4.)

[Yuan 2019] Long Yuan. *Spatial and Temporal Imaging of Exciton Dynamics and transport in two-dimensional Semiconductors and heterostructures by ultrafast transient absorption microscopy.* PhD thesis, Purdue University, 06 2019. (Cited on page 13.)

[Yuan 2020] Fanglong Yuan, Xiaopeng Zheng, Andrew Johnston, Ya-Kun Wang, Chun Zhou, Yitong Dong, Bin Chen, Haijie Chen, James Z Fan, Geetu Sharma*et al. Color-pure red light-emitting diodes based on two-dimensional lead-free perovskites.* Science advances, vol. 6, no. 42, page eabb0253, 2020. (Cited on pages 12 and 82.)

[Zhang 2006] Qingsong Zhang, Tahir Cagin and William A Goddard III. *The ferroelectric and cubic phases in BaTiO3 ferroelectrics are also antiferroelectric.* Proceedings of the National Academy of Sciences, vol. 103, no. 40, pages 14695–14700, 2006. (Cited on page 2.)

[Zhang 2021] Li Zhang, Changjiu Sun, Tingwei He, Yuanzhi Jiang, Junli Wei, Yanmin Huang and Mingjian Yuan. *High-performance quasi-2D perovskite light-emitting diodes: from materials to devices.* Light: Science & Applications, vol. 10, no. 1, pages 1–26, 2021. (Cited on pages 11, 12, 82 and 83.)